STUDIES OF EARTH'S ATMOSPHERE FROM SPACE AND NEAR SPACE

A Thesis

Submitted for the Degree of

Doctor of Philosophy (Technology)

Submitted by

SREEJITH A. G.

Department of Applied Optics & Photonics

University College of Technology

University of Calcutta

March 2017

To my Family,

Friends and Teachers...

List of Publications

1. Refereed Journal Articles

(a) **A Raspberry Pi-Based Attitude Sensor** - ***A. G. Sreejith****, Joice Mathew, Mayuresh Sarpotdar, Rekhesh Mohan, Akshata Nayak, Margarita Safonova, Jayant Murthy*, Journal of Astronomical Instrumentation,vol. 03, issue. 02, 1440006, 2014.[1]

(b) **Pointing System for the Balloon-Borne Astronomical Payloads** - *K. Nirmal,* ***A. G. Sreejith****, Joice Mathew, Mayuresh Sarpotdar, , Ambily Suresh, Ajin Prakash, Margarita Safonova, Jayant Murthy* , Journal of Astronomical Telescopes, Instruments and Systems, Vol. 02, issue. 04, 047001, 2016.[2]

(c) **Development of Data Acquisition Methods for an FPGA-Based Photon Counting Detector** - *S. Ambily, , Mayuresh Sarpotdar, Joice Mathew,* ***A. G. Sreejith****, K. Nirmal, Ajin Prakash, Margarita Safonova, Jayant Murthy* , Journal of Astronomical Instrumentation,Vol 6, 1750002, 2017.[3]

(d) **High-altitude ballooning programme at the Indian Institute of Astrophysics** - *Akshata Nayak,* ***A. G. Sreejith****, Margarita Safonova and Jayant Murthy*, Current Science, Vol. 104, No. 6, March 2013.[4]

(e) **Predicting UV sky for future UV missions** - *Margarita Safonova , Rekhesh Mohan ,* ***A. G. Sreejith*** *and Jayant Murthy* , Astronomy and Computing, Vol 1, Pages 46-53, February 2013.[5]

[1]Presented in Chapter 4
[2]Presented in Chapter 4
[3]Used for the instrument in Chapter 6
[4]Presented in Chapter 3
[5]Presented in Chapter 2

(f) **Measurement of limb radiance and Trace Gases in UV over Tropical region by Balloon-Borne Instruments - Flight Validation and Initial Results** - ***A. G. Sreejith****, Joice Mathew, Mayuresh Sarpotdar, K. Nirmal, S Ambily, Ajin Prakash, Margarita Safonova and Jayant Murthy*, Atmos. Meas. Tech. Discuss., amt-2016-98, 2016.[6]

(g) **Overview of High-Altitude Balloon Experiments at the Indian Institute of Astrophysics**- *Margarita Safonova, Akshata Nayak,* **A. G. Sreejith***, Joice Mathew, Mayuresh Sarpotdar, S. Ambily, K. Nirmal, Sameer Talnikar, Shripathy Hadigal, Ajin Prakash & Jayant Murthy*, Astronomical and Astrophysical Transactions (AApTr), Vol. 29(3): 397-426 2016.[7]

2. **Refereed Conference Proceedings**

(a) **Near ultraviolet spectrograph for balloon platform** - ***A. G. Sreejith****, Margarita Safonova, Jayant Murthy*, Proc. SPIE, 9654, 2015.[8]

(b) **Balloon UV experiments for astronomical and atmospheric observations** - ***A. G. Sreejith****, Joice Mathew, Mayuresh Sarpotdar, Nirmal K., Ambily S., Ajin Prakash, Margarita Safonova and Jayant Murthy*, Proc. SPIE 9908, Ground-based and Airborne Instrumentation for Astronomy VI, 99084E August 9, 2016.[9]

(c) **Noise modeling and analysis of an IMU-based attitude sensor: improvement of performance by filtering and sensor fusion** - *K Nirmal,* ***A. G. Sreejith****, Joice Mathew, Mayuresh Sarpotdar, Ambily Suresh, Ajin Prakash, Margarita Safonova and Jayant Murthy*, Proc. SPIE 9912, Advances in Optical and Me-

[6]Presented in Chapter 3 & 5
[7]Presented in Chapter 3
[8]Presented in Chapter 6
[9]Presented in Chapter 8

chanical Technologies for Telescopes and Instrumentation, July 22, 2016.

(d) **Near UV imager with an MCP-based photon counting detector** - *S. Ambily, Joice Mathew, Mayuresh Sarpotdar,* ***A. G. Sreejith****, K. Nirmal, Ajin Prakash, Margarita Safonova and Jayant Murthy*, Proc. SPIE 9905, Space Telescopes and Instrumentation 2016: Ultraviolet to Gamma Ray, 990530 July 11, 2016.

(e) **An ultraviolet imager to study bright UV sources** - *Joice Mathew, Ajin Prakash, Mayuresh Sarpotdar,* ***A. G. Sreejith****, Margarita Safonova and Jayant Murthy*, Proc. SPIE 9905, Space Telescopes and Instrumentation 2016: Ultraviolet to Gamma Ray, 990533 July 13, 2016.

3. **Journal articles not part of this thesis**

(a) **Prospect for UV observations from the Moon**- *Margarita Safonova, Joice Mathew, Rekhesh Mohan,* ***A. G. Sreejith****, Jayant Murthy, Noah Brosch, Norbert Kappelmann, Arpit Sharma, Rahul Narayan*, Astrophysics and Space Science, Volume 353, Issue 2, pp 329-346, October 2014.

(b) **A software package for evaluating the performance of a star sensor operation** - *Mayuresh Sarpotdar, Joice Mathew,* ***A. G. Sreejith****, K. Nirmal, S. Ambily, Ajin Prakash, Margarita Safonova, Jayant Murthy*, Experimental Astronomy, Vol 43, Issue 1, pp 99–117, February 2017.

(c) **Prospect for UV observations from the Moon. II. Instrumental Design of an Ultraviolet Imager LUCI** - *Joice Mathew, Ajin Prakash, Mayuresh Sarpotdar,* ***A. G. Sreejith****, K. Nirmal, S. Ambily, Margarita Safonova, Jayant Murthy and Noah Brosch*, Astrophysics and Space Science, Vol 362, Issue 2, pp 11, February 2017.

Presentations

1. **Modelling UV sky for future UV missions**- ***A. G. Sreejith,*** *Margarita Safonova , Rekhesh Mohan and Jayant Murthy* , 31st ASI Meeting, ASI Conference Series, 2013, Vol. 9, pp 80, **Oral presentation**.

2. **High-altitude balloon experiments at IIA**-*Akshata Nayak,* ***A. G. Sreejith****, Margarita Safonova and Jayant Murthy*, 31st ASI Meeting, ASI Conference Series, 2013, Vol. 9, pp 136, **Poster presentation**.

3. **Balloon UV Observatory**- ***A. G. Sreejith,****Joice Mathew, Mayuresh Sarpotdar, Ambily Suresh, K. Nirmal, Akshata Nayak, Margarita Safonova and Jayant Murthy*, 32nd ASI Meeting, ASI Meeting, 2014, IISER, Mohali, **Poster presentation**.

4. **Near Ultraviolet spectrograph for CubeSats**- ***A. G. Sreejith****,Joice Mathew, Mayuresh Sarpotdar, S. Ambily, K. Nirmal, Ajin Prakash, Margarita Safonova and Jayant Murthy*, 229th AAS Meeting, AAS Meeting, 2017, Grapevine, TX, USA, **Poster presentation**.

Abstract

We are conducting high-altitude balloon experiments at Indian Institute of Astrophysics using small scientific payloads for atmospheric and astronomical studies. The ultraviolet (UV) window has been largely unexplored through balloons for astronomical observations. This thesis describes the basic instrumentation developed for the balloon experiments including the tracking, telemetry, and flight termination. The current observations are of atmospheric trace gases, as they provide valuable information about the state of the Earth's upper atmosphere. The trace gas retrieval is carried out using DOAS (Differential Optical Absorption Spectroscopy) technique from scattered solar light observations. We have developed a lightweight compact portable unit for measurement of trace gas strengths from ground and airborne platforms.

It is essential to understand the orientation of the payload and the direction of observation for any scientific study. To achieve this, we have developed a lightweight low-cost attitude sensor, based on a Raspberry Pi, built with readily available commercial components which can provide an accuracy of $\pm 0.24^{\circ}$. It can be used in experiments where weight and power are constrained, such as in light-weight high-altitude balloons. We are using the attitude sensor as the major building block in a closed-loop control system with driver motors, to stabilize and point cameras and telescopes for observations from a balloon-borne payload.

The thesis also describes the details of other instruments developed for balloon experiments, one of which is a near UV spectrograph. The spectrograph is a modified Czerny-Turner design in the wavelength band of 250 nm to 400 nm. The system uses an image intensified CMOS as the detector and is designed to be portable and scalable for different telescopes.

It is important to simulate the ultraviolet sky for future ultraviolet space missions and for this, we have developed a sky simulator tool. The software is available as a downloadable package and as a web-based tool. The thesis also contains a description of the time series analysis of airglow observations from FUSE (Far Ultraviolet Spectroscopic Explorer).

Contents

List of Figures

List of Tables

Chapter 1

Introduction

1.1 Introduction

Small and compact scientific payloads can be easily designed, constructed, and flown on high-altitude balloons. Despite the fact that large orbital observatories provide accurate observations and statistical studies of remote and/or faint sources, small telescopes on board balloons or rockets are still attractive because of their low cost and the ability to target specific areas (Sreejith et al., 2015). Although balloons have been used for a number of scientific observations, the near ultraviolet (NUV) window from 200 to 400 nm has been largely unexplored. This window includes several lines of importance to atmospheric chemistry (eg. SO_2, O_3, HCHO, BrO, etc.). Understanding these emissions not only helps in defining the UV foreground for astronomical observations but also enables us to study the atmospheric process to understand the greenhouse gases and climate change.

Atmospheric absorption and emission features, known as airglow lines, provide fundamental information about the earth's upper atmosphere (Meier, 1991). The absorption of solar energy in upper atmosphere results in excitation, dissociation, and ionization leading to fluorescence, which is usually

referred to as airglow. A preliminary analysis of FUV airglow from HUT (Hopkins Ultraviolet Telescope) (Feldman et al., 2001) and FUSE (Far Ultraviolet Spectroscopic Explorer) has been carried out by Feldman et al. (2001), who has pointed out the need for a more detailed follow-up. Understanding airglow is crucial in understanding the contamination from foreground emission to UV observations from Low Earth Orbits (LEO). The foreground comprises of airglow and zodiacal light, which depends on the look direction and the date and time of the observation (Murthy, 2009). Murthy (2014) carried out the exercise of classifying the ultraviolet foreground with empirical modeling using GALEX (Galaxy Evolution Explorer) data. They emphasized the need for proper spectroscopic observations to get a better understanding of the same.

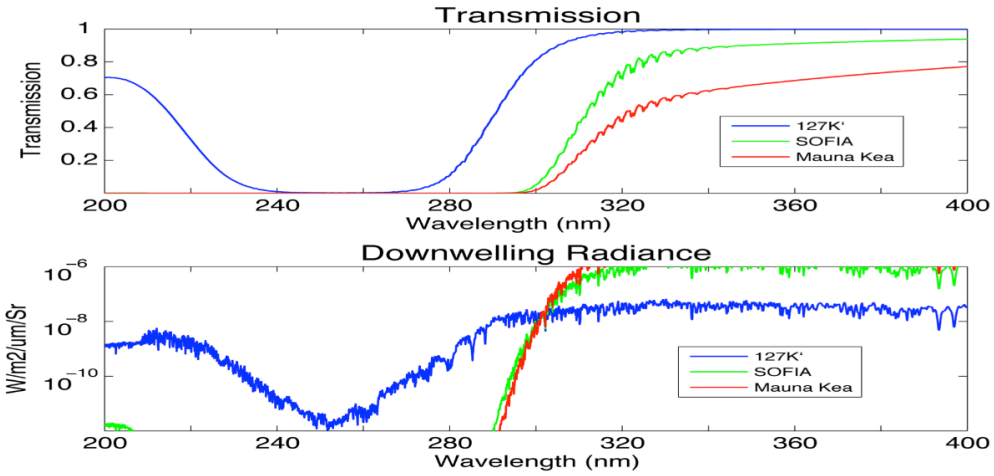

Figure 1.1: Near UV vertical transmission and daytime downwelling radiance from *Hibbits et al., 2013* (Image credit: *Hibbits et al., 2013*).

Ground-based observations have limitations of wavelength and atmospheric turbulence. Ultraviolet observations below 3000Å are not observable from the ground as ozone layer absorbs most of the UV radiations in earth atmosphere. Usually, these observations are carried out from satellites. High-altitude balloon experiments provide a low-cost alternative for observations of astronomical objects in near ultraviolet range. The Modtran transmission model in

atmosphere at different heights is as shown in Fig. 1.1 and is described in detail in Hibbits et al. (2013). At heights of above 34km, there is 100% transmission for radiations above 2700Å and more than 40% transmission for a band between 1900Å and 2200Å (Lemaire and Samain, 1989). With increase in heights above 40km, the absorption band of ozone drops drastically to about 10%, enabling observations above 1900Å (Navach et al., 1973).

At float heights in the stratosphere, the absence of 99% atmosphere enables diffraction limited imaging similar to that of space observatories but at a much lower cost. For example, with sufficient pointing stability and accuracy, a UV telescope (200–400 nm) located at these altitudes with an aperture of just 6-inches and a 1K×1K CCD array, could provide wide-field images with FWHM better than 1″ (Fesen et al., 2015). Additionally, space-based observatories have strict constraints because of detector safety reasons. These constraints on Sun/Moon angles limit the observations of solar system objects.

This thesis aims at developing instruments to carry out ultraviolet observations from the stratosphere. The thesis starts by describing an ultraviolet sky simulator for simulating the sky for future UV missions. The instruments and experiments for observations of near-ultraviolet from balloons and the observations obtained with the existing instruments are described in further chapters. Far ultraviolet observations of the airglow using FUSE data are also discussed. The details of the chapters in this thesis are described in brief in next section.

1.2 Thesis outline

Chapter Two: UV Sky Simulator

This chapter describes the UV sky simulator which can be used for predicting the sky for future UV missions. The details of the software structure and operation are discussed in this chapter. Online implementation of the tool

named ASTUS is discussed in detail. Two examples of the code for ultraviolet space telescopes are used to emphasize how the tool can be used for mission planing and science target selection.

Chapter Three: High-Altitude Balloon Experiments

The high-altitude balloon experiments being conducted from IIA are described here. The basic instrument setup including balloons, communication systems, telemetry, and recovery are discussed in detail. The payload for the balloon experiments and the calibration procedure for the instruments are described in this chapter. Scattered solar light observations carried out from balloon platform are also discussed.

Chapter Four: Attitude Sensor

We describe the development of an attitude sensor using off-the-shelf components, which acts as the main building block of a lightweight pointing system. The attitude sensor is based on MEMS based accelerometer, gyroscope and magnetometer and gives accuracy of $\pm 0.24^{\circ}$. The hardware implementation and calibration of the instrument is also discussed. A small discussion on the pointing system developed using this attitude sensor is also given in this chapter.

Chapter Five: Trace Gas Analysis with DOAS Technique

Using an off-the-shelf UV spectrograph whose calibration is described in chapter three, we have carried out observations of scattered solar light during the day. These spectroscopic observations have been analyzed using DOAS technique to obtain the trace gas column densities. In this chapter, we have explained the basic principles of DOAS analysis and the derived trace gas strengths of Ozone.

Chapter Six: Near UV Spectrograph with Photon Counting Detector

To improve the existing spectrograph, we have developed a near UV spectrograph which uses an image intensified CMOS as the detector. The detector can work in photon counting mode under low light levels. The basic design

of the spectrograph is a modified Czerny-Turner design in divergent illumination of the grating. All the optical components of the system are compact and off-the-shelf. The spectrograph is easily scalable and can be modified for different detectors and slit dimensions. The design and hardware implementation of the system are described in detail in this chapter.

Chapter Seven: Far UV Airglow Observations with FUSE

The analysis of time-tagged observations from the FUSE mission to describe the variation of airglow strength as a function of local time is dealt in this chapter. The dependence of airglow on look direction (i.e., Azimuth, elevation and limb angle) is also explained.

Chapter Eight: Summary and Future Work

The chapter concludes the thesis with a brief discussion on what has been achieved in the study and the future work that could be done to extend the present study.

Chapter 2

UV Sky Simulator

Safanova, M., Mohan, R., Sreejith, A. G, Murthy, J., Astronomy and Computing, 01, 46 (2013).

2.1 Introduction

One of the first ultraviolet observations of the sun was in 1946 from V2 rockets (Baum et al., 1946). The first observations of the UV sky were made later in 1957 (Byram et al., 1957). But we had to wait for over four decades for sensitive, nearly all-sky surveys in the UV, both imaging (Martin et al., 2005) and spectroscopic (Seon et al., 2011). From 2003 to 2012, the Galaxy Evolution Explorer (GALEX) (Martin et al., 2005) has observed almost 80% of the sky in two bands: FUV at 1344-1786 Å and NUV at 1771-2831 Å (Morrissey et al., 2007). The UV sky as we observe is a complicated combination of discrete UV sources such as hot stars and AGNs and the UV background (Murthy, 2009). It is important to know the UV background in large field-of-view (FOV) observations where the flux is integrated over a large solid angle. For observations of point sources, we need to properly understand and discern the background, so that it can be eliminated effectively. The accurate measurement of the UV background is important for many astrophysical and

even cosmological reasons as well — putting meaningful cosmological limits on the cosmic UV background has been the goal of many rockets, orbital and deep-space missions such as (Wamsteker et al., 2006).

We describe the development of a software to predict the UV sky, which can be used as a planning tool for an arbitrary space or ground-based observatory. For missions such as the Astrosat (Kumar et al., 2012), the count rate limitations and detector safety concerns limit the FoV so that there are no bright sources. With this tool, we can generate sky maps that can be used for planning of such missions.

2.2 Architecture and Operation of the Simulator

We have developed a software package, *Sky_model*, which is a set of modules in C. It simulates the appearance of the UV sky at different wavelengths in a given direction, using available archival data from GALEX, zodiacal light calculator and Hipparcos stellar data. We have written all codes in ANSI C, which can use any standard C compiler for build. We have considered a wavelength range from 1300 Å to 3200 Å for the tool and calculated the contributions to the UV sky from the stars, zodiacal light, and the diffuse galactic light separately. The wavelength limit is defined by the existing knowledge of the UV sky (Murthy 2009) and requirements of future missions. The following components of the UV sky can be optionally simulated:

- Diffuse UV background
- Zodiacal light
- Bright stars
- Airglow
- Instrument Background

The contribution from each of these components is estimated separately for a user-specified instrument response function. Once completed, all data are combined to generate an output image and the total count rate in a given field. The program is modular and self-documenting. The flow chart of the operational architecture is shown in Fig. 2.1.

2.2.1 Inputs to the Simulator

The simulator reads its default parameters from *diffuse_initparams.txt*, which is automatically generated. The user has an option to change these parameters at startup after which the file has to be unchanged during the execution of the code. For generating the output images, the simulator requires generic parameters such as time, date, and angular size of image and instrument parameters such as the dark count level and effective area curves of the filters. Various input parameters for each module is given as follows:

Diffuse UV Background

Starlight get scattered by the dust particles in the interstellar medium and this dominates the diffuse astrophysical background. The spatial variation in diffuse background can be from a few arcminutes to degrees and is difficult to model, as it depends on the distribution of stars and dust and their relative geometry (Murthy, 2009). We have applied the empirical sky distribution from Murthy et al. (2010), who used GALEX observations to tabulate the diffuse sky in two bands, FUV (1530 Å) and NUV (2321 Å). These values are subsequently integrated over the user-specified instrument response function to generate the UV background data for that instrument using the function CALC_SCALE_FACTOR. The module CALC_BKGD_FLUX calculates the diffuse sky background. The output array for the predicted galactic background is defined by the WCS parameters in the governing parameter file.

The input parameters for this module, specified in the governing param-

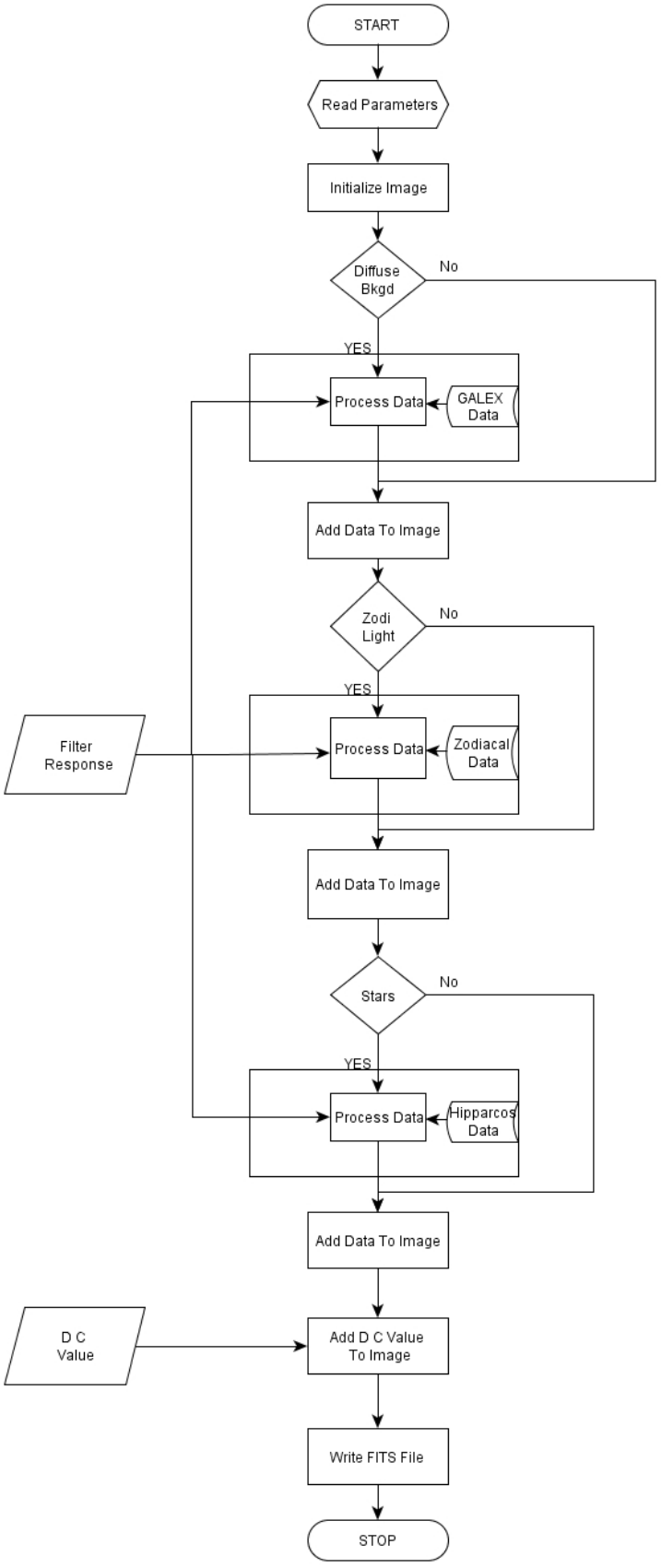

Figure 2.1: Operational structure of the *sky_model* code.

eter file `diffuse_initparams.txt`, are:

- The input data files from NUV and FUV all-sky data and diffuse background spectrum
- Angular cutoff limit: The default is 3 degrees. Since the input data consists of sky background towards different directions which are unevenly sampled there will be contributions from sky background for pixel.
- Cosecant scale factor: To accommodate for the lack coverage of galactic plane by GALEX or other missions, we use a cosine law simulation for calculating the background in those regions.

Zodiacal Light

Similar to diffuse background from the stars, sun light also gets scattered by interstellar dust. Since solar radiation is stronger at higher wavelengths ($>$ 200nm), the zodiacal light is a strong contributer in near UV missions and it is assumed that the zodiacal spectrum follows the solar spectrum. It is strongest near the Sun and the ecliptic plane and, therefore, is dependent on the time of year and the direction of observation. Leinert et al. (1998) have collated all the zodiacal light observations into a table as a function of helioecliptic coordinates which is used in this tool. The module CALC_ZOD_FLUX calculates the zodiacal light with inputs of the name of the zodiacal distribution file, the time (hour, day, month, year), and the WCS parameters. All these parameters are defined in the governing parameter file `diffuse_initparams.txt`. As per the helioecliptic coordinates of the line of sight using Leinert's table (Leinert et al., 1998), the zodiacal spectrum is generated for each pixel in the given FoV and it is then convolved with instrument response function to get the contribution of zodiacal light for a given direction using the function CALC_SCALE_FACTOR. The output is stored in a two-dimensional array.

Stars

Stars that emit UV light are mostly bright, early-type stars, particularly B stars which are distributed in an uneven manner in the sky. In the near UV region, we see some A stars and very little contribution from F stars and later (Murthy & Henry, 1995). Thus, we have included only bright stars for our calculations and assumed the contribution from extra galactic sources to be zero. We use catalog integration to model the stellar contribution to the sky in the UV (Henry, 1977). We used the Hipparcos catalog (Perryman et al., 1997) which includes magnitudes, distances, and spectral types of more than 250,000 stars to model the stars in the sky. The flux data corresponding to the spectral type from the Hipparcos catalog is obtained from the Castelli and Kurucz Atlas[1]. We use a function, CALC_FLUX as described in Sujatha et al., 2004 to correct for extinction and to obtain the V magnitude. Then the flux is convolved with the instrumental response function to yield the total number of counts for that star using CALC_SCALE_FACTOR. This process is repeated for all the stars within the FOV and their count rates are stored in a two-dimensional array.

Airglow

Airglow is the weak light emission from the Earth's upper atmosphere mostly due to the reaction of atmospheric molecules with solar photons, cosmic rays or atmospheric ions. Airglow spectrum contains multiple emission lines from atmospheric oxygen, nitrogen, and other constituents. It is an important contributor to the diffuse UV background for the missions on Low Earth Orbit and is difficult to model due to the strong dependence on the altitude, observation time, zenith angle, and solar cycle. It is a strong function of the local time as well; however most UV observations are performed only during the local night where the average level is about 200 photons/cm^2/s/sr/Å (Sujatha

[1]obtained from the STScI website:
`http://www.stsci.edu/hst/observatory/cdbs/castelli_kurucz_atlas.html`.

et al., 2009). Thus, we have kept this value as the current default, which can be changed by the user.

However, we are planning to incorporate the calculation of the airglow level in the tool. The input parameters required to simulate the airglow contribution are: (a) the airglow count rate (photons/cm^2/s/sr) and (b) the wavelength corresponding to that count rate. This value will be used to scale an airglow spectrum, before integrating it over the instrument response function to estimate the total airglow contribution.

Instrument Background

Intrinsic background of the detectors is usually determined by an approximately uniform distribution of counts caused by the β-decay of ^{40}K in the MCP glass and the surrounding detector structure and is typically low in the UV instruments, at a level of $\sim$ 5 counts/sec/cm^2. However, the externally induced detector background comes from the fast particles in the upper atmosphere hitting the MCP and varies throughout the orbit, rising in areas of high particle count, such as the South Atlantic Anomaly or polar regions; thus it is a strong function of the spacecraft orbit. We have set the default of the dark count at the intrinsic level, but it may be changed by the user. The FoV is also required to estimate the dark count rate per pixel. It is equal to 0.5 deg for UVIT which is set as the default, although any value can be entered here for a user-defined telescope. A set of real filter response curves for GALEX FUV and NUV channels and for UVIT/Astrosat mission are provided. The UVIT response functions are based on ground calibration values and will be updated as per the mission status. Users have an option to upload their own filter response curves as effective areas (in cm^2) as a function of wavelength (in Å).

2.2.2 Coordinates and Image

The software requires the galactic coordinates of the field as input and the output is also provided in the same coordinate system. The output will have the given input coordinates at the center of the frame. The reference pixels correspond to the center of the FITS image, and reference values are the input coordinates. Users can specify the size of the final image and the pixel scale in angular coordinates. We have set a limit of 2048 $\times$ 2048 pixels for output image to save the resources. For example, for the UVIT instrument, the FOV and image size will be set to 0.5 degrees and pixel size to 0.88 arcsec. This would produce a 2048 $\times$ 2048 pixel image, which is the expected dimension of an UVIT image.

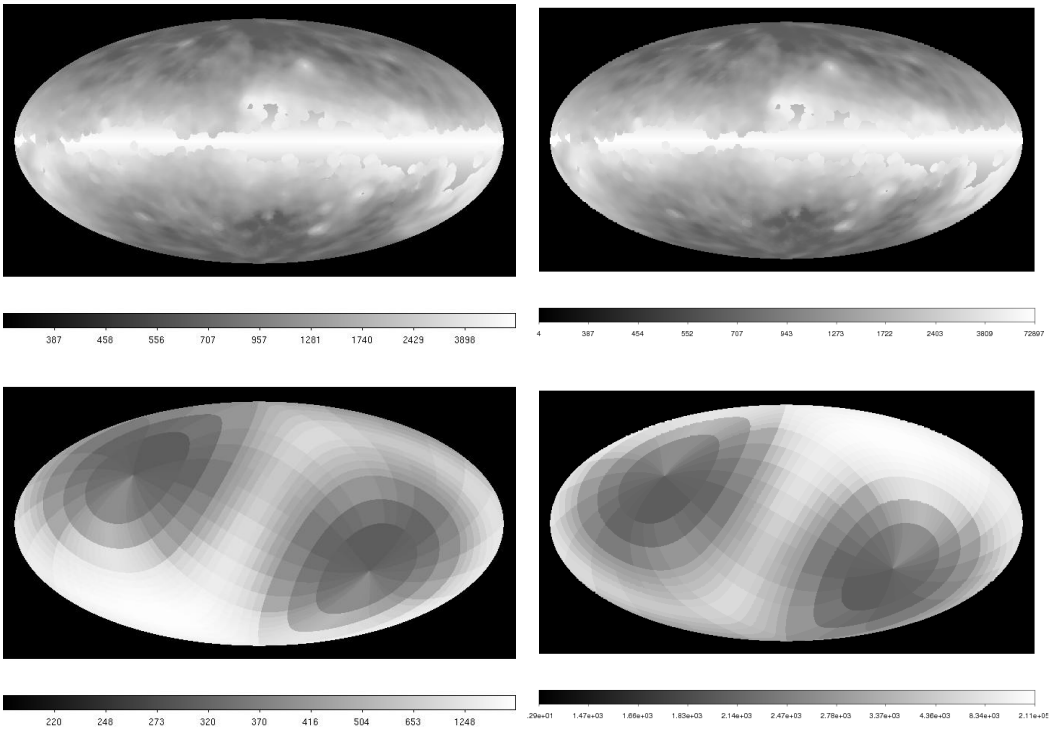

Figure 2.2: Examples of the output of the sky_model code. Top is the all-sky distribution of only diffuse NUV (*Left*) and FUV (*Right*) background. The areas for which there was no coverage by GALEX because of brightness limitations (Galactic plane) are filled with a cosecant law in the model. Bottom is the all-sky distribution of only zodiacal light in NUV in the months of April (*Left*) and September (*Right*).

To map the projection of output image, the tool provides a list of available projections. It is important to choose the correct projection to view or analyze the images. For example, for all-sky images an equal-area projection, such as Hammer-Aitoff, is more suitable for better understanding. For images that are smaller than 15 degrees, we suggest using a tangent plane projection.

2.2.3 Output Data

The final module in the simulation handles the output data file. This module waits till all the threads complete their run. Once all the image arrays corresponding to each sky component are available, they will be added together along with count rates from airglow and instrumental background to prepare the total image data and written out as a FITS image file. Because of the relatively low flux levels in the UV, most UV instruments are photon counting and we provide the flux in photon units (photons/sec/cm^2) if a single wavelength was chosen, or the count rate (counts/sec) if filter set was chosen at the input. Example of output of sky_model code code is as shown in Fig: 2.2.

2.3 Online implementation — ASTUS

Along with the C modules, we have developed a web interface with a perl/cgi back-end to run the sky simulator. The interface is easy-to-use; it accepts input values from user, validates them, runs the sky simulation software, and displays the output data for download. Validation of input values is performed both at the client side and server side before they are parsed to the simulation software. Client-side validation is to warn the user of incorrect input values, if any. The Perl backend script verifies user inputs and prepares the input parameter file which governs the operation of sky-simulation package. The output page also includes a quick-look image of the simulated field in JPEG format and count rates from various components. User input values are discussed in the sections below.

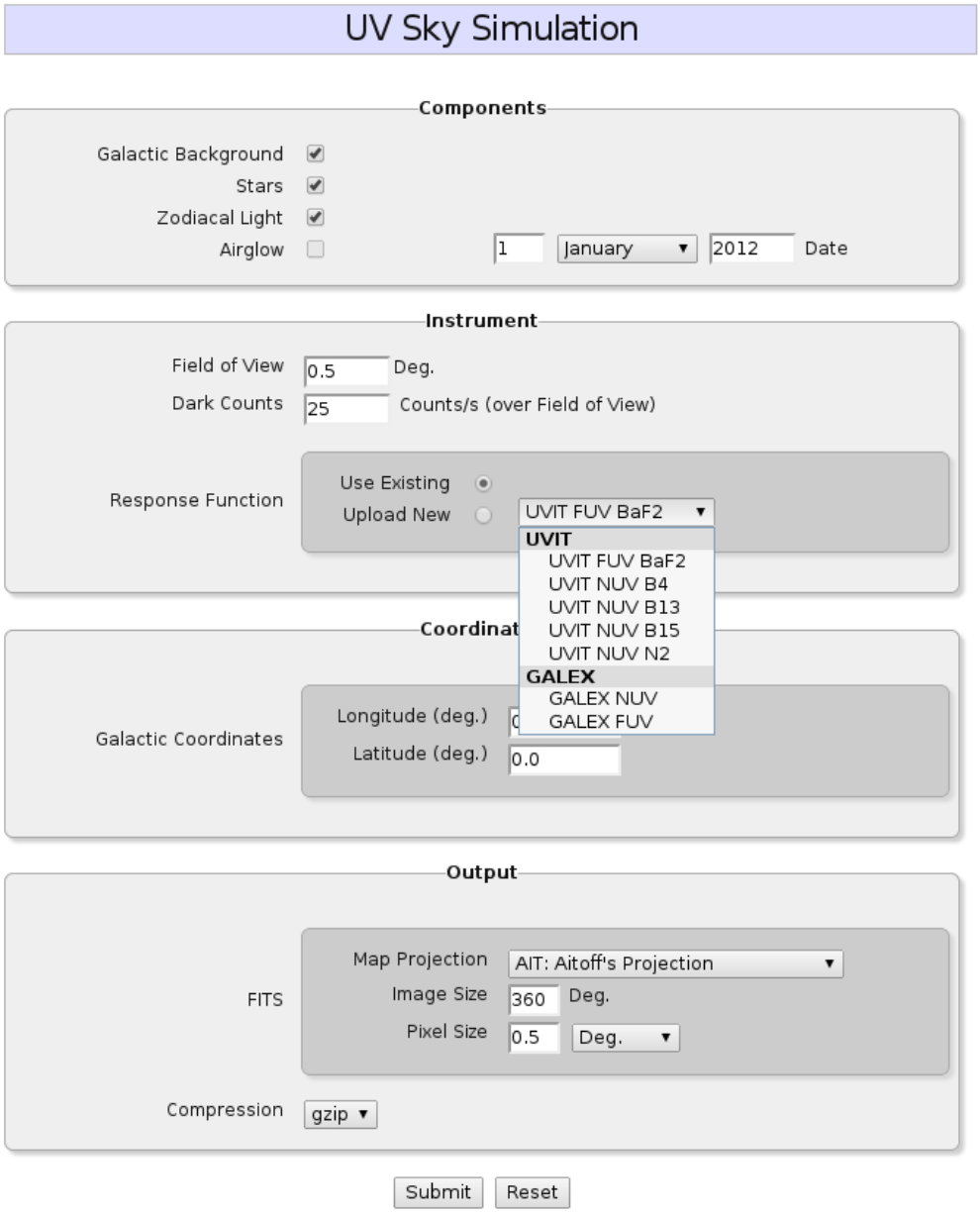

Figure 2.3: A screenshot of the ASTUS input page.

2.3.1 Input Interface

The input data fields on the webpage are shown in Fig. 2.3. Users may choose any combination of various sky components to be included in the simulated image. These include the diffuse UV background, zodiacal light and stars. The airglow contribution is also included in ASTUS.

2.3.2 Output

The output of the online tool is the image of the selected area of the sky and the contribution (in count rates) from various sky components of the image. A typical sky simulation for 1024×1024 pixel image that includes all sky components takes about two minutes to complete on our current server, thus we provide a JPEG image as a quick-look facility. The simulated and compressed image, along with the governing parameter file and link to the output page will be available for a period of 7 days after the job completion. Example images obtained in one of the UVIT filters are given in Fig. 2.4.

2.4 Applications

2.4.1 The UVIT instrument

UVIT, a payload on the Astrosat spacecraft, was launched in 2015 by the Indian Space Research Organization (ISRO) (Kumar et al., 2012). The simulator can be used in the preparation and planning of various UVIT key programs, which span a wide range of targets, from high-redshift galaxies to observations of stars, diffuse galactic structures and star-forming regions. UVIT can map small regions of sky (FOV=0.5°) with a higher spatial resolution ($1.''5-1.''8$) compared GALEX ($4.''5-6.''0$). The UVIT science goals are optimized for combined studies with the X-ray payloads, since ASTROSAT is a multi wavelength mission. Due to the sensitivity of the intensified C-MOS

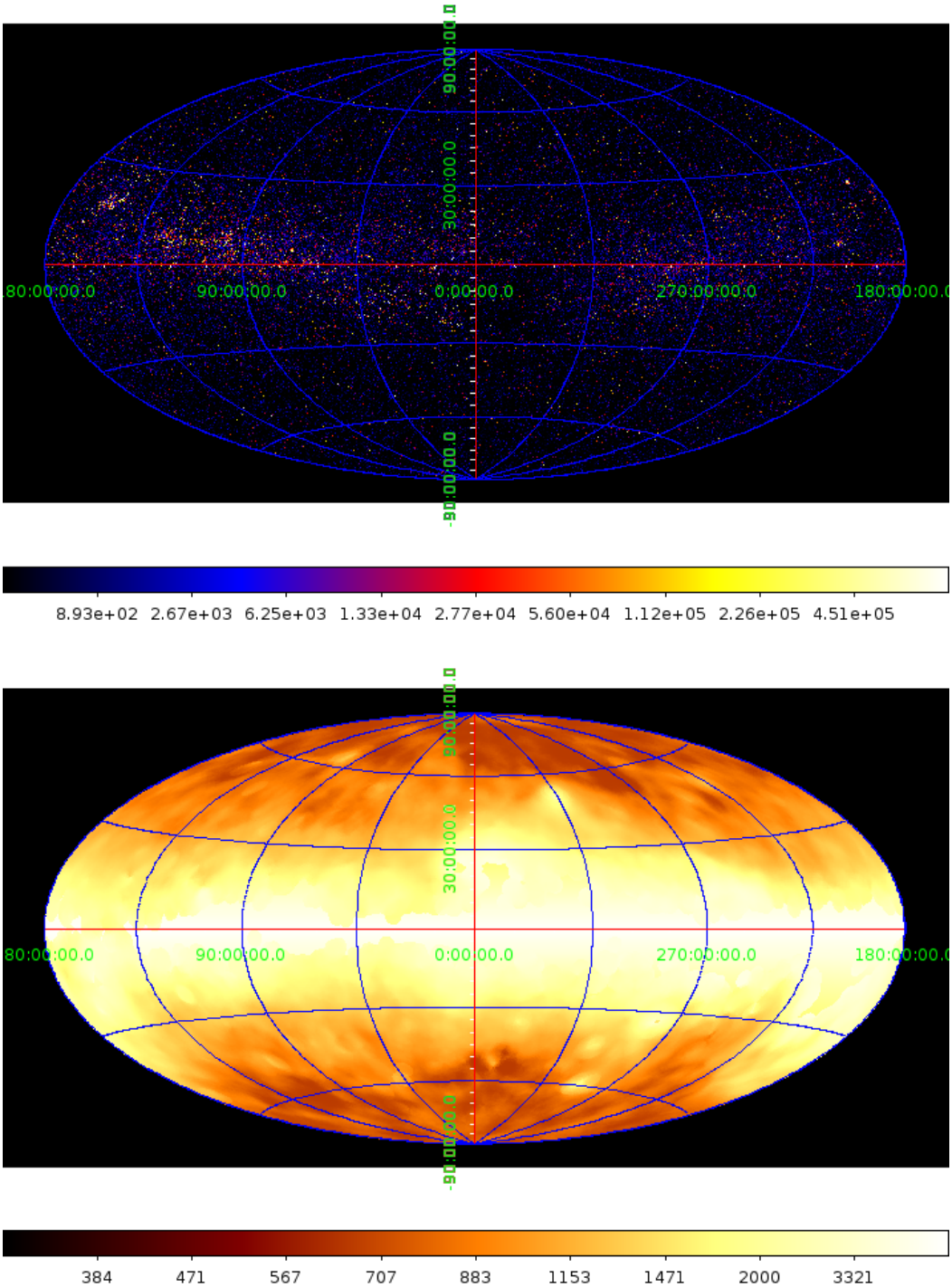

Figure 2.4: All sky images with UVIT NUV B13 filter as generated by ASTUS. *Top*: Hipparcos stars. *Bottom*: All-sky diffuse Galactic background.

detectors (Kumar et al., 2012), it is not possible to observe bright sources with UVIT. Thus it is important to predict the bright regions in the sky while planning the observations to warn about the directions where the telescope shall not be pointed. While selecting the photometric or astrometric calibration targets also, we should be careful enough to avoid stars that generate high count rates to create coincidence losses at the detector. We can use the simulator to get a map of calibration stars whose magnitudes will not exceed the count-rate limit. Also, the tool can be used to investigate the possibility of saturation of the detector while conducting sky surveys with a high dynamical range.

2.4.1.1 Basic parameters of the UVIT filters

The basic parameters of the selected UVIT filters are given in Table 2.1 and the effective areas of the filters are shown in Fig. 2.5. The calculations for the basic photometric parameters for UVIT filters were done based on the definition used in Safonova et al. (2009). The effective bandwidth is dependent on the spectral shape of radiation for broadband filters and can be calculated as the integral of the normalized effective areas. The mean, source-independent wavelength was calculated as

$$\lambda_{\rm c} = \frac{\int \lambda A_{\rm norm}(\lambda) d\lambda}{\int A_{\rm norm}(\lambda) d\lambda}\,, \tag{2.1}$$

where $A_{\rm norm}(\lambda)$ is the effective area normalized to 1. An exact relationship between $\langle F_\lambda \rangle$ and $\langle F_\nu \rangle$, the mean source intrinsic spectral-energy distribution in energy and frequency units, respectively, $\langle F_\lambda \rangle = \langle F_\nu \rangle c^2/\lambda_{\rm p}^2$, is provided by the pivot wavelength of the system,

$$\lambda_{\rm p} = \sqrt{\frac{\int A_{\rm norm}(\lambda) \lambda d\lambda}{\int A_{\rm norm}(\lambda) d\lambda/\lambda}}\,, \tag{2.2}$$

Table 2.1: Pre-launch characteristics of selected UVIT filters.

	BaF_2 (nm)	NUVB13 (nm)	NUVB15 (nm)	NUVB4 (nm)	NUVN2 (nm)
λ range	130–183	220–265	190–240	245–283	273–288
Bandpass $\Delta\lambda$	37.8	28.17	27.1	28.23	8.95
Central λ_c	155	243.6	218.3	242.8	279
Pivot λ_p	154.5	243.4	218.1	261.6	279
Effective λ_{eff}	123.2	243.3	217	263	279.2

Both the central and the pivot wavelengths are independent of the spectrum of the source. The effect of the source power distribution over a given filter is included in the filter's effective wavelength $\lambda_{\rm eff}$,

$$\lambda_{\rm eff} = \frac{\int \lambda A(\lambda) F(\lambda) d\lambda}{\int A(\lambda) F(\lambda) d\lambda}\,, \tag{2.3}$$

where $F(\lambda)$ is the source spectrum in ergs/cm^2/s/Å. This is the mean wavelength of the passband as weighted by the energy distribution of the source over the band and is especially useful in, for example, predicting the expected counts. In Table 2.1 we have given the effective wavelengths for Vega (except the FUV filter BaF_2 filter, for which the effective wavelength is for A1V star).

2.4.1.2 Calibration targets

An accurate ground calibration of the instrument, especially the spectral response calibration of the filters, is essential because the predicted flux values from the tool are dependent on the filter parameters. High values of the global and local count rates can adversely affect the long term performance of the detector. In addition there can be multiple events on the detector which affect the linearity of the response. The non-linearity may also arise due to high count rates. The upper limit on the total count rates, of the order of 10^5 counts/s, is determined mostly by the electronic readout mechanism of the microchannel plate (MCP). For UVIT, the count rate limit is kept

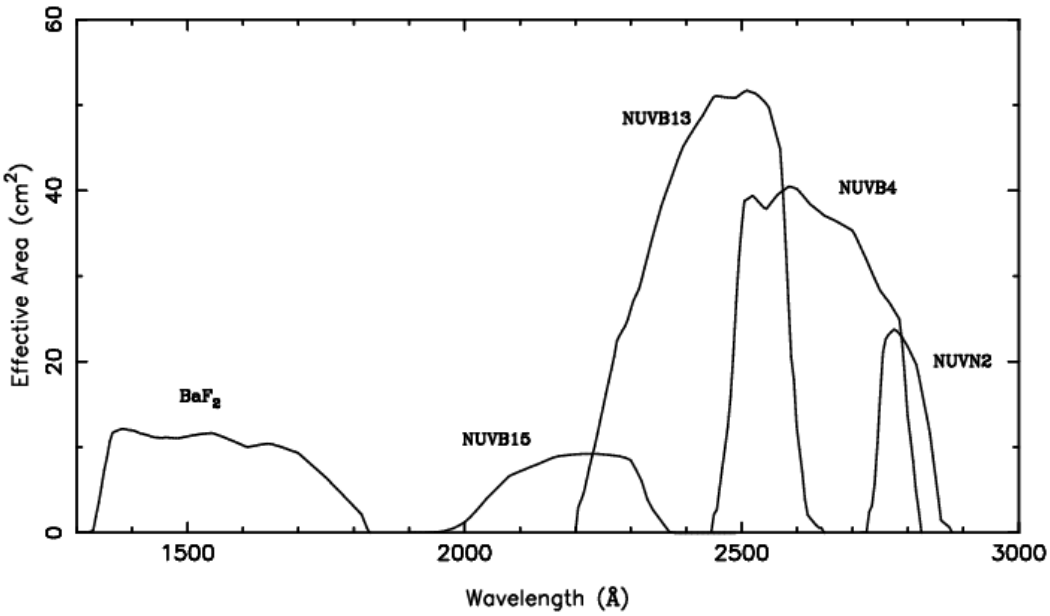

Figure 2.5: Pre-launch effective areas of five selected UVIT filters.

at $\sim 1.1 - 1.45 \times 10^5$ photons per second over the FoV (pre-launch values estimated from Kumar et al. (2012)).

We have selected an FUV filter BaF_2 and an NUV filter NUVB4 for these examples. Using the simulator, we have calculated the total (zodiacal + diffuse galactic + airglow) counts for two photometric standards (GD71 and G93-48) and for four open clusters that could be used for astrometric calibration (Feigelson 1, ASCC51, M67 and NGC188). These are suitable for UVIT flux calibration because being not very bright, the UV and optical spectra are available on the HST standard white dwarfs catalog. Astrometric calibration for UVIT includes pointing accuracy estimation, FOV calibration, distortion correction, etc. For these purposes, extended fields containing many stars with good astrometry such as open clusters, are generally used as in Safonova et al. (2009). Old open clusters M67 and NGC 188 were proposed by the UVIT team (Subramaniam & Tandon, 2012) and it was of interest to investigate their feasibility for the in-orbit calibration. The seasonal variation of zodiacal light levels in counts/s in the fields of photometric standards is

shown in Fig. 2.6. Zodiacal light is usually nearly negligible in FUV (from 0.3 to $\sim$ 30 counts/s over the whole FOV) in all considered fields. In NUV, however, it may significantly limit the viewing direction and/or observational time window. For example, in the field of the open cluster M67, the zodiacal light is prohibitively high all year round (see bottom panel in Fig. 2.6, where, for emphasis, the inset is showing the full range). The observations of photometric standards, GD71 and GD93-48, are also restricted during the months of May to September and February to April, respectively (Fig. 2.6, *top*). The diffuse background may also limit the fields; the levels produced by diffuse light and stars in counts/s over the full FOV are given in Table 2.2. It can be seen that GD71 has too high a background, especially in the NUV, and care should be taken while observing the open cluster ASCC51. However, stellar light may sometimes dominate over all backgrounds — the field of an open cluster Feigelson 1 is too bright due to stars and thus this cluster is not a good calibration source, while GD93-48 is good, except in the months of February to April (see Fig. 2.6, *top*). In Table 2.2 we provide the ecliptic latitudes of the considered fields; sources at low ecliptic latitudes will suffer high zodiacal background and thus should not be chosen for calibration. However in UVIT, in principle, smaller windows can be chosen to increase the readout time and thus reduce the total count level (Kumar et al., 2012).The conclusions on these calibrations targets are presented in Table 2.3.

2.4.2 The ULTRASAT mission

To study the variable sources in the sky, a wide-field transient explorer is proposed (Sagiv et al., 2014) by the Weizmann Institute, Caltech, and the Israeli Space Agency (ISA). The ULTRASAT (Ultraviolet Transient Astronomy Satellite) can cover a $\sim$ 210 deg^2 field with a 2kx2k CCD at the backend. The mission aims to observe the transient UV sky consisting of supernovae, stellar and AGN variability, tidal disruption events that peak in the UV, UV

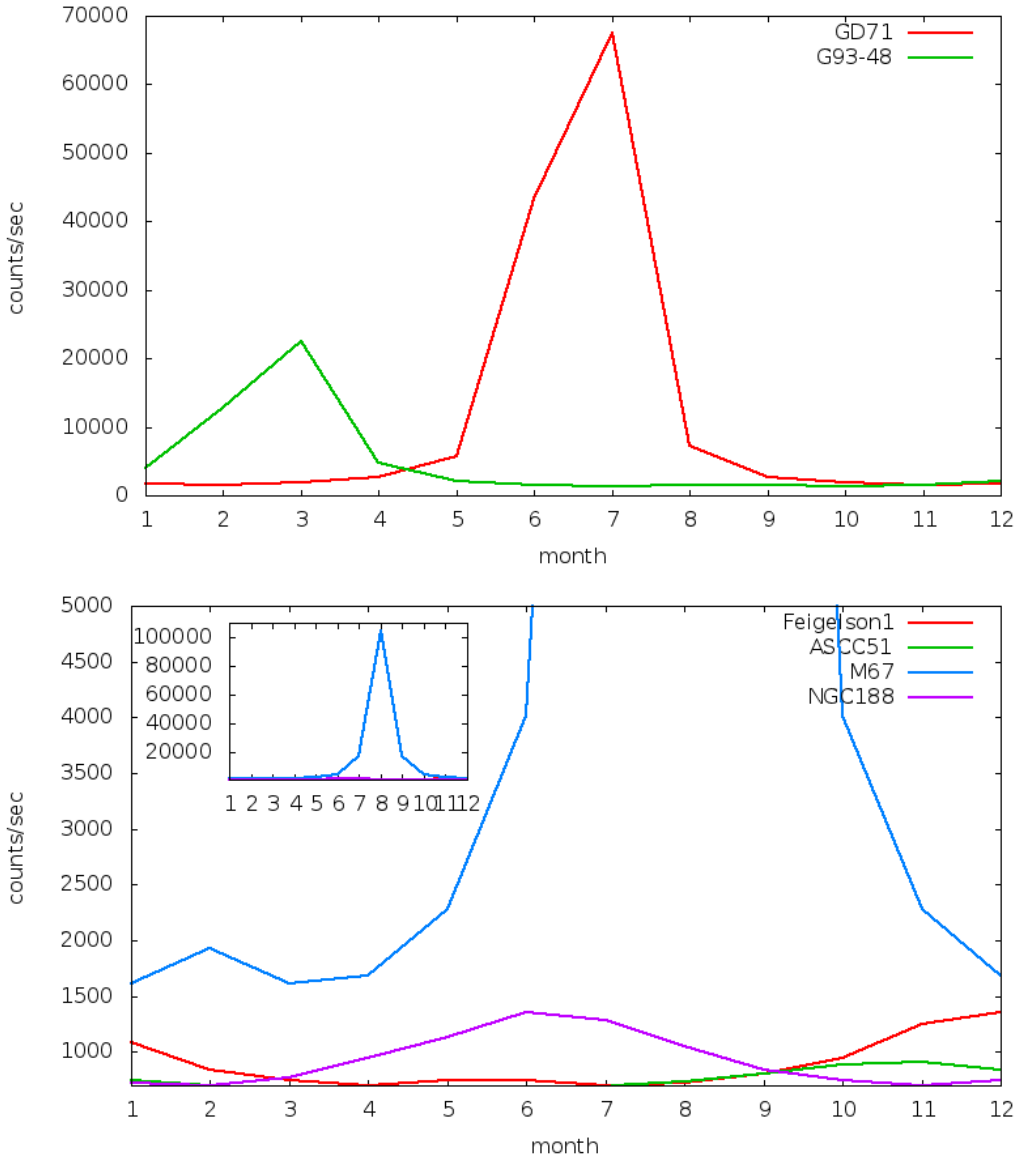

Figure 2.6: Seasonal variation of zodiacal light background level in NUV filter NUVB4 for two photometric standards GD71 (red line) and G93-48 (green line) (*top*) and four open clusters, ASCC 51 (green line), Feigelson (red line), NGC188 (magenta line) and M67 (blue line) (*Bottom*). The inset shows the full scale of zodiacal light levels in M67 field.

Table 2.2: Diffuse background (b/g) and stellar light counts in counts/s in possible photometric and astrometric calibration targets for UVIT.

Field		Ecl. lat	FUV (BaF_2)		NUV (NUVB4)	
Phot. Std	m_V		diff. b/g	stars	diff. b/g	stars
GD71†	13.03	-7.54	3520.2	557.85	8740.14	396.53
G93-48†	12.74	+14.37	317.09	209.04	562.43	224.45
Open cluster	$Dim_V^{\ddagger}$					
Feigelson1	18′	-63.92	1250.7	84248.3	2196.94	160175.0
ASCC 51	48′	-71.83	1546.36	356.16	3267.9	1520.12
M67	30′	-5.61	240.43	20.0	488.8	277.6
NGC188	14′	+65.15	310.13	437.02	757.04	2408.3

† Stellar contribution for these standards were calculated separately by IIA UVIT exposure time calculator (ETC) (privately available at `http://uvit.iiap.res.in/Software/Tools/etc`) — Hipparcos has no data for white dwarfs.
‡ Apparent dimension in V.

Table 2.3: Possible calibration sources for UVIT observations

Field	Conclusion	Reason
GD71	Not very good	High diffuse; May–Sep: high zodiacal b/g
G93-48	Good	All counts low; Feb–Apr: high zodiacal b/g
Feigelson 1	Bad	Very high counts from stars
ASCC51	Good in NUV	Rather high FUV diffuse b/g
M67	**Bad**	Very high zodiacal b/g all year
NGC188	Good	All counts low

afterglow from gamma ray bursts, etc. It was initially planned to launch the ULTRASAT into a low-earth Sun-synchronous dawn-dusk orbit where it will always look in the anti-Sun direction. The observation strategy is to stare at one direction of the sky continuously for a long duration. The *sky_model* simulator can be used to generate images of the sky for every day of the first year of the mission. This will help in identifying those regions which are safe to observe for a continuous stretch of time. Some of the simulator outputs are shown in Fig. 2.7. To aid the mission and science planning, we were involved in generating maps to get an estimation of the areas with low count level at any particular time of the year for the ULTRASAT mission team. *Sky_model* simulator will continue to be used in future to optimize and characterize pho-

tometric observing modes to determine the best observing strategy in the preparation and planning of observations.

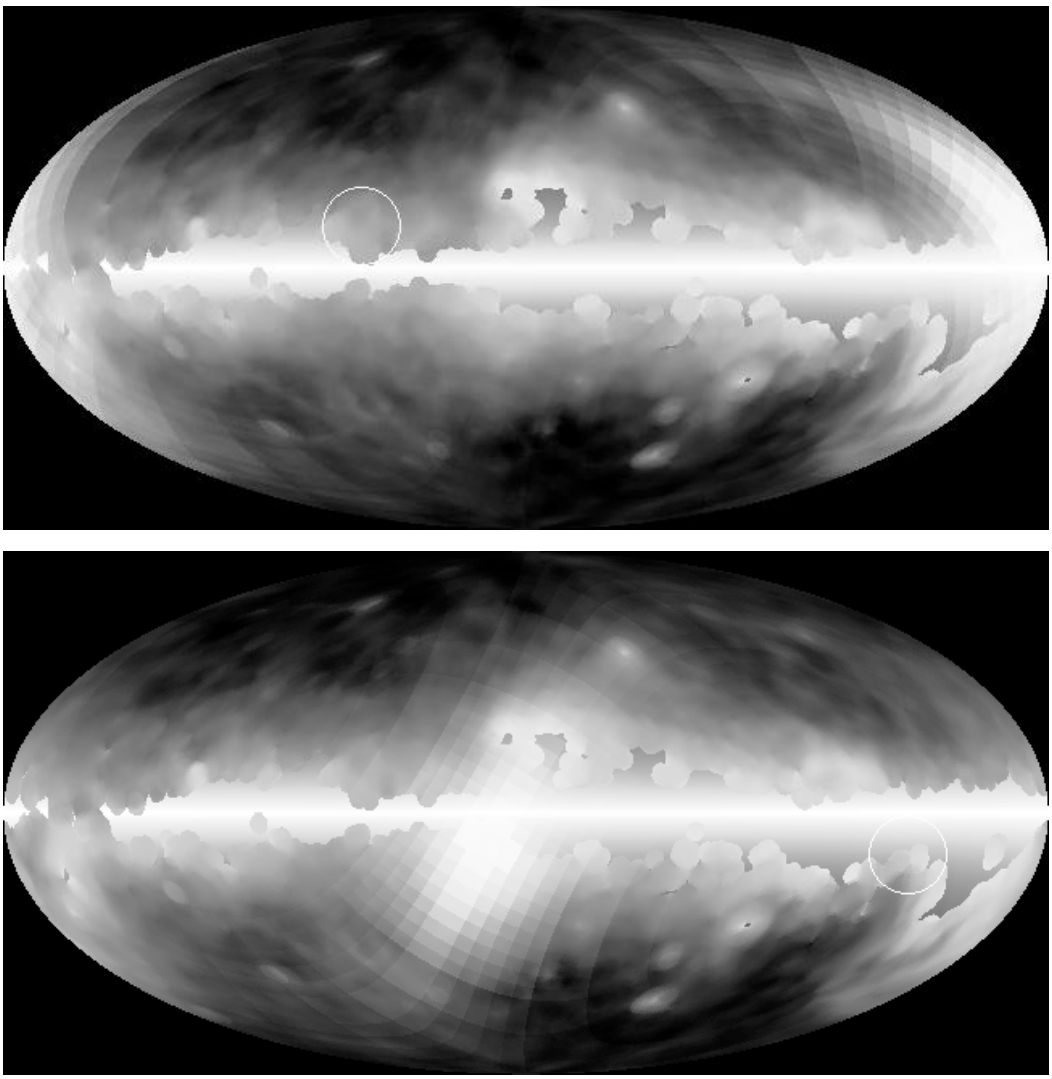

Figure 2.7: Simulated combined maps of the zodiacal light and diffuse background on 1st January (*Top*) and 1st July (*Bottom*). Satellite FOV, marked by a white circle, is in anti-Sun direction. Areas for which there was no coverage by GALEX (Galactic plane) are filled with a co-secant law in the model.

2.5 Future Developments

The web implementation of the simulator will be expanded to include various features. For example, to include the option for users to upload their own

stellar catalogs. These catalogs will have to have the following data on each star: galactic coordinates, spectral type, and standard V magnitude. Another option is to include hot white dwarfs as currently they are excluded from the simulation because Hipparcos catalog does not include them. In addition, the calculation of the airglow level from the two-line-elements of a spacecraft will be introduced as a separate module in the web interface. We also plan to implement flagging of the over-bright areas and include the option for a user to input user-defined FUV and NUV brightness limits. The effective areas of the UVIT filters will be regularly updated as and when the UVIT team updates them with observations in orbit. Work is being carried out on the implementation of the integration of the entire airglow spectrum (the airglow flux versus the wavelength) over the instrument response function to estimate the total airglow contribution. New diffuse background maps are now available using all the available GALEX observations. The new diffuse background data can be readily used with the offline version of the diffuse tool. The online tool still works on the diffuse data discussed in this chapter.

Chapter 3
High-Altitude Balloon Experiments

Sreejith, A. G., Mathew, J., et al., Atmos. Meas. Tech. Discuss amt-2016-98., doi:10.5194/amt-2016-98, 2016. & Safonova, M., Nayak, A., Sreejith, A. G., et al., Astronomical and Astrophysical Transactions (AApTr), Vol. 29(3), 397-426 (2016).

3.1 Introduction

High-altitude balloons for scientific experiments have been used for more than a century. One of the pioneers in using weather balloons was Leon Teisserenc de Bort, a meteorologist from France. His experiments of launching balloons as early as 1896 helped in the discoveries of the tropopause and stratosphere. Balloons have been used in many scientific experiments since then. In 1912, the Austrian physicist Dr. Victor Hess carried out an experiment by taking an Ion Chamber (IC) with him in a balloon upto heights of about 5 km and measured the radiation levels. He observed the ionization rate to increase with the increase in height. This led him to conclude that the radiation was of outer space in nature, he also eliminated the possibility of radiation from the sun

by carrying out the experiment during solar eclipse. For his discovery of cosmic radiation, Dr. Victor Hess was awarded the Physics Nobel Prize in 1936. High-altitude balloon experiments became a major part of scientific experiments after World War II. Latex balloons were used for atmospheric profiling and polyethylene balloons for bigger scientific experiments. Currently, most of the countries around the world have balloon programs, launching balloons carrying payloads from few hundred grams to tons. Balloon experiments are being used for atmospheric studies, astronomical observations from gamma rays to microwave, satellite prototyping, etc. Since the balloons reach low pressure and temperature regions in the atmosphere, most of the balloon experiments are unmanned automated systems.

Balloon experiments provide a great springboard for instrument development for future space missions. Cost of balloon-borne missions can be as low as 10 percent of a corresponding satellite mission, and they can be completed at a faster time scale. Instruments carried on high-altitude balloons have contributed immensely to our knowledge of the universe. For example, the discovery of cosmic microwave background anisotropy, the first detection of antiparticles in cosmic rays, the detection of chlorofluorocarbons and chlorine monoxide radicals in the stratosphere, discovery of positron emissions, and observation of black-hole X-ray transients from the galaxy to name a few, and many more significant results can be expected in the future from balloon-borne instruments. Several Earth Observing Satellites trace their instrument heritage to balloon experiments as well. A lot of the instruments used on satellites for atmospheric and astrophysical observations were developed initially for high-altitude balloon flights, and they continue to be a valuable test-bed for future space flight instrumentation.

A typical high-altitude balloon experiment consists of a flight train as shown in Fig. 3.1. A balloon filled with suitable gas carries the entire system. The different parts of the balloon experiment are described in detail below.

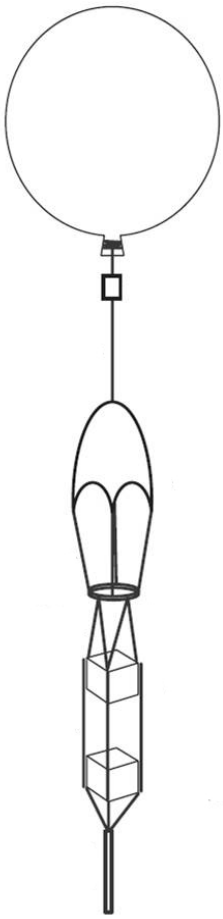

Figure 3.1: Typical balloon flight train. The main components from the top are: *i.* Balloon, *ii.* Flight termination unit, *iii.* Parachute, *iv.* Scientific payloads, *v.* Communication system.

3.1.1 Balloon

The type of the balloon used depends on the type of experiment. Balloons are filled with low-density gases like Hydrogen or Helium to provide the required lift. This enables them to rise above the lower atmosphere to the required heights. As the balloon reaches higher altitudes, the pressure in the atmosphere decreases exponentially. The reduced pressure causes the balloon to expand. The balloon expands till the material used for its manufacture reaches the elastic limit which leads us to the different classification of balloon as follows:

3.1.1.1 Sounding balloon

Sounding or Weather balloons are typically manufactured from latex. These balloons are designed to expand till they burst. A sounding balloon that has a diameter in the range of 2 meters at launch can expand to a diameter of up to 10 m at burst. These balloons are specified by their weight in grams. A 350 g sounding balloon weighs 350 g, a 1200 g weighs 1200 g, etc. All the sounding balloons usually have the same thickness of latex. The difference in weight between different size balloons comes from the size of the mold the balloon was manufactured on. A bigger mold will require a larger amount of latex resulting in a heavier balloon. This also enables the balloon to stretch to a larger diameter before bursting. Even though meteorological satellites provides us with most of the data for weather research and forecast activities, sounding balloons are still launched from across the globe for precise vertical analysis of atmospheric parameters at least twice a day from different meteorological stations.

These balloons are now also used for carrying out small stratospheric research as they can reach heights above 25 km.

3.1.1.2 Equal pressure balloons

The equal pressure or zero pressure balloon is usually made of low-density polyethylene (LDPE) with a thickness of the orders of $10 - 20\mu$. These balloons work by maintaining the internal pressure lesser than outside environmental pressure. It is partly inflated before launch, rises until the gas inside expands to fill the balloon's fixed volume. As the balloon reaches float altitude, the excess gas is vented out to satisfy the equilibrium condition. These balloons use load tapes to carry suspended load and can stay afloat for a few days. These balloons may also require dropping of ballast to maintain the height.

3.1.1.3 Super pressure balloons

A super pressure balloon prevents the gas from venting out and is usually made with a non-extensible material like Linear low-density polyethylene (LLDPE). The inside pressure is greater than outside in these balloons. Upon reaching the float altitude, the balloon is pressurized by excess helium. These balloons can provide extremely long duration float and are considered a key technology for future astronomical observations from near space.

3.1.2 Parachutes

A parachute is used as a safety device on every balloon flight in order to reduce the damage to the payload by reducing the descent rate while coming down. A parachute is usually made of a cloth material that is woven together or a canopy made of plastic (like ripstop nylon) and connected to the payload with suspension lines (called shroud lines). The parachute canopy is made axially symmetric about the vertical axis and can have holes in it. The major features of descending parachute with payload are as shown in Fig. 3.2.

Parachutes we use in high-altitude ballooning are usually made out of ripstop nylon and have a descent rate of less than 5m/s. Parachutes are generally described by their nominal diameter (i.e., the diameter of the drag-producing surface area of the canopy). The parachute should be able to withstand the stress during flight termination. Fully deployed parachutes are used in scientific ballooning instead of packed parachutes.

3.1.3 Flight Termination Unit

Balloons can drift off if the winds are high during the flight. Each balloon flight may have restriction on its flight path and time due to permissions from local aviation authorities. To restrict the motion of the balloon, it is necessary to have a flight termination unit (FTU). Two independent FTUs are designed and used for our balloon system. A timer-based system placed

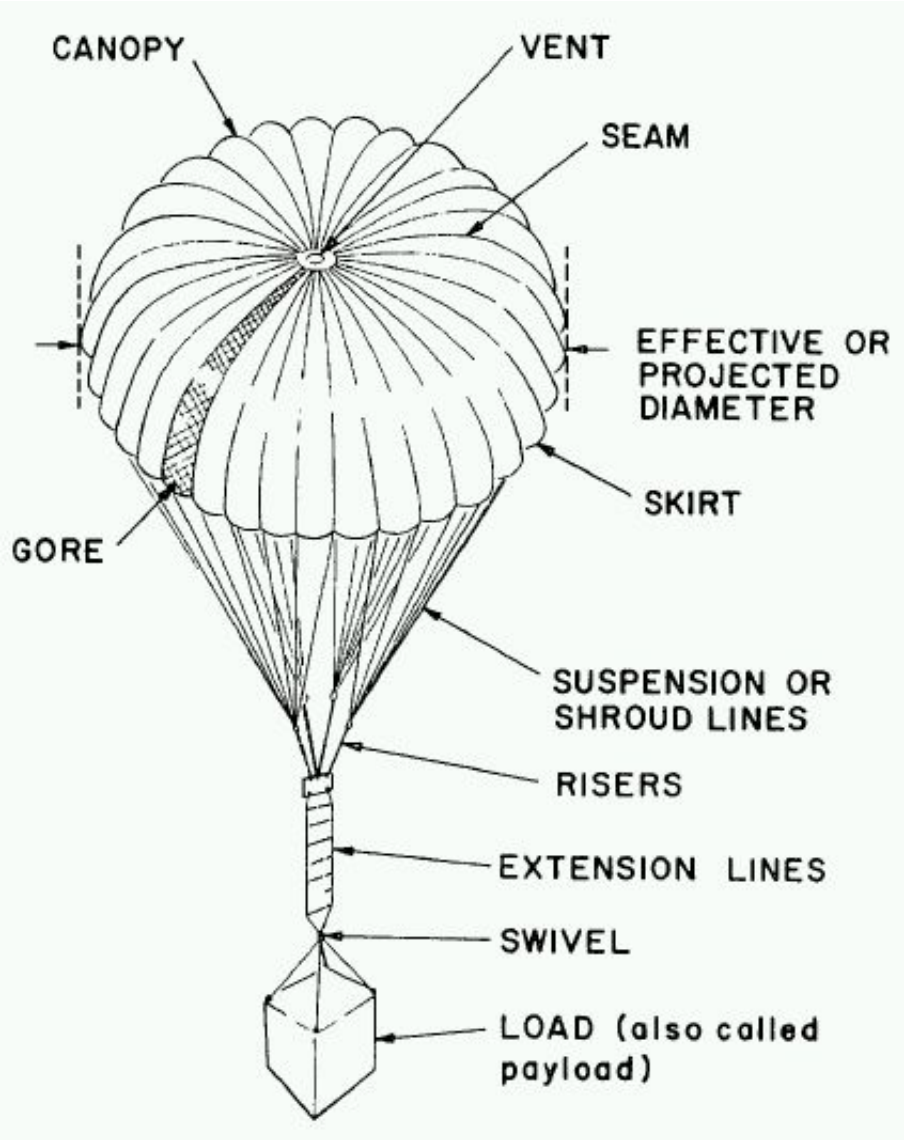

Figure 3.2: Major features of parachute used in high-altitude ballooning (image credit: http://stratocat.com.ar/stratopedia/119.htm).

below the parachute and a GPS-based system inside the main payload box. The FTU uses a thermal knife, in the form of a heated nichrome coil, to cut the load line between the balloon and the parachute. The two types of FTU's employed are described as follows:

3.1.3.1 Timer-based FTU

This mechanism consists of a tiny Microcontroller-based timer circuit which is programmed for a predefined duration depending on the type of experiment. This system is initialized just before the balloon launch. The timer system activates the relay to heat up the nichrome wire wound across the load line to melt it, severing it for the deployment of the parachute after the programmed time.

A lithium polymer battery (7.6 V, 2100 mAh) is used to provide power to the circuit. The circuit and the battery are placed inside an insulated box which is attached to the load line under the parachute. The programmable timer is based on an Atmega328P microcontroller unit (MCU) which triggers the Flight Termination at a set termination time.

3.1.3.2 Geo-fencing based FTU

A high-altitude balloon has a tendency to drift away with lateral winds in case it fails to burst or reaches buoyancy before reaching burst altitude. It can drift up to 300 kms away from the predicted burst location during these flights. In such cases, to avoid it from reaching undesirable locations (like water bodies, mountains, neighboring states/countries), a failsafe mechanism is used to keep track of the current balloon location in terms of latitude and longitude and to terminate the balloon flight if it goes outside of a pre-programmed 'geographical fence'. Our flight termination system also consists of a geo-fence, which works at high-altitudes, and a flight termination mechanism (FTM).

The circuit for the geo-fencing FTU is implemented as an add-on 'shield' for an Arduino. The geo-fencing feature is implemented using a Global Positioning System (GPS) module and the Arduino Uno board. The FTM consists of a relay which connects the nichrome wire to the battery through a relay. The Arduino Uno triggers the relay when the current location reported

by the GPS is found to be out of the boundary defined by the programmed latitudes and longitudes. The relay passes the current through the nichrome wire, the nichrome wire heats up and cuts the loadline between the balloon and the payload. In such cases, the thermal knife is activated to separate the loadline between the balloon and the payload.

GPS module: A GPS module from Ublox (NEO-6) is used in this circuit. This module has the advantage that it works at high-altitudes, unlike the readily available GPS chips. This GPS module receives signals from different GPS satellites visible in the sky. Then it estimates its location with respect to the satellites and computes the latitude and longitude of the location. This process is called GPS locking. Once locked, the GPS module updates its location every second and reports this location to a serial port in a specific format. This format is called NMEA (National Marines Electronics Association) sentence format. After decoding these NMEA format sentences, the latitude, longitude, time, and altitude information of the location of the payload is obtained.

Microcontroller: The Arduino microcontroller decodes the NMEA sentences from the GPS module. The latitude and longitude of the launch location at Hosakote are 13004', 77057'. The GPS fence is usually defined at 150 kms from the launch location which corresponds to around 1015' shift in latitude and longitude. Therefore, the boundary is programmed as the square of geographical locations on the map described by 13004' $\pm$ 1015', 77057' $\pm$ 1015'. The current location of the balloon, obtained from decoded NMEA sentences, is then compared with the programmed boundary of latitude and longitude. If the balloon is outside the boundary, the micro controller triggers the flight termination.

3.1.4 Communication and Tracking

Balloon experiments can be carried out without tracking the balloon also, but as one of the major advantages of balloon experiment is re-usability of the payload, it is necessary to recover and reuse the payload and hence communication and tracking becomes a major part of balloon experiment. Communication is required for direct transfer of data from payload, this enables the data from the experiments to be available even if the payload is lost. Another method is to store the data on-board and collect it when the payload is recovered. In these cases, we have to use tracking of the balloon to recover the payload. The balloon payload is tracked with the help of an on-board GPS sensor.

3.1.4.1 Telemetry unit

The telemetry unit we use in our experiments is an off the shelf Automatic Packet Reporting System (APRS) tracker pre-configured with a call sign. It is a complete, self-contained, water resistant unit using 10-watt of power. The system has a TinyTrak3 controller chip, together with a Byonics GPS2OEM GPS receiver, and a Standard Male Antenna (SMA). It is an omnidirectional antenna which broadcasts 10W of RF power on HAM frequency band. 144.8 MHz RF frequency is used to transmit the GPS coordinates in APRS packet format. Audio Frequency Shift Keying (AFSK1200) is used to encode zeros and ones from the digital APRS packet structure on the radio input. The baud rate used by the transmitter to transmit the packet is 1200 Hz. Various parameters like packet repetition time, frequency deviation, RF carrier frequency can be set for the transmitter. TinyTrak3Config is used to configure these parameters in the transmitter. It can operate for 8 days with one set of batteries when transmitting the position every 2 minutes, although we have configured the packet repetition interval to be 10 seconds.

3.1.4.2 Receiving stations

A two-fold receiver system is used to track the balloon in real-time and to keep a log of the packets received from the balloon. A combination of a base station and a moving station is used to ensure successful tracking and recovery of the payload. An omnidirectional monopole antenna with a mobile radio station from Kenwood (TM-271A [1]) is used as a base station. The antenna is placed at the highest location possible on launch site campus to increase the range. During the experiment, the base station works as a data logger which records the position (time, latitude, longitude and height) of the balloon at regular intervals. This information is useful to correlate with various science instrument in the payload. It also provides the height and ascent rate of the balloon at any given time. The base station radio is tuned to 144.8MHz and is always used as a listener. The audio output of the radio is connected to the soundcard in the computer. AFSK1200 Decoder software is used to decode the packets which are received from the radio and displayed on the screen. The decoder software requires an open-squelch radio for synchronization of the message signal. Hence, the base station radio is used in SQL(Squelch) 0 mode.

The moving station is an hand-held walkie talkie (TH-K2AT[2]) with a sensitive portable antenna and a hand-held decoder which is a TinyTrak4 decoder from Byonics. The speaker output of the handheld walkie talkie is connected to the TinyTrak4 which decodes the AFSK1200 signal transmitted by the balloon transmitter and displays on an LCD. This system also operates in SQL 0 mode.

[1] https://www.kenwood.com/i/products/info/amateur/tm271_usa/
[2] http://www.kenwood.com/i/products/info/amateur/th_k2at/

3.1.5 Flight Prediction

Flight prediction is carried out taking into consideration the buoyant force, gravity, crosswinds, and air drag. To simulate the balloon path, the variation of attitude of payload is calculated using the US standard atmosphere values. A MATLAB program was written for the same. The lateral movement of the payload due to wind is simulated using wind velocity information. This information is available from the National Operational Model Archive and Distribution System (NOMADS) program at the National Oceanic and Atmospheric Administration (NOAA). The Wind velocity, temperature and pressure data for different geopotential altitude and temperatures throughout the entire world are available in GRIB format with two levels of resolution, 0.5° or1°.

The code simulates the motion of the payload, by evaluating the force acting on the payload over small increments of time. It is assumed that the acceleration of the payload is constant over the small time interval. The motion with respect to the wind is calculated for the altitude obtained from the vertical profile calculations described earlier. The prediction code and details of how to use it are available at https://github.com/iiabaloongroup.

Before the launch, we calculate the balloon flight path using the Cambridge University Spaceflight Landing Predictor (http://predict.habhub.org/) together with our own codes described here. The balloon information to be used in the simulations are provided by the manufacturer.

3.2 Payload

The balloon-borne instrumental set-up used for our experiments consists of three main parts: (i) a spectrograph with an optical fiber and a light collecting lens; (ii) a Raspberry Pi single board computer (SBC) which acts as the onboard computer; (iii) an optical monitoring camera and environment

sensors; and (iv) an attitude sensor described in detail in the next chapter. All instruments were powered through a 13000 mAh lithium battery with two power settings at 5 W and 10 W. Fig. 3.3 shows the schematics of the instrumental set-up. The entire payload was placed in a STYROFOAM ™[3] box to keep the electronics above their operating temperatures of 0°C. We found that, in practice, we had to make a small opening on the payload box to allow the heat from the electronics to escape.

To validate this method, we have flown this setup on two high-altitude balloon flights which are described in Section 3.3.

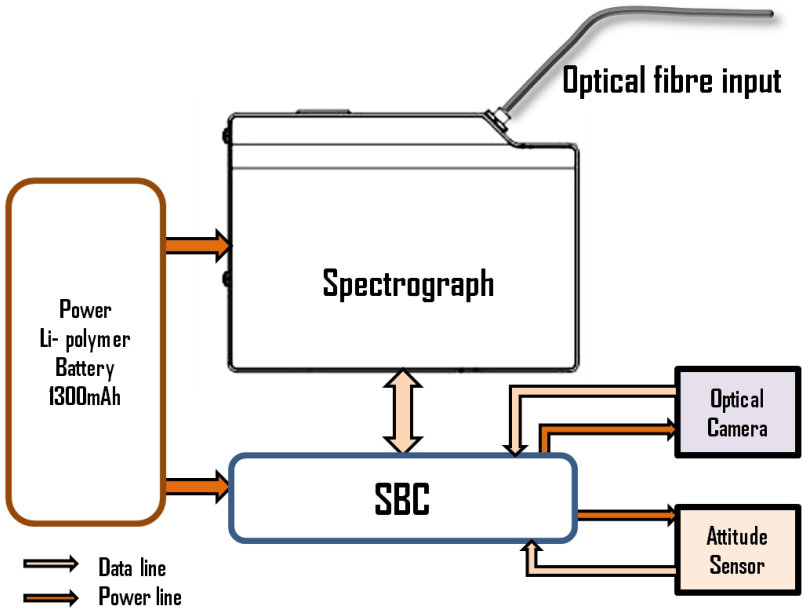

Figure 3.3: Schematics of the instrumental set-up.

3.2.1 UV Spectrograph

The spectrograph used is a CCD-based, miniature holographic grating spectrograph[4], operating in a symmetrical crossed Czerny-Turner configuration with high sensitivity in the near UV range (200 – 400 nm), see Fig. 3.4. Light is collected through a 5 mm lens with a field of view (FOV) of 2°. The

[3]Dow Chemical Company, USA
[4]MayaPro2000 from Ocean Optics, Inc, USA

collected light is fed to the spectrograph through an optical fiber (400 μm diameter) placed at the focus of the lens. The aperture of the fiber also acts as the entrance slit for the spectrograph. The light from the entrance slit is focused onto the fixed holographic UV grating (1200 lines/mm) by the collimating mirror. The peak efficiency of the grating is above 30% in the wavelength band of 200–420 nm with a full-width half-maximum (FWHM) of 0.75 nm. The diffracted light is reflected by the grating which is focused by the mirror onto an FFT (Full Frame Transfer) back-thinned CCD from Hamamatsu (S10420-1106-01) with a quantum efficiency of over 40% in the 200 – 400 nm wavelength band. The spectrum is spread over the CCD array which consists of 2048 × 64 pixel elements. The spectrograph is controlled by an on-board microcontroller which handles the Analog to Digital Conversion and the communication with the payload computer. The detailed specifications of the spectrograph are provided in Table 3.1.

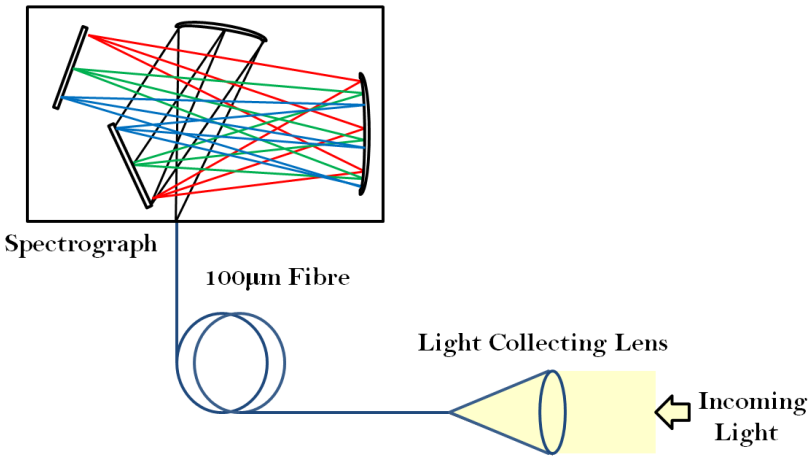

Figure 3.4: Schematic of the spectrograph.

The spectrograph is controlled using the on-board flight computer (Raspberry Pi SBC) through its USB port. McDAS (Maya control and data acquisition software) is a python code developed to control and carry out the data acquisition from the spectrograph and store it as a text file on board the flight computer. Prerequisites for this python code are the *numpy* and

Table 3.1: MayaPro2000 technical specifications

Dimensions	$149 \times 109.3 \times 50.4$ mm
Weight	0.96 kg (without power supply)
Power	500 mA at +5V DC
Design	Symmetric crossed Czerny-Turner
Focal length (input)	F/4 101.6 mm
Input Fiber Connector	SMA 905 to single-strand optical fiber (0.22 NA)
Gratings	Holographic UV, 1200 lines/mm
Entrance Slit	$400\,\mu$m
Detector	Hamamatsu S10420
Architecture	2-D Back-thinned
Thermoelectric cooling	No
Pixels	Total: 2068×70, Active: 2048×64
Pixel size	$196\,\mu\text{m}^2$
Well Capacity	200,000 $\bar{e}$
Peak QE	75%
QE @250 nm	65%
Integration time	7.2 ms – 5 sec
A/D converter	16 bit, 250 kHz
Dynamic range	10000:1+ (typical: $\sim 15000:1+$)
Signal-to-noise ratio	450:1
Non-linearity (uncorrected)	$\sim 10.0\%$
Linearity (corrected)	$> 99.7\%$
Temperature	Storage: -30°C to +70°C; Operation: –0°C to +50°C
Humidity	0%–90% non-condensing
Interfaces	USB 2.0 480 Mbps, 3-wire RS-232

Table 3.2: MayaPro2000 USB communication

Pipe	Description	Type	HS Size	FS Size	Endpoint address
0	Endpoint 1 Out	Bulk	64	64	0x01
1	Endpoint 2 In	Bulk	512	64	0x82
2	Endpoint 6 In	Unused	Unused	Unused	Unused
3	Endpoint 1 In	Bulk	64	64	0x81

HS Size corresponds to high speed size in bytes and FS size corresponds to full speed size in Bytes.

pyusb packages. The spectrograph is programmed to work in continuous mode throughout the flight. In this mode, the CCD is constantly being driven at the user specified integration time. When a spectrum is requested via software (i.e., McDAS), the spectrograph electronics wait for the current integration period to expire. Then at the start of the next integration period, the CCD data is readout, which contains the data for photons which were collected by the CCD in the previous integration period. All commands are sent to the Spectrograph through End Point 1 Out (EP1). All the spectral data are acquired through End Point 2 In and all other queries are retrieved through End Point 1 In (EP1). The details of endpoints available for communication with the device is described in table 3.2

The detailed program algorithm is as follows:

- Scan the USB ports for the device.
- Connect to the device with correct vendor id and serial number.
- Get USB speed from the device.
- Initialize the endpoints.
- Get wavelength calibration coefficient, nonlinearity coefficient.
- Set integration time.
- Query for the current status of the device.
- Get pixel, integration time, packets in spectrum, etc from the device.
- If device is ready, request for spectra.
- Check USB speed.
- Transfer spectra through endpoint.
- Check for the sync.

- Extract count vs pixel information from the packets.
- Save counts and pixel information to an array.
- Correct for nonlinearity.
- Wavelength calibration of the spectra with pixel to wavelength mapping.
- Save the data as a text file with the time stamp.
- Go to sleep (predefined) and loop to step vii.

The data is stored on board the flight computer with time stamp for further analysis.

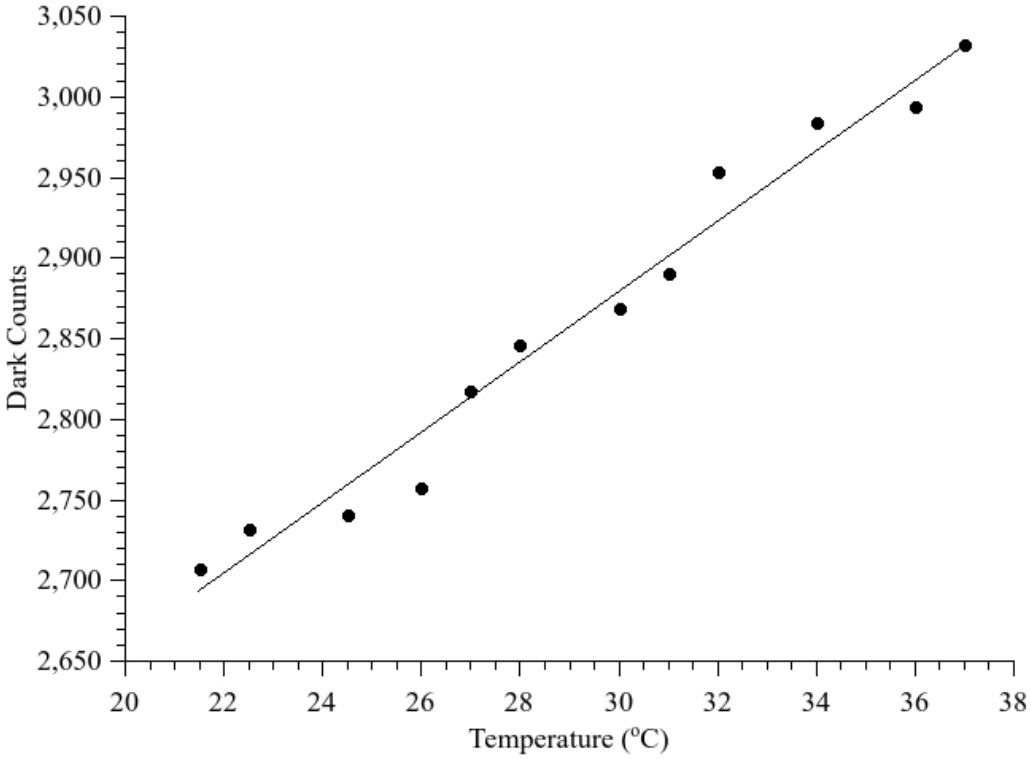

Figure 3.5: Dark counts per second vs. temperature.

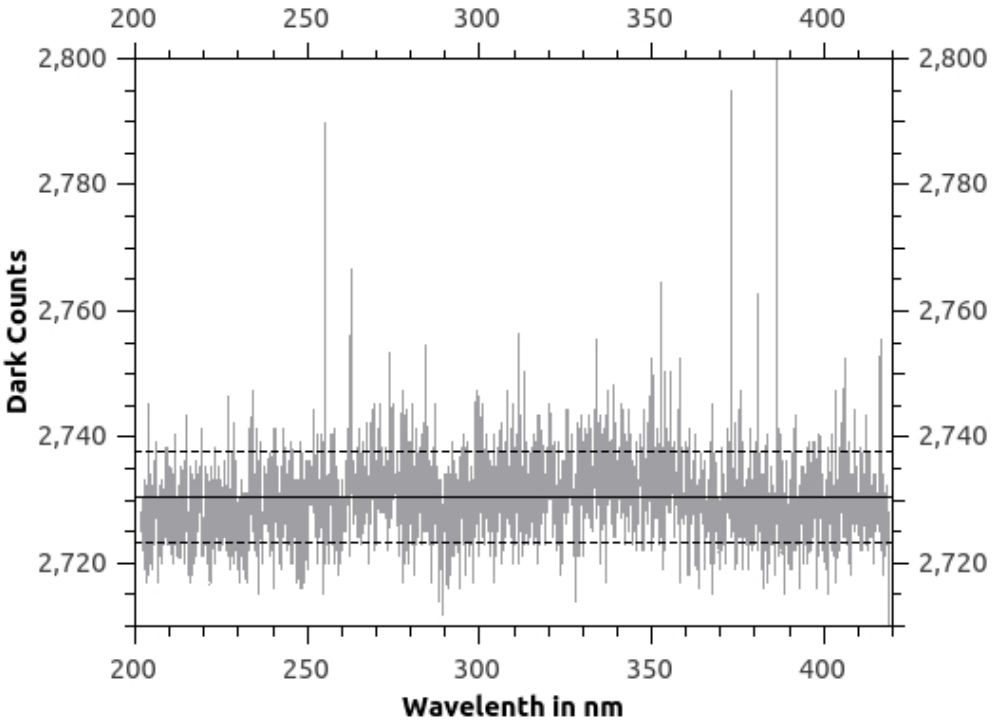

Figure 3.6: Dark counts per second at 25°C. The solid line shows the mean value, and the dotted lines represent the standard deviation.

3.2.1.1 Calibration and testing

Dark count: The dark count rate of the spectrograph was measured in a dark room with the entrance slit covered by a black cap. The temperature sensor (LM75) was placed on the surface of the spectrograph close to the detector side to effectively measure the detector temperature. This test was performed at several different temperatures and found that the dark count varied linearly with the temperature (Fig. 3.5). A typical dark count signal for an exposure of 1 sec at 25°C is shown in Fig. 3.6, where the mean value of the counts is 2730 ± 7.

The dark counts in both flights were measured through observations at wavelengths shorter than 250 nm. Solar UV does not penetrate below 30 km and thus any recorded counts below 250 nm will be due to dark counts (Wolff et al., 2008). comparison of the dark count obtained in the October 2014

flight with that of the lab measurement for an equivalent temperature (28°C) is shown in Fig 3.7. The variation of dark current with temperature followed the same trend as observed in the laboratory (Fig. 3.5).

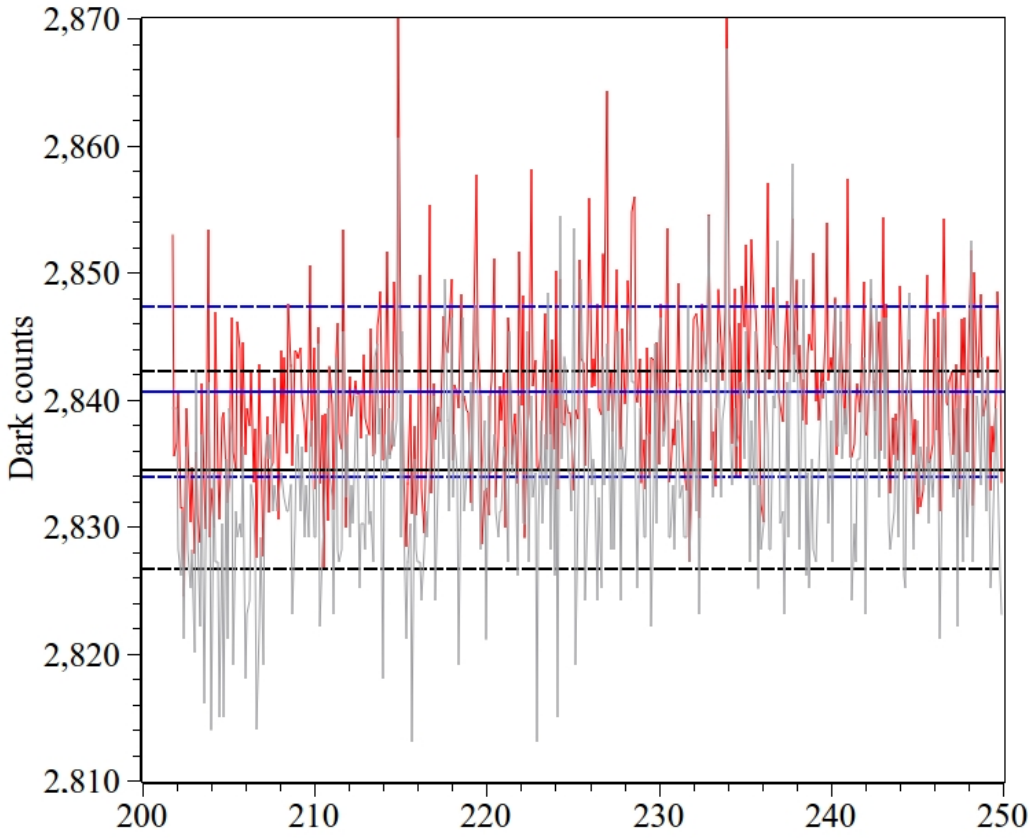

Figure 3.7: The variation of dark signal with wavelength in flight (grey) and in laboratory (red). The solid line represents the mean and the dotted line represents the standard deviation (black for flight data and blue for laboratory measurement at $28°C$.

Wavelength calibration The nominal wavelength calibration of the spectrograph from the manufacturer (Ocean Optics manual, 2009) has a third order relation between the pixel value and wavelength:

$$\lambda_p = I + C_1 p + C_2 p^2 + C_3 p^3 \,, \tag{3.1}$$

where λ is the wavelength at pixel p, I is the wavelength of the 0th pixel, and C_1, C_2, and C_3 are the coefficients. The spectrograph comes wavelength cal-

ibrated from the manufacturer and the vendor provides frequent wavelength calibration upon request.

3.2.2 Attitude Sensor and Other Monitors

We have used a compact MEMS-based attitude sensor described in detail in next chapter to monitor the look direction of the spectrograph. This sensor uses an internal IMU (inertial measurement unit) with an external GPS unit to give the look direction to an accuracy of $\pm 0.24^{\circ}$ in either RA (Right Ascension) and DEC (Declination), or in Earth-centered inertial coordinates (azimuth and elevation).

Environment sensors (temperature, humidity, and pressure) are usually employed to measure the atmospheric parameters during the flight. Two temperature sensors, internal (inside the payload box) and external (outside the payload box), monitor the temperature of the payload. The internal sensor is placed to ensure that the spectrograph remains within its operational temperature. A GPS sensor provides the positional information of the payload. The technical details of the environment sensors are given in Table 3.3. The horizontal camera is a follow-up instrument to verify the look direction of the light-collecting aperture. A second camera is placed vertically to monitor the balloon and records images every 30 sec.

Table 3.3: Details of environment sensors used

Parameter	Sensor	Operating Range	Accuracy
Temperature	LM75	-55°C to $+125^{\circ}$C	$\pm$2K
Pressure	MSR145 FP/020	0 to 2000 mbar	$\pm$2.5 mbar
Humidity	MSR145 FH/020	0% to 100%	$\pm$2%

3.2.3 On-board Computer

The payload is controlled through a Raspberry Pi[5] single-board computer (SBC), running a Linux operating system. The python code (MCDAS[6]) described earlier is used to send commands to the spectrograph and to receive the data through the USB port.

The onboard computer also controls the monitoring hardware (Section 3.2.2) in the payload through the Raspberry Pi's I2C port. The data from the attitude sensor, optical cameras and the environment sensors are stored on-board on SD cards and retrieved after the recovery of the payload.

The payload, along with the instruments, included a radio telemetry unit, batteries, a parachute, and two flight termination units (FTU), as described in previous sections. The light-collecting lens, attitude sensor and an optical camera were placed horizontally with respect to the base of the payload in order to look at the Earth's limb. Another optical camera was placed looking up, recording the images of balloons every 30 sec for balloon monitoring. This helps to keep a record of the time of balloons burst/cutoff, as well as the functioning of the FTU. Power for the instruments was provided by lithium polymer batteries which have flight heritage.

3.3 Experiment

Balloon experiments are being carried out from the CREST campus (13.113°N, 77.814°E) of the Indian Institute of Astrophysics, near Bangalore, India from March 2013. Payload used for each experiment varies depending on the scientific experiment to be carried out. Initial launches were used to check the communication system, the FTUs and all the flight monitoring systems. In the following section, two flights are described, which aimed at carrying out spectroscopic observations of scattered solar light in UV.

[5]Raspberry Pi Foundation, UK

[6]Available as open source at our web page `https://github.com/iiabaloongroup`

Spectroscopic observation of UV scattered light was carried out on two flights in 2014, 15th June and 12th October. The launches were carried out in the morning, when winds were relatively mild. The total weight of payload including the parachute was about 5 kg, which we launched using three latex balloons[7]. Each balloon was filled with 7 cubic meters of hydrogen corresponding to a measured neck lift of 5.5 kg. The ascent rate of the balloons is typically 6 m/s with a final altitude close to 30 km. The balloons usually take around 90 minutes to reach the maximum altitude, therefore the FTU system was programmed to detach the balloon from the parachute after 100 minutes of the flight. Typical descent rate with the parachute is about 4.5 m/s.

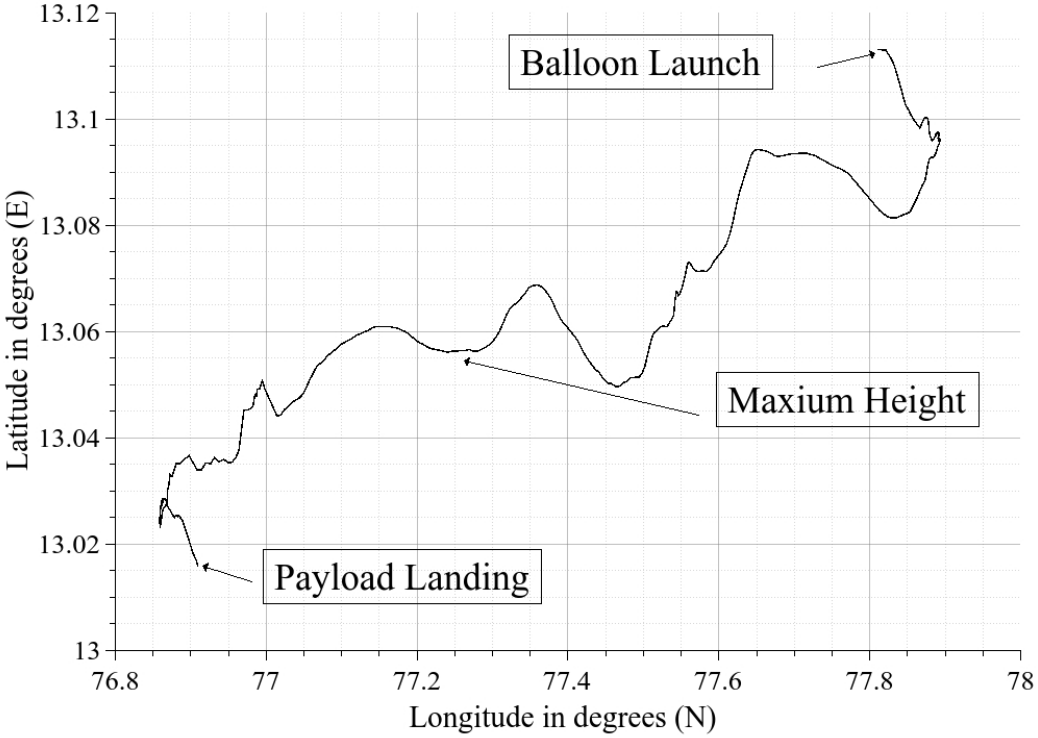

Figure 3.8: Balloon trajectory derived from GPS data for the 15 June 2014 flight.

The ground track for the 15 June 2014 flight was obtained from GPS data (Fig. 3.8) which is accurate to better than 10 meters on the ground,

[7]CPR-2000, Pawan balloons, India

and about 20 – 30 meters in the altitude. The GPS transmitted the position of the payload to the ground station at the CREST campus through a radio link operating at a frequency of 144.8 MHz. We monitored the altitude profile (Fig. 3.9), and the variation of the temperature inside and outside the payload box (Fig. 3.10). The payload experienced oscillations in both azimuth and elevation with an average rotation of $\sim 10^{\circ}$/sec in azimuth and a maximum variation of $\sim \pm 10^{\circ}$ in elevation. The GPS radio tracker failed to provide location information for the October 2014 flight because the antenna broke 10 minutes into the flight. The derived altitude for this flight is calculated using the information of the general trend of ascent rate from previous flights and burst time. The time of reaching the maximum altitude was obtained from the image of the balloon burst/cut-off.

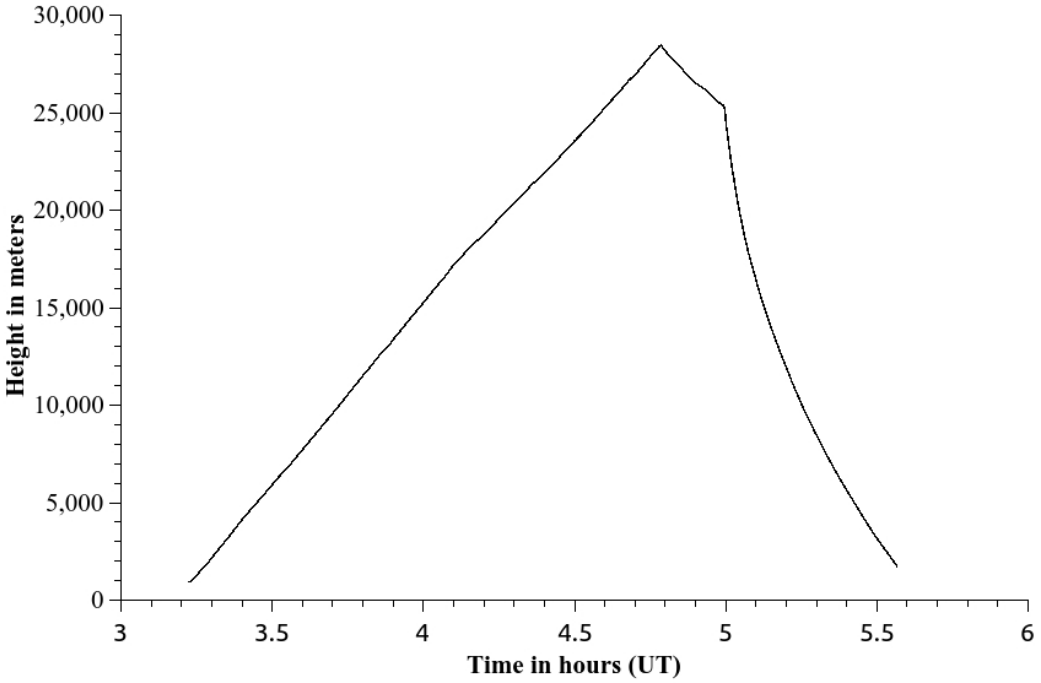

Figure 3.9: Flight height profile on the June 15 2014 flight.

The spectrograph was programmed to record the spectra at every 5 seconds with an exposure time of 1 second. The time-tagged data from the spectrograph are stored on board along with the housekeeping data (payload

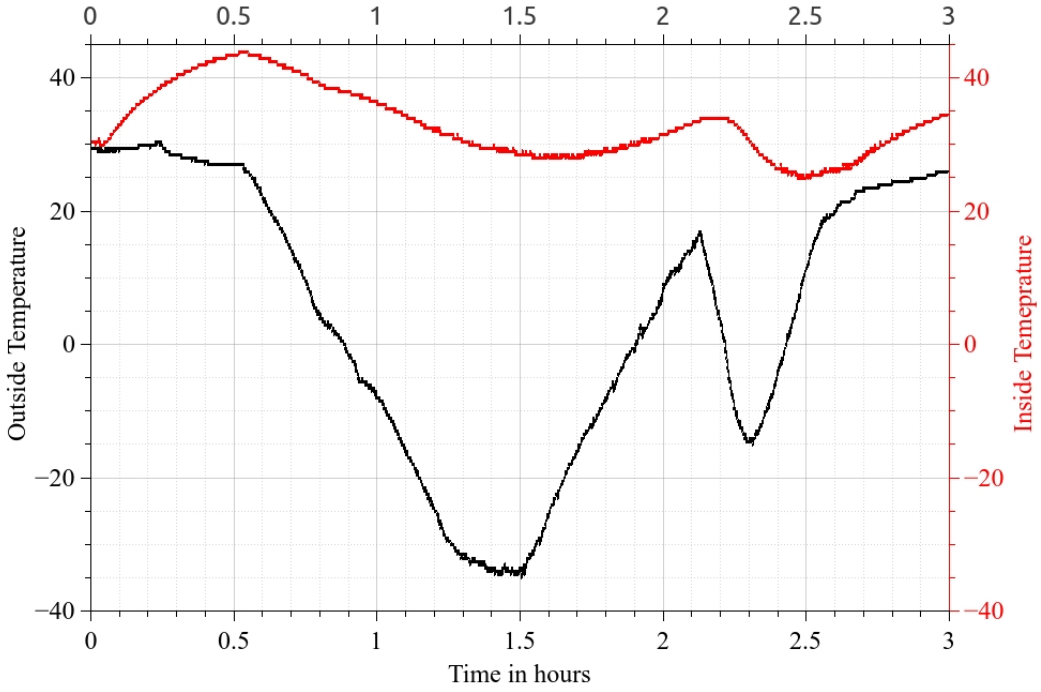

Figure 3.10: Variation of external (black curve) and internal (red curve) temperature during the October 12, 2014 flight. The sensors were switched on 30 mins prior to the launch, therefore, the launch time corresponds to 0.5 hrs in the graph.

orientation and environment sensors) and images from the cameras. These are recovered after launch and analyzed in the laboratory.

3.4 Observations and Results

3.4.1 Scattered Solar Light

The aperture was pointed toward the Earth limb with the solar zenith angle (SZA: the angle between the Sun and the zenith) varying between 53° and 41°. 53° corresponds to the SZA at launch (ground), and 41° corresponds to the SZA at maximum altitude. The observations taken at elevation angles of ±1° and at azimuth angles of around 270° using attitude sensor data are only considered for analysis. The angle from the Sun was further verified with the optical camera.

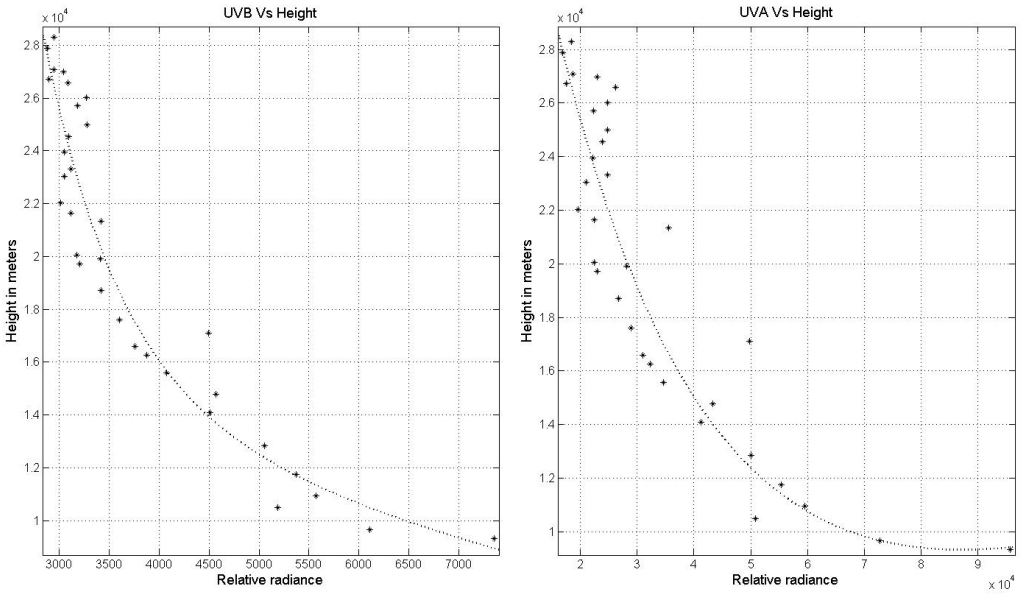

Figure 3.11: Variation of measured radiance with altitude. The lines represent an exponential fit to the data. Note the SZA change from 52 to 41 degrees with increase in altitude for June 15, 2014.

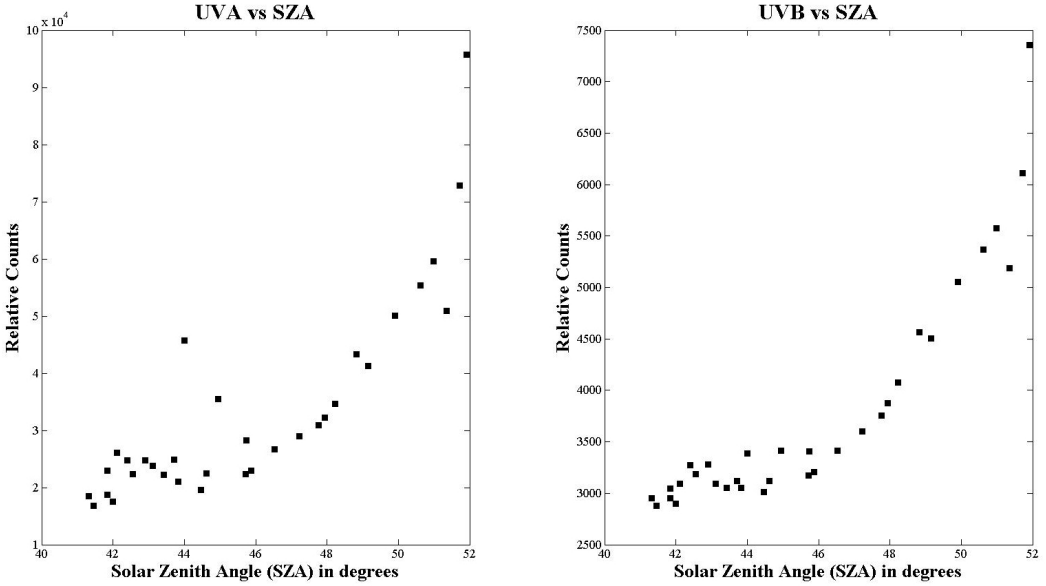

Figure 3.12: Variation of measured radiance with solar zenith angle on the 15 June flight.

The relative flux in two UV bands: UVA (315–420 nm) and UVB (280–315 nm) are calculated, and plotted with respect to the height of observation

(Fig. 3.11). The relative flux in these bands is given by the equation

$$I_{band} = \frac{\Sigma I_{\lambda}}{\Delta\lambda}\,, \tag{3.2}$$

where I_{band} is the intensity in the particular band (UVA/UVB), I_{λ} is the intensity at a particular wavelength and $\Delta\lambda$ is the wavelength band. Fig. 3.11 shows the variation of measured radiance in the two different wavelength bands; the points are the measurements at different heights and the dotted lines represent an exponential fit in agreement with results obtained in Weidner et al. (2005). Here only the data above 10 km is considered; this is because the scattering below 10 km is heavily influenced by cloud cover, and the payload had too much oscillations, which has prevented obtaining any useful results. The SZA does not have a linear relation with the altitude because our payload has lateral movement during the observations. Therefore, the variation of radiance vs SZA is plotted in a separate graph (Fig. 3.12).

Chapter 4

Attitude Sensor

Sreejith, A. G., Mathew, J., et al., J. Astron. Instrum. Vol 03, Issue 02, 1440006 (2014).

4.1 Introduction

Stabilization and pointing are essential requirements for a wide variety of telescopes, instruments, and cameras (Hilkert, 2008). One of the commonly used systems to stabilize and point the telescope are Inertially stabilized platform (ISP). ISPs have been used for more than a century on different types of moving platforms. Applications of such systems include surveillance and tracking, communications, astronomical telescopes, etc. One of the applications for astronomical telescope is the gyro-stabilized system in the Hubble Space Telescope which can achieve milli-arcsecond pointing accuracy (Hilkert, 2008).

The configurations of inertial stabilization and pointing systems can vary depending on the applications of the system. Gimbals are the essential part of an ISP which carry out the stabilization of the payload by motors and bearing assemblies.

4.2 Attitude Determination

One of the main requirements of any ISP is accurate attitude determination, which is discussed in this chapter. The technique of determining the orientation of the payload or spacecraft is termed attitude determination. It is critical in case of satellites to point the solar panels towards the sun, the communication antenna system towards earth, and other sensors/telescopes to the desired directions to satisfy their scientific objective. The attitude is determined by understanding the current pointing of the platform and the previously known position in inertial coordinates.

4.3 Types of Attitude Sensors

Attitude sensors provide the orientation information of the platform and are considered the heart of ISP systems. Different types of attitude sensors have been used in high-altitude balloon experiments: star trackers, sun sensors, magnetometers, accelerometers gyroscopes, etc. to name a few. We describe a few types of sensors in the following paragraph.

4.3.1 Sun Sensors

The sun sensor works by determining the position of the sun. It usually employs an image sensor with some form of imaging optics and calculates the position of the sun in the detector. Sun covers around 0.5° of the sky and hence sun sensors usually works at this accuracy. The brightness of the sun makes it a great choice for attitude determination for most of the earth observing satellites and for airborne and ground-based attitude determination during the day.

4.3.2 Magnetometers

The earth's magnetic field has been used to determine the orientation/direction from ancient times. The use of the magnetic compass for navigation is well known. Different types of magnetometers can be used to measure the strength and the direction of the magnetic field of earth and provide us with an attitude information. The advantage of these systems are that they are lightweight and require low power, but these units suffer from accuracy issues as the exact nature and strength of magnetic field is yet to be determined and are easily affected by other electromagnetic interferences. These disadvantages limit magnetometer usage to low accuracy missions.

4.3.3 Star Sensors

Star sensors are one of the most accurate systems for measuring the attitude at night, provided that we have clear skies. Star sensors are extensively used in satellites for attitude determination. Although they are extremely accurate and reliable, they do suffer from certain disadvantages like complexity, high price, extensive software requirements, etc. These may also be affected by bright sources such as moon, planets and the sun in their field of view.

4.4 Raspberry Pi based Attitude sensor

For our application on high-altitude balloon, it was decided to have a novel approach and decided to build a compact attitude sensor with reliable performance with a commercial inertial measurement unit (IMU), which combines an accelerometer, a magnetometer and a gyroscope on a single chip. The IMU provides attitude information in terms of Euler angles and quaternions (Bar-Itzhack & Oshman, 1985), which is combined on a Raspberry Pi[1] with the output of a global positioning system (GPS) chip to obtain the celes-

[1] http://www.raspberrypi.org

Table 4.1: Raspberry Pi technical specifications (Source: Raspberry Pi user guide, Raspberry Pi Foundation).

Chip	Broadcom BCM2835 processor
CPU	700 MHz Low Power ARM176JZ-F processor
GPU	Dual Core VideoCore Multimedia Co-Processor
Memory	512MB SDRAM
Ethernet	Onboard 10/100 Ethernet connector
USB 2.0	Dual USB connector
Video Output	HDMI composite RCA
Audio Output	3.5mm jack, HDMI
Onboard Storage	SD, MMC, SDIO card slot
Weight	45 gms
Power Rating	700 mA (3.5 W)
Operating System	Raspbian
Dimensions	8.6cm x 5.4cm x 1.7cm

tial coordinates of the pointing direction. The construction of a lightweight compact attitude sensor has become much simpler in recent years due to the replacement of mechanical devices by solid state devices such as, for example, micro-electromechanical systems (MEMS). The details of the development of this novel Raspberry Pi-based attitude sensor which uses onboard data fusion is described in this chapter.

4.4.1 Hardware and Implementation

The attitude sensor was built around a Raspberry Pi, a small-size single-board computer (SBC) developed by the Raspberry Pi Foundation (technical specifications in Table 4.1). The Raspberry Pi and similar SBCs (e.g. the Arduino) provide flexible, low-cost platforms to which different devices may be connected, and which have been used in a number of innovative ways from home automation systems to aeronautical communication devices (Sabastian et al., 2012).

The photograph of the sensor, along with an SD card for scale, is shown in Fig. 4.1, *Left*, and its functional block diagram is shown in Fig. 4.1, *Right*.

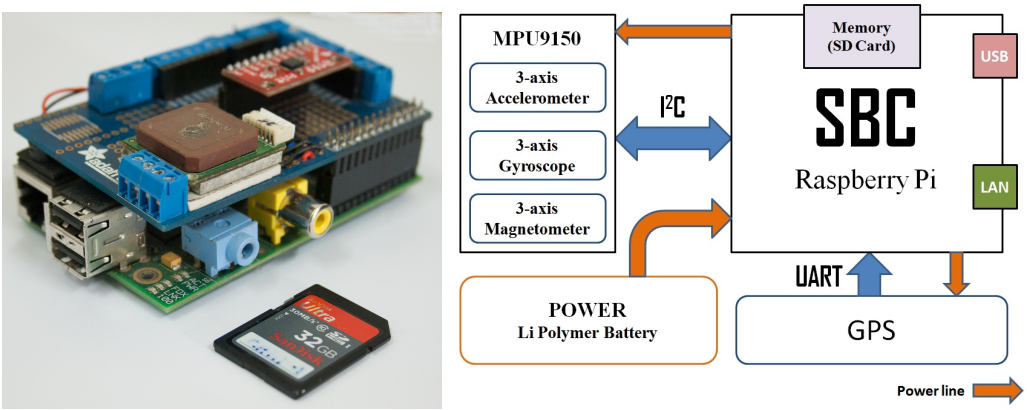

Figure 4.1: Attitude sensor. *Left*: Assembled attitude sensor with an SD card for scale. *Right*: Functional block diagram of the attitude sensor.

The 9-axis MEMS IMU (MPU-9150[2]) which contains two chips, the MPU-6050 comprising a 3-axis gyroscope, an accelerometer, and a digital compass (Ak8975), and a Digital Motion Processor (DMP) is used for the development of attitude sensor. This IMU is commonly used in a variety of commercial applications including mobile phones, tablets, and gaming platforms. Gyroscopes are included because the accuracy of accelerometers and magnetometers is satisfactory only when the system is stationary and far from induced random magnetic fields (Ayub et al., 2012), whereas gyroscopes provide a fast response to changes in orientation while being independent of magnetic fields. The MPU-9150 uses the proprietary InvenSense Digital motion fusion™ and runtime calibration firmware to combine data from the accelerometer and the gyroscope onboard the chip.

The MPU-9150 has user-programmable settings for the gyroscope with ranges of ±250, ±500, ±1000, ±1000 and ±2000 °/sec (dps), for the accelerometer with ranges of ±2 g, ±4 g, ±8 g and ±16 g, and a single setting of $\pm 1200 \mu T$ range for a compass. For our application the acceleration experienced by the payload does not exceed 2 g as was observed in all of our previous flights, therefore the default ±2 g settings for the accelerometer and the default value of ±2000 *dps* for the gyroscope was selected in the implementation

[2]InvenSense Inc, USA (http://www.invensense.com/mems/gyro/mpu9150.html)

of attitude sensor.

The data from the sensors are digitized by three 16-bit analog-to-digital converters (ADCs) for the gyroscope, three 16-bit ADCs for the accelerometer and three 13-bit ADCs for the magnetometer. The data stream from the MPU-9150 is fed into the I^2C (Inter-Integrated Circuit) port of the Raspberry Pi. This port is a multi-master serial single-ended computer bus, through which low-speed peripherals are attached to the motherboard using bidirectional open drain lines SDA (Serial Data Line) and SCL (Serial Clock) with pull-up resistors. The DMP application processor performs the sensor fusion by integrating the output from the gyroscope and accelerometer and generates the quaternions (by InvenSense licensed codes inside the DMP) output which can be read out from the First-In-First-Out (FIFO) registers by the SBC. Since now the sensor timing synchronization and sensor fusion computations are carried out by the DMP, the total load on Raspberry Pi is reduced.

One of the great advantages of the Raspberry Pi is the extensive library of open-source programs available for the platform. The open source code *linux-mpu9150* (developed by the Pansenti software consultancy and development company[3]) was used to read the data from MPU-9150, combine the magnetometer data with the data from the two other sensors, and calculate the attitude information in terms of Euler angles.

The Euler angles give the orientation of the sensor relative to an Earth-centered inertial frame (ECI), which we convert to celestial coordinates using the position data (latitude and longitude of the payload) obtained from the GPS sensor. The GPS of choice is a 20-channel GPS receiver from iWave[4] operating in the L1 frequency band (1575.42 MHz), which gives accuracy better than 10 meters on the ground and 20-30 meters in altitude. The data from the GPS sensor is transmitted to the Raspberry Pi through the Pi's Universal Asynchronous Receiver/Transmitter (UART) port (Fig. 4.1, *Right*)

[3] `https://github.com/richards-tech/linux-mpu9150`

[4] iWave Systems SiRF StarIII GSC3f GPS receiver, iWave Systems, India (http://www.iwavesystems.com)

serially at the rate of 9600 bps. The entire system is powered by a 5 V lithium polymer battery. A C code reads the GPS values and combine the Euler angles with the GPS values to calculate the orientation information in Right ascension (RA) and Declination (Dec) and write the output to a file on an SD card.

4.4.2 Description of the Software

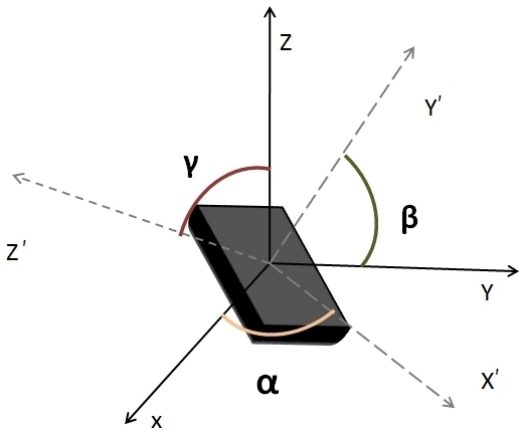

Figure 4.2: Attitude sensor reference frame. The axes x, y and z define the ECI reference frame. The axes x', y' and z' define body-centered reference frame. Angles α, β and γ are the Euler angles.

The code reads the data from the MPU-9150 and calculates the Euler angles. Here, the data fusion from accelerometer and gyroscope is done on-board the MPU-9150 while the magnetometer data fusion is done in the main code. The code operates by opening the I^2C bus for communication between the Raspberry Pi and the MPU-9150. It then reads the data from the IMU and uses the Euler angle transformation (Pio, 1966) to calculate the yaw α, pitch β, and roll γ angles (Fig. 4.2). The roll and pitch angles are derived from the accelerometer and gyroscope output, and the yaw readings from the magnetometer. The accelerometer + gyroscope data are saved in the form of quaternions, which are then read from the DMP FIFO registers to calculate

Euler angles using the following formulas

$$pitch(\beta) = \arcsin(2 \times (ac - bd)) \,, \tag{4.1}$$

$$roll(\gamma) = \arctan\left\{\frac{2 \times (cd + ab)}{1 - 2 \times (b^2 + c^2)}\right\}, \tag{4.2}$$

where a, b, c, d are the quaternions. After that, the magnetometer output is used to calculate the yaw angle,

$$yaw(\alpha) = \arctan\left\{\frac{MagY}{MagX}\right\}, \tag{4.3}$$

where MagY and MagX are the Y-axis and X-axis magnetometer readings, respectively. Settings of ±2000 dps and ±2 g are used for gyroscope and accelerometer, respectively. *linux-mpu9150* is modified to calculate the equatorial coordinates (RA and Dec) of the pointing by combining the IMU and the GPS data (the source code is available at the following address: `https://github.com/iiabaloongroup`). The code calculates the elevation *Alt* and azimuth *Az* of the horizontal coordinate system, which defines the absolute pointing of the sensor with respect to an Earth-centered coordinate system, from the Euler angles. The latitude ϕ and longitude l of the payload and the current universal time (UTC) are then read from the GPS module using the National Marine Electronics Association (NMEA) protocol over the UART port. The local sidereal time (LST) of observation in degrees is then calculated from the UTC by

$$\mathrm{LST} = \mathrm{GMST} + \mathrm{UTC} \cdot 15.0 + l \,, \tag{4.4}$$

where GMST (Greenwich Mean Sidereal Time) in degrees is

$$289.9404 + 4.70935 \times 10^5 \cdot d + 356.0470 + 0.9856002585 \cdot d + 180 \,, \tag{4.5}$$

and quantity d is calculated from the date information YYYY-MM-DD as

$$d = 367{\cdot}\text{YYYY} - \frac{7}{4}\left(YYYY + \frac{MM+9}{12}\right) + \frac{275\cdot MM}{9} + DD - 730530.0 + \frac{\text{UTC}}{24}\,. \tag{4.6}$$

After LST is calculated, the equatorial coordinates RA and Dec are obtained from the following formulae

$$Dec = \arcsin\left\{\sin\left(Alt\right)\sin\phi + \cos\phi\cos h\cos\left(Az\right)\right\}, \tag{4.7}$$

$$HA = \arccos\left\{\cos\phi\sec\left(Dec\right) - \tan\left(Dec\right)\tan\phi\right\}, \tag{4.8}$$

$$RA = LST - HA\,, \tag{4.9}$$

where HA is the hour angle. The output of the attitude sensor contains the following information: equatorial coordinates (RA and Dec) of the source, the current time in UTC, GPS coordinates (latitude and longitude) of the payload, azimuth and elevation of the pointing direction. The flowchart of the complete algorithm is presented in Fig. 4.3.

4.4.3 Attitude Sensor Calibration

4.4.3.1 Initial calibration

The sensor must be calibrated before its first use at a given location by slowly moving it through a range of azimuths and elevations. The program *linux-mpu9150* finds the direction of the magnetic North from the magnetometer values and the local gravitational field vector through the accelerometer output, and then internally defines a local Earth-centered coordinate system. This calibration is sensitive to the local magnetic fields and is affected by the presence of nearby ferric objects, for example, the telescope mount and, therefore, has to be repeated for any change of local conditions.

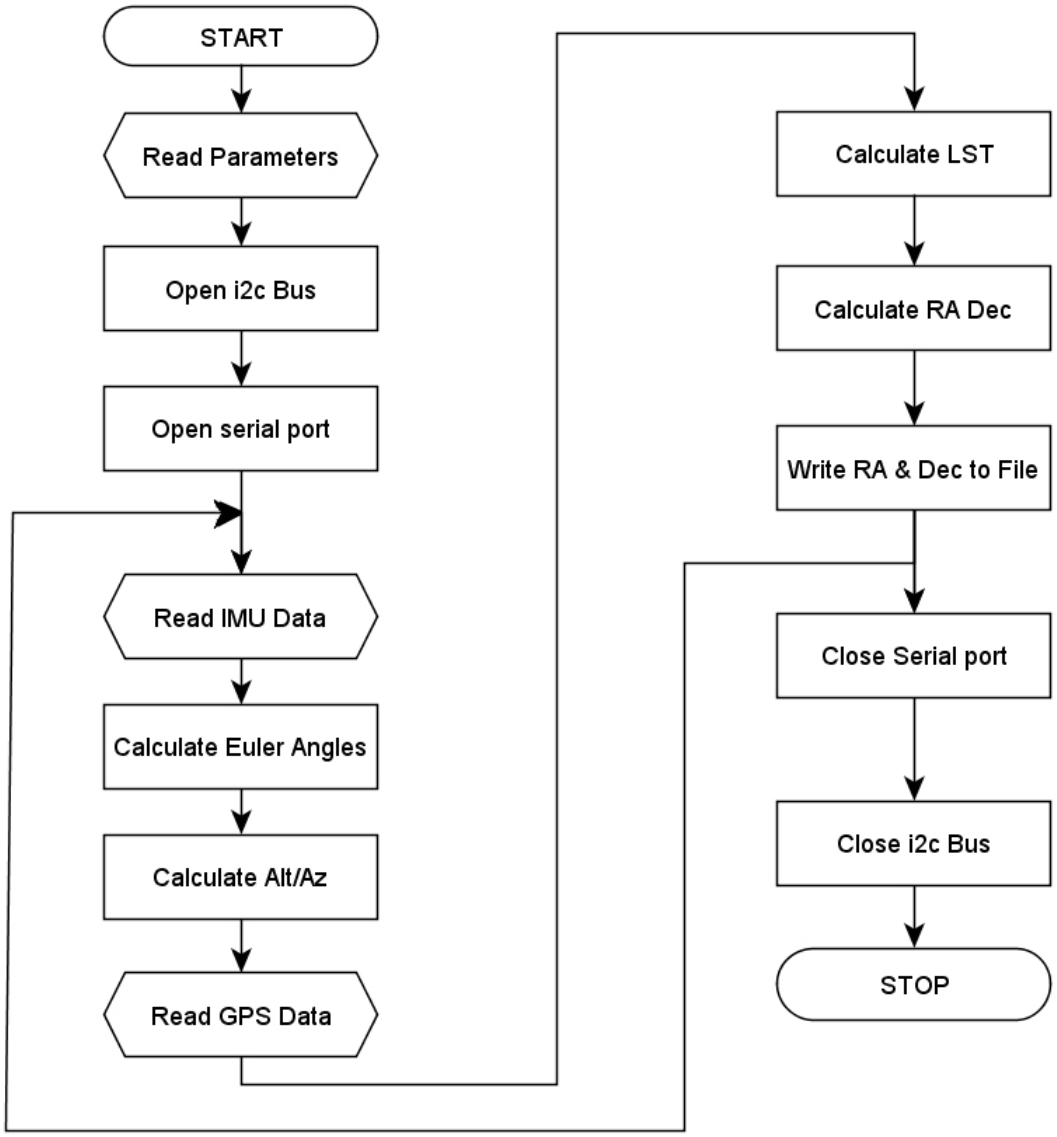

Figure 4.3: Flowchart of the attitude sensor code.

4.4.3.2 Gyroscope calibration

The attitude sensor can operate in two modes: with and without the magnetometer. The initial testing of the sensor was carried out without the magnetometer. The test involved measuring the drift in elevation and azimuth over a period of 10 hours. A drift of about one arc minute per hour was observed in elevation values which was well within our accuracy limits (see Fig. 4.4, *Top*). The drift was much higher in azimuth (Fig. 4.4, *Bottom*) – almost 150 de-

grees in 10 hours, which is unacceptable for our applications. These drifts are due to two sources of errors — bias (Groves, 2013) and integration errors (Borenstein et al., 2008; Shiau et al., 2012), that arise because of manufacturing limitations of the MEMS gyroscopes (Borenstein et al., 2008; Shiau et al., 2012). Drifts that are due to the integration errors are linear and can be easily modeled. However, bias errors are due to the intrinsic instability of the gyroscopes and exist even when the gyroscopes are not rotating. In an ideal case one would expect the bias error to be zero, or at least constant, which can be compensated for by subtracting the bias from the output, but in practical situations, the bias error varies with each operation of the sensor due to changes in the environment. These errors can be avoided by using higher-precision gyroscopes, such as optical or mechanical ones. However, MEMS gyroscopes have major advantages in having a lower power consumption, a shorter start-up time, and being smaller, lighter and cheaper. Bias errors are usually corrected using other sensors (such as accelerometers) in tandem with MEMS gyroscopes. In situations where accelerometers give a constant value (or zero) (e.g. in yaw angle measurements where there is no acceleration in the z-axis), these errors can be avoided by using a fixed external reference — the magnetometer (Fig. 4.5).

4.4.3.3 Magnetometer calibration

The magnetometer in the IMU was found to have a nonlinear response (Fig. 4.6) leading to an error of 5 to 10 degrees in azimuth pointing due to cross-field effects and hysteresis (Pang et al., 2013). To measure the nonlinearity, the sensor was mounted on a 3.5-inch Meade ETX 90 reflector telescope which was rotated by 360 degrees. Sensor values and actual rotation (from the telescope markings) at different positions were noted and used to generate the output. The measured nonlinearity was fitted with a fifth-degree polynomial and the corrections were incorporated into our processing algorithm to produce a linear output. This nonlinearity is sensor dependent and must be

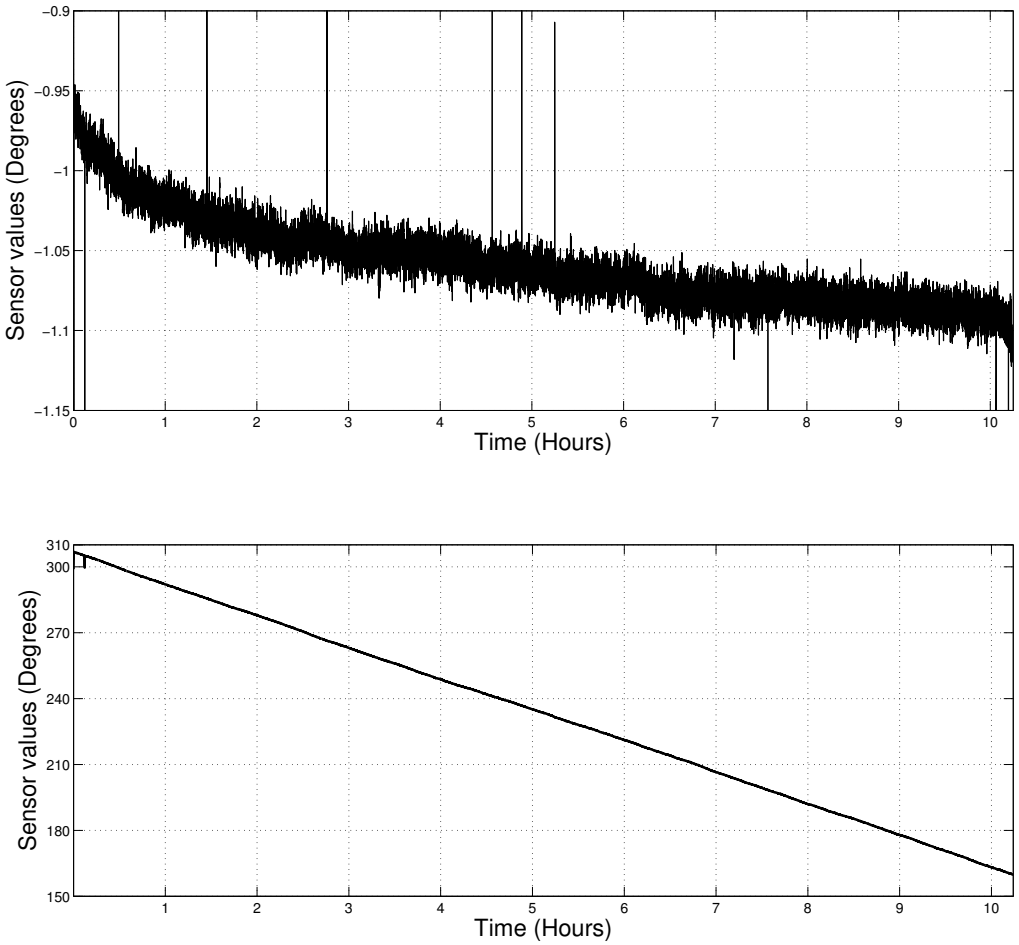

Figure 4.4: Results of the sensor calibration without the magnetometer. *Top*: drift in elevation, *Bottom*: drift in azimuth.

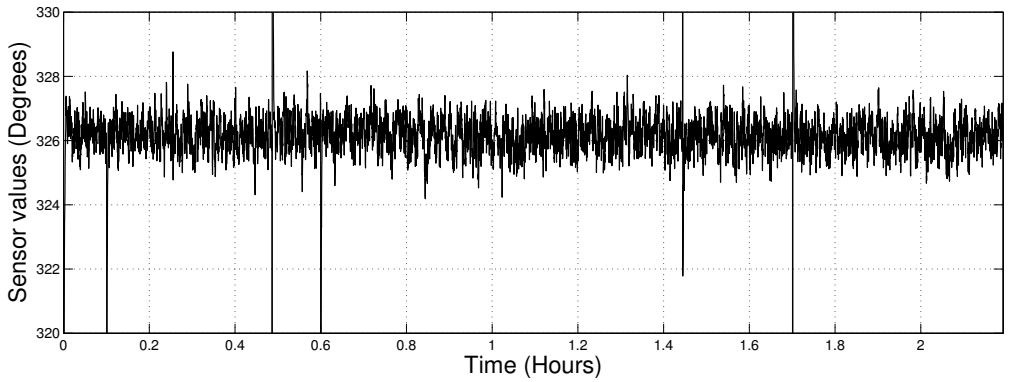

Figure 4.5: Results of the sensor calibration with the magnetometer. There is now no drift in the azimuth.

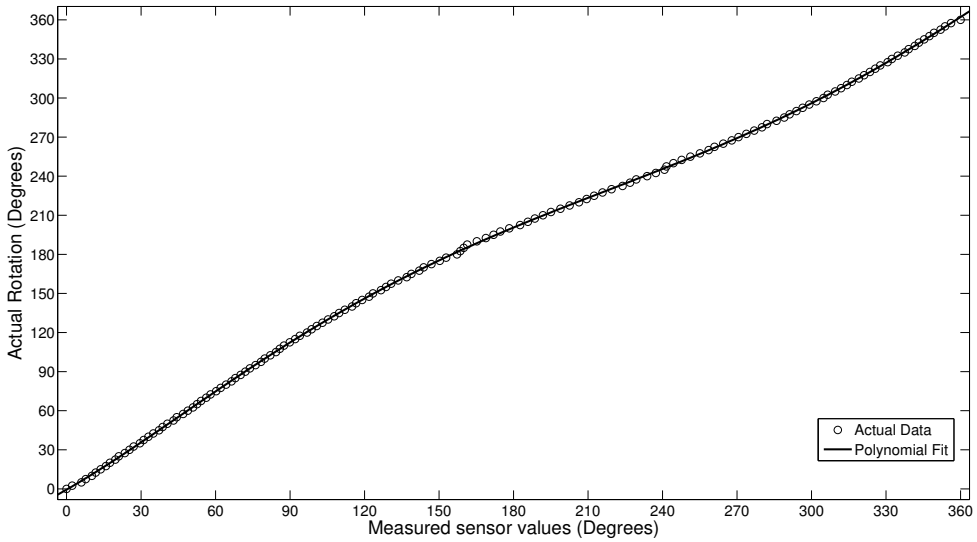

Figure 4.6: Magnetometer nonlinearity.

corrected for each sensor.

4.4.3.4 Pointing calibration

The pointing accuracy of the sensor was tested as part of its calibration. The sensor was mounted on a 3.5-inch Meade ETX 90 reflector telescope and pointed to several known objects in the sky. The same object was observed several times for different elevations. The differences between the actual values and the measured sensor values and the errors are given in Table 4.2. The average of RMS errors was found to be 0.479 degrees. This test helps to determine the reproducibility and the accuracy of sensor pointing. The limiting factor in accuracy for both RA and Dec is due to large errors in azimuth values. These errors occur due to the intrinsically poor magnetometer accuracy (Pang et al., 2013), which is ultimately the limiting factor in the overall pointing accuracy of the sensor. A better accuracy may be obtained if *North* is defined independently without the magnetometer, however in this case, the gyroscope introduces a drift due to bias errors, as discussed earlier.

To test the reproducibility of the sensor output, the readily available Goniometer Stages from Newport™ (with accuracy of 10′), and Thorlabs™ (with

Table 4.2: Results of the absolute pointing calibration. The values are in DD:MM:SS. The average RMS error is in degrees

Object	RA J2014.15	Dec J2014.15	Observed RA	Observed Dec	Average RMS Error
Capella	79:25:60	46:00:3	78:46:17.1 78:54:14.3 79:27:42	46:05:32.5 45:28:25.5 46:34:29.1	0.56
Menkalinan	90:08:30	44:56:50	89:40:22 89:43:48.8 89:47:13.1	44:52:53.9 44:43:41.3 44:34:22.4	0.38
Aldebaran	69:10:60	16:30:31	69:13:29.8 69:32:51.9 69:47:40.9	16:46:00.3 16:58:48.8 16:12:49	0.53
Rigel	78:48:15	-08:11:11	78:36:30.2 78:26:08.1 78:57:53.2	-08:15:59.9 -07:48:12.6 -07:53:41.5	0.38
Jupiter	101:30:29	23:14:44	101:39:16.9 101:38:32.3 101:16:35.4	22:37:45.8 22:45:58.3 22:54:22.1	0.53

accuracy of $1'$), to move the sensor in the y-axis (tilt) and z-axis (pan) was used. Sensor readings were taken at some predefined values of azimuth and elevation (pointing). After random movement of the stages, the sensor was brought back to the initial pointing and the readings were recorded. This step was performed five times in total for several different directions. The results are summarized in Table 4.3.

It was found that the standard deviation of sensor values in elevation (due to accelerometer and gyroscope) and azimuth (due to magnetometer) were around $0.01°$ and $0.24°$, respectively. Since the accuracy of the Goniometer Stage Newport™ is $10'$, this value can be assumed to be overall accuracy in elevation measurement (which is within the absolute pointing accuracy, see Table 4.2). The accuracy of GPS is around $10''$ and introduces much less error to the attitude sensor.

Table 4.3: Results of relative pointing. The given values are in degrees. Az is Azimuth and Ele is Elevation

	Az	Ele	Average Az	Average Ele	Standard deviation (Az)	Standard deviation (Ele)
Set 1	252.5326	1.1952				
Set 2	252.1189	1.1983				
Set 3	252.2308	1.1706	252.3917	1.1868	0.23904	0.0108
Set 4	252.7191	1.1876				
Set 5	252.3570	1.1853				
Set 1	307.5729	-09.9565				
Set 2	307.3201	-09.9624				
Set 3	307.4700	-09.9614	307.3638	-09.9612	0.2077	0.0042
Set 4	307.4264	-09.9593				
Set 5	307.0294	-09.9674				
Set 1	29.9928	09.9897				
Set 2	30.0042	09.9604				
Set 3	30.3929	09.9699	30.0712	09.9753	0.2523	0.0109
Set 4	30.4891	09.9769				
Set 5	29.7343	09.9793				
Set 1	347.1065	06.6215				
Set 2	346.4374	06.6384				
Set 3	346.6514	06.6102	346.6744	6.61822	0.2581	0.0123
Set 4	346.5242	06.6096				
Set 5	346.6524	06.6114				

4.4.3.5 Thermal dependence of the sensor

According to the manufacturer's specifications, the operational range of MPU-9150 is between $-40°C$ and $+60°C$. Since the ambient temperature in the stratosphere can reach $-60°C$, the effect of temperature on other electronics components, such as the GPS module and the SBC have to be tested. From one of our previous high-altitude balloon flights, it was found that the GPS module fails to operate below $-40°C$. In addition, it is well known that the performance of lithium polymer batteries reduces at low temperatures, with $-20°C$ being the limit of a good performance (e.g., Ji et al. (2013)). The sensor was kept in an insulated box in a thermal chamber ($-18°C$) for more than two hours. The temperature in the box was maintained above $-10°C$

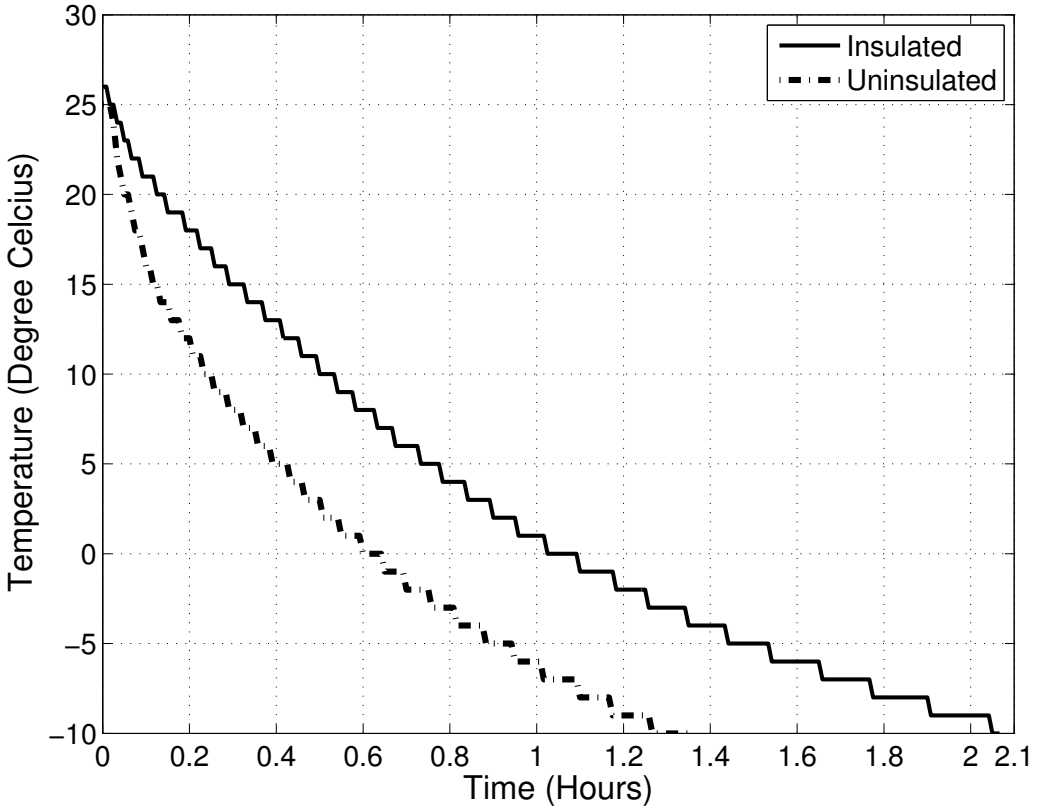

Figure 4.7: Temperature test. Solid line — temperature variation in an insulated box. Dashed line — temperature variation in the un insulated sensor.

for 2 hours. When the sensor was placed in the chamber uninsulated, the recorded temperature dropped to $-10°C$ in almost one hour (Fig. 4.7, dashed line). This indicates that it is necessary to properly insulate the equipment in the balloon experiments. From our flight experience, it was found necessary to balance the internal heating from the electronics with the heat loss from the payload and have experimented with insulated boxes with openings of different diameters to ensures that the temperature is within the allowable range.

4.5 Flight Results

This attitude sensor was flown on several high-altitude balloon flights from our launch facility at CREST campus of Indian Institute of Astrophysics (13.1131

N, 77.8113 E). The aim of these experiments was to test the pointing accuracy of a commercial aerial photography mount, intended for astronomical observations from balloons. In Figs. 4.8 and 4.9 the output of the sensor for the flights conducted on October 13, 2013 and February 16, 2014, respectively are presented. The weight of the payload on the October flight (comprising aerial photography mount with the IMU, attitude sensor, temperature sensors, camera, radio GPS tracker and GSM-GPS tracker) together with the parachute was 5400 grams, and it was carried by two 3000 gms sounding balloons. The balloons were expected to rise above 25 kms at a speed of around 5 m/s, according to the manufacturers' specifications. The balloons rose to a height of about 22 kms in 2 hours after which we believe one balloon has burst. The remaining balloon attained a state of neutral buoyancy, causing it to float at about that altitude for more than 12 hours, carrying the payload along, as the cut-off mechanism to detach the parachute from the balloons failed. The payload was tracked by radio till it crossed over to the Arabian sea, around 400 kms west of the launch site. The payload was later partially recovered by Indian fishermen from the Arabian sea. While the aerial photography mount with its data was lost, the attitude sensor data was recovered and analyzed. The results of the analysis are as in Fig. 4.8. Oscillations in azimuth values (Fig. 4.8, *Top*) indicate that the payload experienced spinning motion during the entire flight with a frequency of 50 degrees in 2–3 minutes, and the elevation values (Fig. 4.8, *Bottom*) indicate that the payload was experiencing swinging motion with a frequency below 2 degrees for the entire flight.

The payload on the February flight (UV spectrograph, attitude sensor, temperature sensors, camera, radio-GPS tracker and GSM-GPS tracker) together with the parachute weighed 5400 gms and was carried by three 2000 gms sounding balloons. The balloons reached the maximum height of 26.9 kms in 2.5 hours. The balloons burst at that altitude and the payload was successfully recovered around 100 km from the launch site. There was much more turbulence on the second flight (Fig. 4.9) mainly because of the use

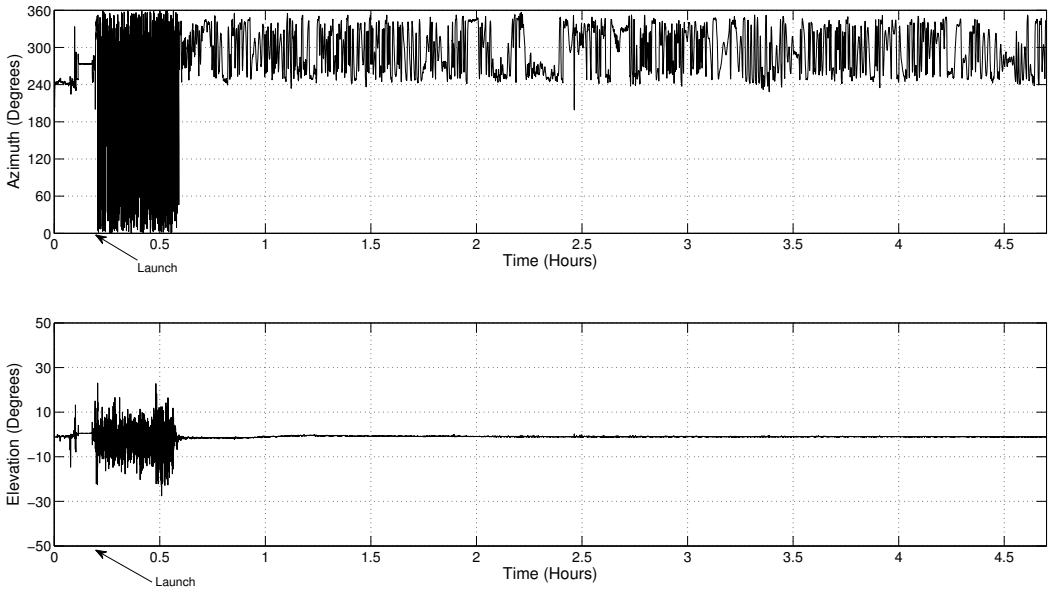

Figure 4.8: Attitude sensor data from balloon flight on October 13, 2013. X-axis is time of the balloon flight in hours. *Top*: Azimuth values, *Bottom*: Elevation values. The sensor was switched on at 0.0 hours and the balloon was released at 0.2 hours. The large variations in both azimuth and elevation values till 0.2 hours are due to the handling of the payload on the ground.

of three balloons instead of two and a stormy weather. The change in frequency of swinging and swaying of the payload as it crossed the tropospheric boundary at around 1.2 hours from the start is clearly visible in Fig. 4.9.

The attitude sensor was flown on these flights in order to test its working in flight conditions and to determine the movement of the payload due to winds.

4.6 Conclusion and Pointing system

The development and calibration of a novel low-cost attitude sensor which can be built with readily available commercial components are described in this chapter. The overall accuracy of the developed sensor was found to be $\pm 0.25^{\circ}$ due to the intrinsic errors in the sensors. This accuracy can further be improved by operating the attitude sensor without the magnetometer, defining the initial *North* direction prior to the launch by other means and correcting

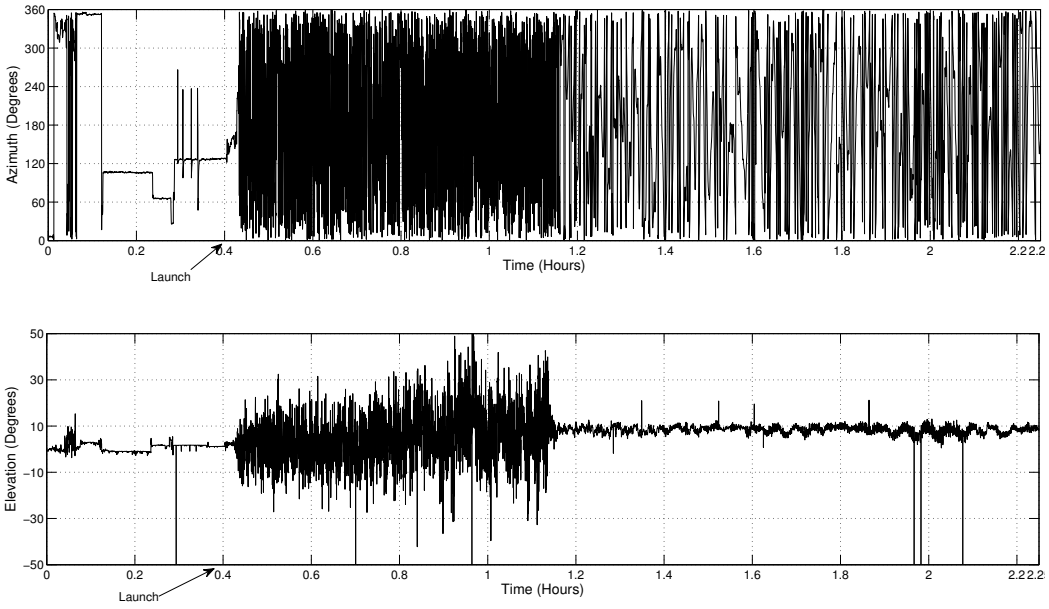

Figure 4.9: Attitude sensor data from balloon flight February 16, 2014. X-axis is time of the balloon flight in hours. *Top*: Azimuth values, *Bottom*: Elevation values. The sensor was switched on at 0.0 hours and the balloon was released at 0.4 hours.

for the gyroscope errors (Sec. 4.4.3.2) in the algorithm. The accuracy of the system can also be improved by using high-precision, but more expensive, magnetometers, accelerometers and speed sensors (Gebre-Egziabher et al., 2004). However, the current sensor can be used for initial coarse pointing on a stabilized platform.

The sensor fusion employed in the algorithm has been taken from already available open-source codes. It will be worthwhile to develop data filtering and data fusion algorithms of our own, which may improve the accuracy of the sensor. The experience gained in the development and testing of this device will further enhance our ability in the development of similar, yet more complex, systems. The attitude sensor described here as been used as a building block in a closed-loop pointing and stabilization platform for balloon-borne payloads (see Fig. 4.10), where the attitude information provided by the attitude sensor is used for coarse pointing of the payload.

The pointing system uses Arduino based controller with same code/ algorithm described in this chapter. The correction in azimuth and elevation are

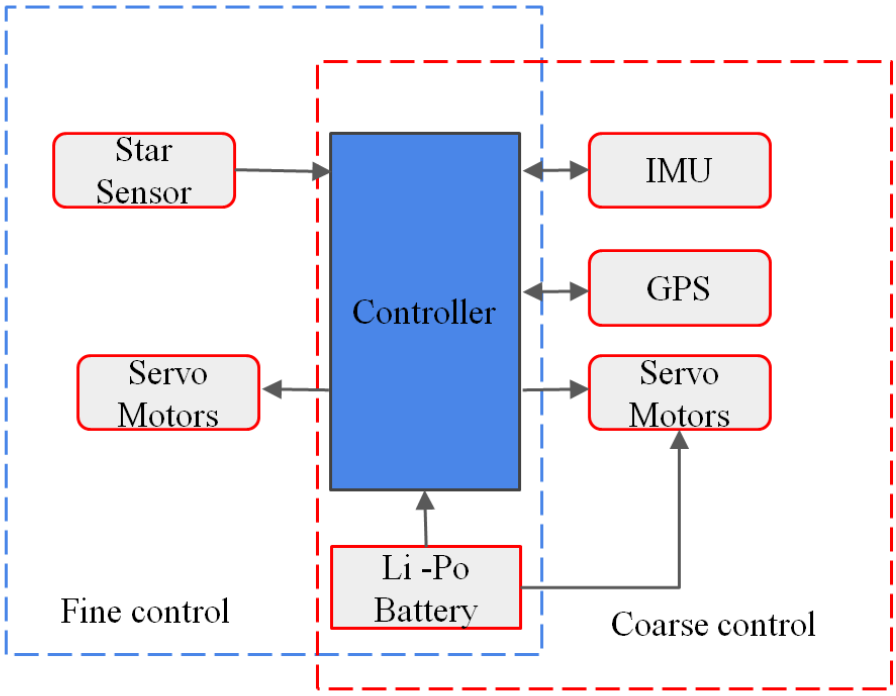

Figure 4.10: The block diagram of the pointing system.

carried out with the help of DC servo motors of required torque (The torque required varies based on the payload to be used). The controlling of the motors is based on a PID loop fine tuned to give a fast and stable response for fast and slow variations of the payload.

The system performance of the pointing system was checked on the ground and in tethered flights with satisfactory results. The pointing system can point to an accuracy of $\pm 0.28^{\circ}$ and track objects from the ground with an accuracy of $\pm 0.13^{\circ}$. The performance in the tethered flights was poorer (0.40° in best conditions), largely because of strong winds at low altitudes.The ground observations of the pointing system are as in Fig. 4.11.

Further fine pointing can be achieved by the inputs from a star sensor developed by our group (see Nirmal et al. 2016 and Sarpotdar et al. 2017). The star-sensor is a highly sensitive, wide FOV optical imaging camera. The front end optics of the star sensor constitutes a four-element Tessar lens sys-

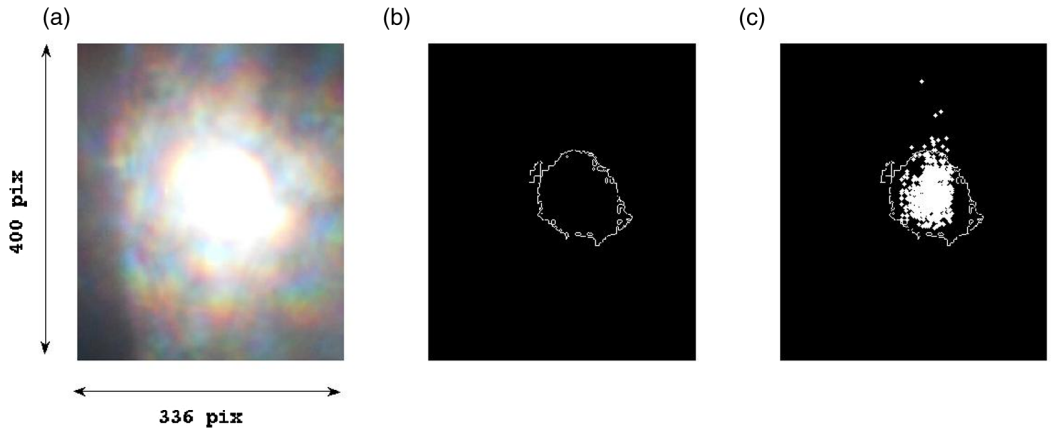

Figure 4.11: (a) An image frame of the Sun, extracted from the video captured during the ground test. (b) The isophot of the Sun's image scaled by 250:1. This isophot was used to find the centroid of the image. (c) The isophot of the Sun with over-plotted centroids calculated for every image frame. The size of the image is marked in pixels. The third image shows the accuracy information of pointing system from the ground, as it is clear from the image that the centroids mostly lie within the isophot which corresponds to $\pm 0.25^{\circ}$, i.e., the angular width of the Sun in the sky (image credits: Nirmal et al. (2016)).

tem custom designed to reduce chromatic aberration, coma, and distortion. The star sensor operates by observing stars brighter than visual magnitude of 6. It requires at least 3 stars in the FOV, in any field of the sky to provide us with orientation information to accuracy in arc seconds (see Sarpotdar et al. 2017).

Our team is also working on adding an extra axis control to create a 3-axis, fully autonomous inertial pointing system. These will find application in aerial photography and other stabilized systems apart from the high-altitude balloon application. The complete details of this pointing system is beyond the scope of this thesis and will be discussed in a future thesis from our group.

Chapter 5

Trace Gas Analysis with DOAS Technique

Sreejith, A. G., Mathew, J., et al., Atmos. Meas. Tech. Discuss amt-2016-98., doi:10.5194/amt-2016-98, 2016.

5.1 Introduction

Trace gas analysis is an important tool in atmospheric studies. The antarctic ozone depletion discovery in 1985 by Farman et al. (1985) was a shock in atmospheric research as the ozone depletion in polar region was much more than anticipated by scientific community. These observations highlighted the effects of human activities on the fragile nature of our earth's atmosphere. The role of ozone layer for the protection of humans and other biological species from UV radiation has been well documented from as early as the 19th century (Cornu, 1879; Hartley, 1881). The discovery of destruction of stratospheric ozone led to an increase in research activities to better understand and control these effects.

The scientific community previously had an idea about the effects on ozone layer due to the emissions of nitrites and halides into the atmosphere as

discussed in Crutzen (1970); Molina & Rowland (1974), but the intensity of destruction of ozone was unexpected. The discovery of ozone hole in antarctic lead to more extensive research for better understanding of the formation of the ozone hole (for example: Crutzen & Arnold (1986); Solomon et al. (1986); Toon et al. (1986)). Chlorofluorocarbons (CFC) were identified as the main cause of ozone layer depletion and their production was reduced or regulated and later stopped by the Montreal Protocol of 1987 and other modifications in the future(Weidner, 2005).

Since the discovery of ozone hole, ozone layer monitoring is being carried out from space and ground observations throughout the world. Space-based instruments such as SCIAMACHY (Scanning Imaging Absorption Spectrometer for Atmospheric Chartography: Bovensmann et al. (1999)), OSIRIS/Odin (Llewellyn et al., 2004; Murtagh et al., 2002) and SOLSE/LORE (Space Shuttle Ozone Limb Sounding Experiment/Limb Ozone Retrieval Experiment: McPeters et al. (2000)) have the advantage of being able to monitor changes in the atmosphere over long periods of time in different geometries. The satellites usually cover the UV and optical wavelength bands. A complementary approach is known as Differential Optical Absorption Spectrometer (DOAS) which uses payloads flown to altitudes of 20–40 km by high-altitude balloons (Ferlemann et al., 2000) with different observational geometries.

Balloon-borne instruments are a comparatively cheaper and faster method of measuring *in situ* profiles of ozone and other trace gases (Okano et al., 1996) in the upper troposphere and stratosphere. These have typically been done by electro-mechanical devices tuned for specific gases (Wolff et al., 2008). Spectroscopic observations of absorption and emission lines in the atmosphere allow simultaneous measurement of multiple gas species — including greenhouse gases — and have enhanced our knowledge of photo-chemical reactions of in the atmosphere (e.g. Kritten et al. (2010); Weidner et al. (2005)).

In this chapter, the feasibility of using an off-the-shelf spectrograph to trace the UV emission in the atmosphere is explored. The instrument setup,

calibration of the payload and the experiment method is as described in chapter 2. We obtained the variation of the scattered solar UV (UVA/UVB) flux (discussed in chapter 2), and measured the ozone slant column density (SCD) with altitude (discussed in this chapter). Although we obtained valuable data from the experiments, our team believes that a custom built spectrograph will prove more productive.

5.2 DOAS

For trace gas analysis, we used the widely accepted Differential Optical Absorption Spectroscopy (DOAS) technique. DOAS technique is one of the most useful technique for atmospheric remote sensing, developed by IUP Heidelberg (Platt et al., 1979, 1980; Platt & Perner, 1980). Optical depths of 0.0001 along light paths of 15 km can be observed with typical DOAS systems enabling the detection of weak absorbers. The DOAS technique is the application of Beer-Lambert law to the entire atmosphere in a small range of wavelengths.

The DOAS technique can be broadly divided into two categories passive DOAS and active DOAS depending on the type of light source and the method of experiment.

Active DOAS techniques employ a light source of their own as used in long path DOAS systems, cavity-enhanced DOAS systems, etc. In active DOAS systems the light from the the source is fed to the spectrograph after passing through the atmosphere whose trace gas strength is to be measured. The Spectrograph provides the spectral information and this information is analyzed to obtain trace gas strengths and composition along the light path. Active DOAS technique is usually employed for ground-based measurements because of the use of artificial light source. The sensitivity of these systems also decreases with increase in path length due to loss of light in the atmosphere. Active DOAS method is a valuable tool in obtaining tomographic

information (e.g. 2D pollution information) of local trace gas by employing several mirrors at different altitudes and, thus, several light paths (Weidner, 2005).

Passive DOAS enables measurements from moving platforms such as balloons, UAVs, satellites, etc. (Platt & Stutz, 2008), in addition to ground based measurements, as it uses a light source of extraterrestrial origin, the Sun. Passive DOAS systems can also use lunar light or light from stars as the source. Passive DOAS measurements can be direct observation of source (i.e. solar, lunar or stellar light) or scattered light from the extraterrestrial source. Direct source measurement can only measure trace gas profiles in the line of sight of the source but have the advantages of simple geometry of observation and more photons for analysis (Weidner, 2005).

Ground-based measurements cannot be carried out during cloud coverage, but in the case of balloon measurements trace gas strength from ground to the stratosphere can be retrieved during the ascent of the payload.

5.2.1 Theory

Different atmospheric species will have specific absorption features and the concentration of these species can be retrieved from analysis of broadband absorption spectra in the required spectral ranges. DOAS analysis is an extension of Beer-Lambert law which states that the intensity of light traveling through a medium will decreases exponentially with the product of the extinction coefficient and the path length (Danckaert et al., 2016). Basic equation of Beer-Lambert law is as follows

$$I(\lambda) = I_0 exp^{-L\sigma(\lambda)n} \tag{5.1}$$

where $I(\lambda)$ is the measured intensity, $I_0(\lambda)$ the unattenuated reference intensity, L is the path length in cm, $\sigma(\lambda)$ is the absorption cross sections which is dependent on wavelength, and n is the number density of the species

$[molecules/cm^3]$. The $L \cdot \sigma \cdot n$ is the dimensionless quantity known as optical depth (τ).

Rayleigh and Mie scattering also contributes in reducing the intensity in atmosphere due to extinction of light. Scattering in general can be assumed to be a broadband absorption feature. Including these scattering effects to the above equation provides

$$\tau(\lambda) = \ln \frac{I_0}{I(\lambda)} = L(\sigma(\lambda)n + \epsilon^R + \epsilon^M) \tag{5.2}$$

where ϵ^R and ϵ^M are the extinction coefficient of Rayleigh and Mie scattering respectively. DOAS method works by separating broad and narrow band spectral structures of the absorption spectra in order to extract the narrow trace gas absorption features. This is achieved using certain approximations which are as follows:

- The concept of Slant Column Densities (SCDs) is introduced assuming the absorption cross sections of species to be independent of environment parameters like temperature and pressure.
- Broadband features like scattering and reflections are approximated by a low order polynomial.
- Mean path is assumed in case of scattered light observations.
- Concept of pseudo-absorbers is used, these may include under-sampling by the instrument or ring effect.

Molecular absorption cross-sections of trace gases are fitted to the logarithm of the ratio of the measured spectrum and the reference spectrum. The reference spectrum can be an extraterrestrial spectrum or the spectrum measured at the lowest light path. The result of this fitting procedure (i.e. coefficients of fit) corresponds to the the total number of molecules per unit area along that particular light path for each trace gas, i.e., the differential SCD.

Atmospheric absorption species have high frequency components in their spectrum and DOAS analysis uses these structures for resolving optical densities of trace gas species. A least squares fitting process is used to achieve this. The result of the fit is differential slant column densities of the trace gas.

The linearity of DOAS retrieval problem breaks when we take into account the following effects

- Correction of small wavelength shifts between measured and reference spectra with shift and stretch parameters.
- Introduction of offset parameter to account for dark current or stray light issues (both instrumental and from the atmosphere).

Due to the shift, stretch and offset parameters, this is a non-linear least squares problem, which can be solved using a Marquardt-Levenberg (M-L) algorithm (see Bevington (1969); Danckaert et al. (2016); Marquardt (1963)) to obtain the SCDs. This section has given a brief overview about the DOAS procedure, for more information and detailed discussions please refer to Platt & Stutz (2008) and Danckaert et al. (2016).

5.2.2 Advantages and Disadvantages with DOAS

Advantages

- Rayleigh and Mie scattering (broadband features) can be assumed as a low order polynomial and removed easily.
- Estimation of absolute intensity (reference spectrum) is not required.
- Enables measurement of multiple species at the same time.
- Provides high sensitivity on account of long path lengths and high specificity.

Disadvantages

- Affected by atmospheric turbulence.
- Species with absorption in UV and visible are limited.
- Ground based observations are affected by cloud cover and other climate phenomenon.

5.3 Experiment

Trace gas analysis was carried out on the spectroscopic observation of UV scattered light described in chapter 3. These observations were carried out on two flights in 2014, 15th June and 12th October. The launches were carried out in the morning, when winds were relatively mild, from the Hosakote campus (13.113°N, 77.814°E) of the Indian Institute of Astrophysics near Bangalore, India. Our balloon-borne instrumental set-up consisted of three main parts: (i) a spectrograph with an optical fiber and a light collecting lens; (ii) a Raspberry Pi single board computer (SBC); (iii) an optical monitoring camera and environment sensors; and (iv) an attitude sensor described in chapter 4. All instruments were powered through a 13000 mAh lithium battery with two power settings at 5 W and 10 W. The instrument details, the experiment and its calibration are described in detail in Chapter 3, section 3.2. For trace gas analysis from scattered solar light, the light collecting lens was placed looking at the earth limb (horizontal to the payload box). The spectrograph recorded 1 sec exposure spectra in intervals of 5 seconds. Only observations taken at elevation angles of $\pm 1^{\circ}$ and at azimuth angles around 270° using attitude sensor data were considered for trace gas analysis.

5.4 Analysis

The analysis was carried out using DOASIS (Kraus et al., 2004), which is a software to analyze the data and obtain the trace gas strengths. The DOASIS technique uses a least-square fitting with cross-sections of different species and a synthetic Ring spectrum[1], generated using the DOASIS software (Kraus et al., 2004) in the wavelength band of interest to generate the differential slant column densities (dSCD) of the trace gases. A third-order polynomial was used to account for the broadband features (Rayleigh and Mie scattering).

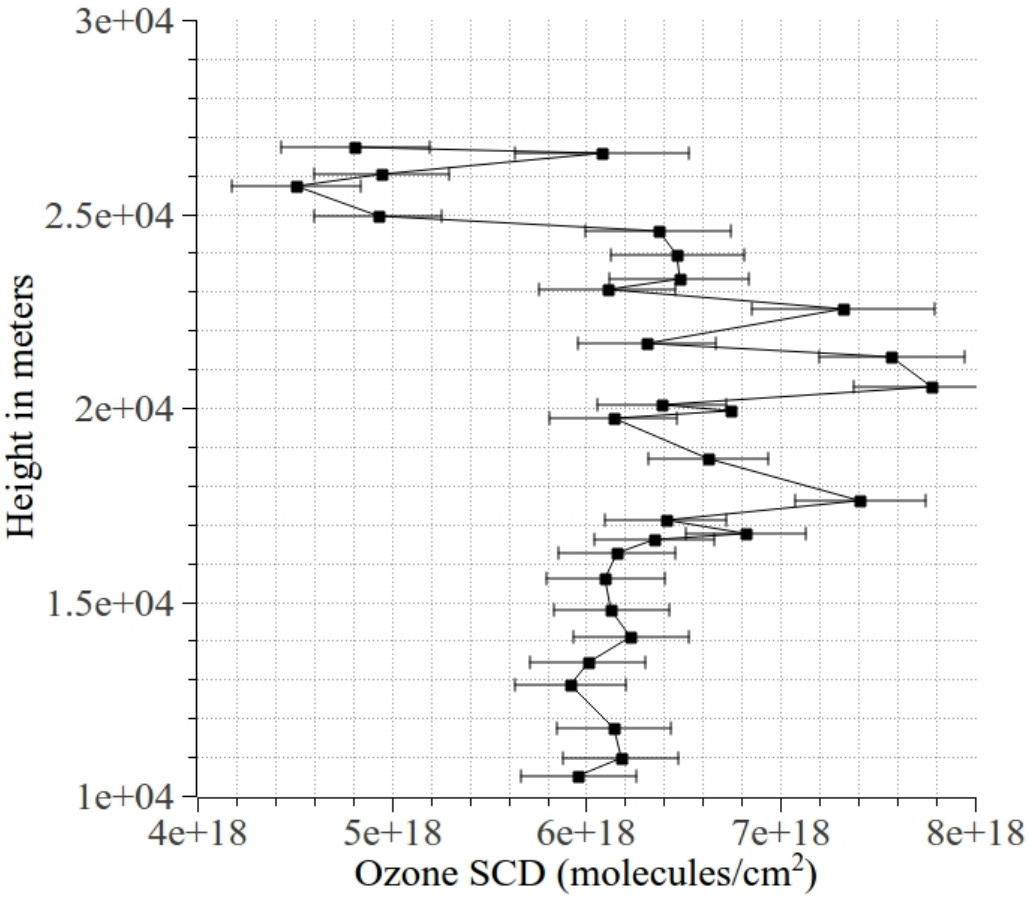

Figure 5.1: Observed ozone SCD on June 2014 Flight.

[1]To correct for the ring effect which leads to the widening of spectral features in scattered light observations, e.g. de Beek et al. (2001)

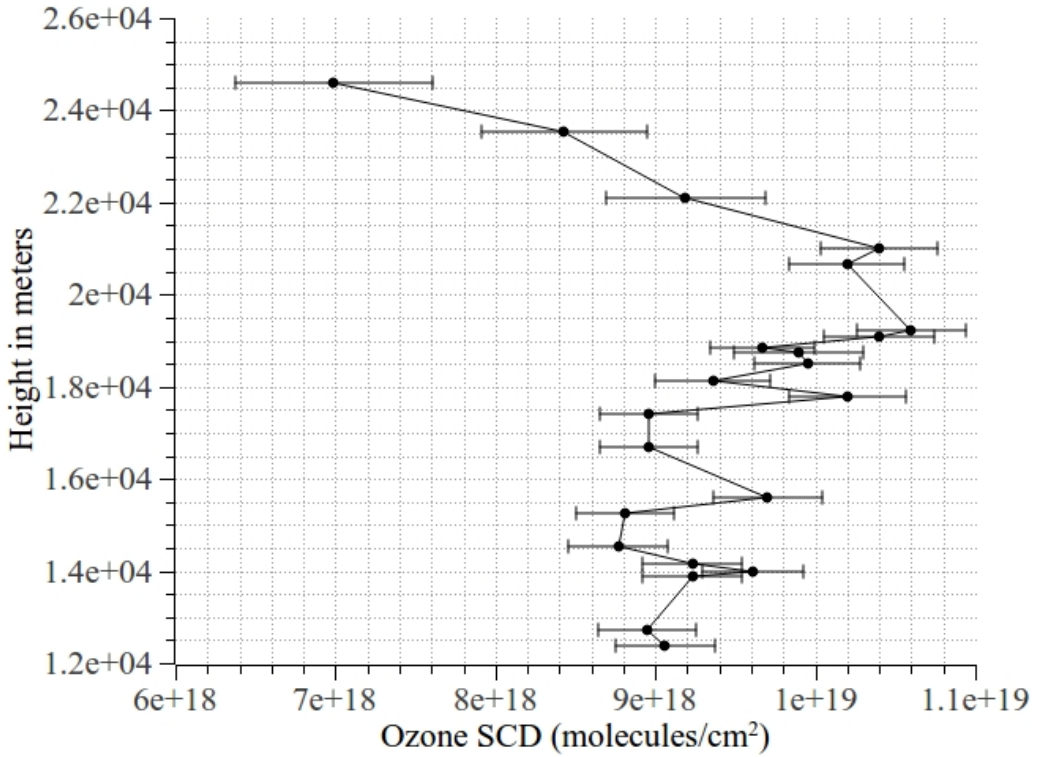

Figure 5.2: Observed ozone SCD on October 2014. Please note that the height information of this flight was calculated based on ascent rate, as GPS information was not available throughout the flight.

The observed spectra were corrected for the dark current measured on the ground before launch before the DOAS analysis. The DOAS fit was carried out in the wavelength range 305–340 nm. The following cross-sections were used: ozone from Bogumil et al. (2003) at $T = 223$ K, NO_2 from Vandaele et al. (1998) at $T = 220$ K, BrO from Wahner et al. (1988) at $T = 228$ K and O_4 at $T = 296$ K from Spectroscopy Lab of Royal Belgian Institute for Space Aeronomy (http://spectrolab.aeronomie.be/o2.htm). A Fraunhofer reference spectrum (solar spectrum (Kurucz et al., 1984) convolved with the instruments slit function), along with various trace gas absorption cross-sections and the Ring spectrum, was used for analysis. A shift-and-squeeze technique was carried out with respect to the Fraunhofer spectrum during the fitting process. The observed slant column densities for June and October 2014 are as shown in Fig: 5.1 and Fig: 5.2.

5.5 Conclusion

Here in this chapter a method to measure trace gas strengths from the limb scattered UV radiance using the balloon-borne UV spectrograph is presented. The instrument discussed here have been flown on some of our balloon flights, and is in a constant state of improvement. This method for atmospheric observations provides a system which is comparable to other existing systems in the field, and its functionality is well-documented in the previous sections. The instrument used in the experiment suffers from certain limitations that have to be corrected. For example, the current spectrograph has a low signal to noise ratio (SNR), therefore, improving the SNR will improve the sensitivity, and will even enable operations during the night time. Even though corrections have been carried out for dark signal variations with temperature and correction being incorporated it in current data analysis process, it is necessary to look into details of the temperature dependence of the slit height and other optical parameters of the current spectrograph. However, The spectrograph build in-house is described in chapter six with similar functionality but a better detector will be used in future observations.

In these flights, the payload experienced frequent oscillations preventing continuous observation for a long duration. The pointing system (Nirmal et al., 2016) described in Chapter three will enable stable observations of regions of interest. Multi-Axis DOAS (MAX-DOAS, Hönninger et al. (2004)) observations using the same instrumentation setup can be carried out using the pointing system. In addition, it will be possible to point at the Sun (or the Moon) to employ passive DOAS technique of measuring trace gas strengths, thus improving the SNR and accuracy of trace gas analysis.

The same principle and the method used for the analysis of ozone can be applied to other trace gases in the atmosphere, such as BrO, NO_2, etc. We are planning to perform DOAS analysis of BrO. For this species, Aliwell et al. (2002), on the basis of previous observations and DOAS analysis with

different fitting windows, recommended to use the narrow wavelength band of 346–359 nm. They found that even a small change in the fitting window leads to significant changes in the retrieved SCDs, and therefore, the wavelength band of 346–359 nm was recommended.

Chapter 6
Near UV Spectrograph with Photon Counting Detector

Sreejith, A. G, Safanova, M., Murthy, J., Proc. SPIE 9654, International Conference on Optics and Photonics 2015, 96540D, 2015.

6.1 Introduction

Spectroscopy can trace its origins back to *phenomenon of colors* in *Opticks* by Isaac Newton. Gustav Kirchhoff and Robert Bunsen created a spectrograph of reasonable resolution by passing a collimated beam through a prism and a focusing optics. Even though diffraction gratings were used for a long time, H. A. Rowland, of Johns Hopkins University was the first to create ruling engines capable of producing diffraction gratings with necessary precision.

Optical spectrometry have contributed immensely to the advancement of science, especially physics, in the past couple of centuries. Spectroscopy has contributed to finding out the stellar abundances (compositions of stars) as well as discovering unknown species; for example, unknown spectral lines in the solar spectrum led to the discovery of helium.

Observations from high-altitude balloon platforms provide us with an op-

portunity to detect radiation in the near ultraviolet (NUV). As discussed in previous chapters we observe from altitudes of greater than 25 km which puts the payload above most of the atmospheric absorption (primarily O_3 and O_2) allowing us to observe to a short wavelength cutoff of 270 nm. As Rayleigh scattering is absent at these altitudes the seeing is also improved throughout the NUV. The upper atmosphere is also more uniform, making corrections for turbulences more precise than those at lower altitudes (Arnold et al., 2013).

Our group intends to utilize this opportunity by using compact instruments to do atmospheric and astronomical observations. The first scientific objective is the the observation of atmospheric emission and absorption features. Trace gas analysis is carried out from scattered/direct solar light observations as discussed in the previous chapter. Other observations include the observation of solar system objects such as comets, where we would be able to observe molecular lines from water, CO, and other species.

This chapter discusses the design and development of a spectrograph to observe in NUV from atmospheric and astronomical sources. The design of choice is a Czerny-Turner (C-T) spectrograph which has been used extensively in both its classical and modified forms [eg. Ref: (Wang et al., 2008),(Si et al., 2008),(Chandler, 1968),(Rouse et al., 1969)], including in balloon payloads [eg: Ref: (Murcary et al., 1969), (Lemaire, 1971)]. In the following sections, a spectrograph capable of operating in the wavelength 250-400 nm which can be connected to any telescope is described. The system is designed considering aberration correction dependence with wavelength. Different aberration correction methods are available in literature, some of which are applied are discussed in the next section and are compared with the existing classical arrangement.

6.2 Design

The design of the spectrograph is a modified Czerny-Turner. Crossed Czerny-Turner is more compact than our current design but was avoided in order to reduce scattering and stray light effects The Czerny-Turner spectrograph is a two mirror system where light from the entrance slit is collimated by a concave spherical mirror onto a plane grating. The light diffracted by the grating (600 lines/mm) is focused onto the imaging plane by another mirror (Czerny & Turner, 1930). We have used off-the-shelf mirrors and gratings for this spectrograph and an image-intensified CMOS detector is the detector.The details of the detector are in Table: 6.1 with further description of the spectrograph in the following sections.

Table 6.1: Detector specifications

Sensor Type	Intensified CMOS
Image intensifier	Micro Channel Plate MCP40 from Photek
MCP Type	Z stack MCP with 40mm diameter
Photo cathode	S20(Multi alkali)
Phosphor screen	P46
Optical Format	1/4”
Active Array Size	1280x800(HxV)
Pixel Size	3 μm x 3 μm
Frame Rate	30 fps @ 1280 x 800
Input window size	40mm
Readout system	Spartan 6 FPGA
Output Data Format	16 bit Serial(for continuous mode) 5 bytes/photon event(for photon counting mode)
Power Consumption	$\approx$ 5 Watts
Weight	700 gms

6.2.1 Method of Aberration Correction

A concave spherical mirror when used off-axis has spherical aberration, coma, astigmatism, field curvature, and distortion. In most of the cases the first three aberrations are important and should be corrected. Spherical aberration is reduced by following the method in Xue et al. (2009). The F-number of the system is represented as $\mathrm{F\#} = f/D$ where D represent the diameter of the mirror and f the focal length. The wavefront aberration W_s due to spherical aberrations can be expressed as

$$W_{s_{(max)}} = \frac{(y_{max})^4}{8r^3} \tag{6.1}$$

$$\frac{(y_{max})^4}{8r^3} \leq \frac{\lambda}{4} \tag{6.2}$$

where r is the radius of curvature of the spherical mirror, and y_{max} is the half aperture of the spherical mirror. Solving for the above equations we determine the focal length and diameter of the mirror to be used. The radius of curvature r is twice the focal length for a spherical mirror. Hence Equation (6.2) can be modified as follows

$$f \leq 256 \cdot \lambda \cdot (F\#)^4 \tag{6.3}$$

$$D \leq 256 \cdot \lambda \cdot (F\#)^3 \tag{6.4}$$

Thus the relative aperture of the system can be calculated considering the aberration tolerance, incident light power, .etc.

The use of off-axis collimating and focusing mirrors leads to coma in a Czerny-Turner system. Coma aberrations are corrected using Shafer equation (Shafer et al., 1964).

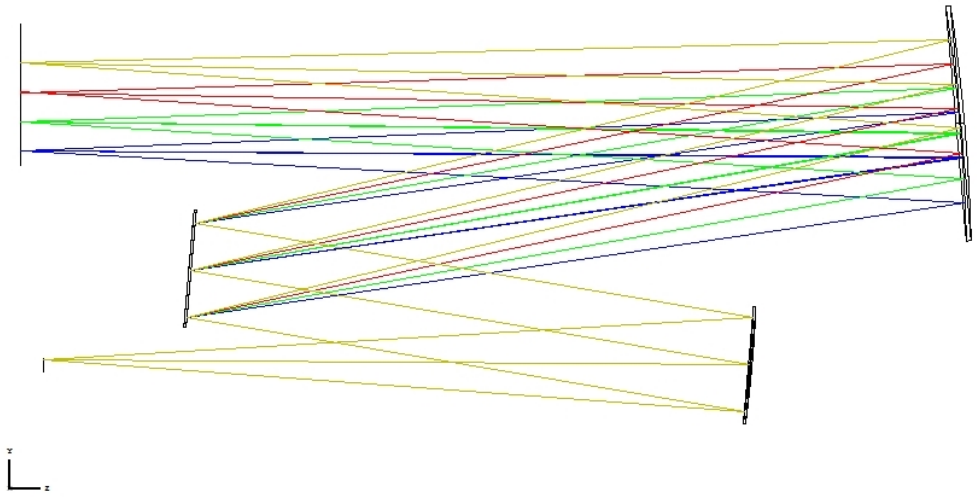

Figure 6.1: Uncorrected Czerny-Turner spectrograph design.

$$\frac{\sin\alpha_1}{\sin\alpha_2} = \frac{r_1^2(\cos\theta\cos\alpha_1)^3}{r_2^2(\cos i\cos\alpha_2)^3} \tag{6.5}$$

where α_1 and α_2 are the off-axis incidence angles for the collimating and focusing mirror. the incidence and diffraction i and θ are angles on the plane grating. The curvature of the collimating and focusing mirrors are r_1 and r_2 respectively.Typical values of α_1 and α_2 are approximately equal to 5 and 8 and hence $\cos\alpha_1^3 \approx \cos\alpha_2^3 \approx 1$. Therefore equation 3 modifies as

$$\frac{\sin\alpha_1}{\sin\alpha_2} = \left\{\frac{r_1}{r_2}\right\}^2 \cdot \left\{\frac{\cos\theta}{\cos i}\right\}^3 \tag{6.6}$$

Adjusting r_1, r_2, α_1 and α_2 of the mirrors one can reduce coma. Czerny-Turner system geometry of placing the focusing mirror is limited and hence to fit the geometry the additional condition of $r_1 < r_2$ was included. The values of θ and i are further calculated from grating equation

$$d(\sin i + \sin\theta) = m\lambda \tag{6.7}$$

where d is the grating order represented in lines/unit length and m is the order of diffraction.

Astigmatism extends the image along the slit height (sagittal direction) due to the difference in sagittal and tangential focal length of the mirrors caused by off-axis reflections. Reasons why astigmatism should be reduced in a spectrograph, such as the increase in the exposure time and reduction in the resolution of the system, are widely discussed in literature (Dalton, 1966). Two different methods for astigmatism correction was carried out as astigmatism is the main contributor of aberration in a Czerny-Turner system.

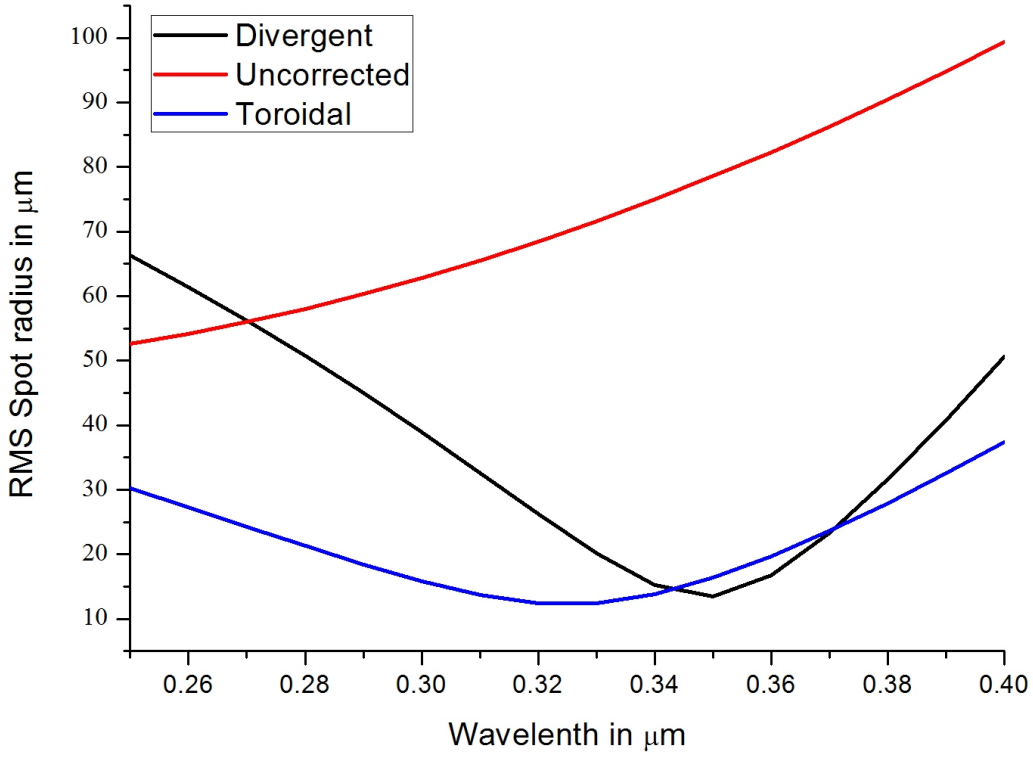

Figure 6.2: RMS spot radius for various configurations

1.Divergent illumination: Eliminating astigmatism by divergent illumination of the grating in a Czerny-Turner spectrograph is discussed in (Bates et al., 1970) and (Austin et al., 2009). Here the distance from the entrance slit to the collimating mirror is reduced so that the grating is under divergent illumination (Bates et al., 1970). This method makes use of diffraction in

the tangential plane which, when reflected from the grating introduces astigmatism (that is wavelength dependent) which compensates for the off axis reflection of spherical mirrors. The advantage of this method is that it does not require any extra optics for correction of aberrations.

2.Toroidal mirror: Astigmatism can be corrected by using a toroidal mirror (which has distinct tangential and sagittal focal lengths) as first discussed by Shafer (Shafer, 1967) and this method has been widely used by many authors while modifying Czerny-Turner spectrograph. The focal distance to the tangential image for a collimated beam reflected from a spherical surface is given as (Shafer, 1967)

$$f_t = \frac{r\cos\alpha}{2} + \Delta f_t \tag{6.8}$$

and the distance to the sagittal image is

$$f_s = \frac{\rho\sec\alpha}{2} + \Delta f_s \tag{6.9}$$

where $f_{t,s}$ corresponds to the distance measured along the principal ray from the image plane to the surface of the mirror. α is the off-axis angle. Δf terms are the third order approximations. r and ρ are the radii of curvature of the mirror in the tangential and sagittal planes. Assuming that the Δf terms are almost equal we have

$$\rho = r(\cos^2\alpha) \tag{6.10}$$

These equations will define the radius in terms of the off-axis angle for the toroidal mirrors required. A mirror with a shorter sagittal focal length as compared with tangential focal length will help to correct astigmatism in these systems.

6.2.2 Ray Tracing and Analysis

The ray tracing of the spectrograph is carried out using the optical system design software ZEMAX[1]. The grating used is a 600 lines/mm plane grating. The spectrograph is an NUV (250-400 nm) system. The optical system layout for the spectrograph without astigmatism correction is shown in Fig. 6.1. The spot radius for different wavelengths are obtained after the initial optimization of the spectrograph to correct for coma and spherical aberration. The spot radius thus obtained is compared with the spot radius of a modified Czerny-Turner spectrograph where corrections using Divergent illumination method and Toroidal mirror method are carried out. A toroidal mirror with the same radius of curvature as the spherical mirror was used to reduce astigmatism. The variation in the spot radius with wavelength for different systems is as shown in Fig. 6.2. It is clear from Fig. 6.2 that both modifications on the Czerny-Turner system improve the optical performance (reducing aberrations). A toroidal mirror improves the performance throughout the wavelength range, but at the cost of the addition of an extra optical component as compared to classical a Czerny-Turner system. The divergent illumination method improves the performance but mostly at higher wavelengths. The spot radius of the central wavelength reduces from around $68\mu m$ to around $28\mu m$ in divergent illumination method and around $12\mu m$ by using a toroidal mirror.

6.3 Hardware Implementation

Once the near ultraviolet spectrograph has been designed with off the shelf components and further improved by various methods of aberration correction it was found to produce satisfactory results for aberration correction. The structural diagram of the spectrograph is as shown in Fig. 6.3. The

[1]Zemax is a trademark of Zemax, LLC

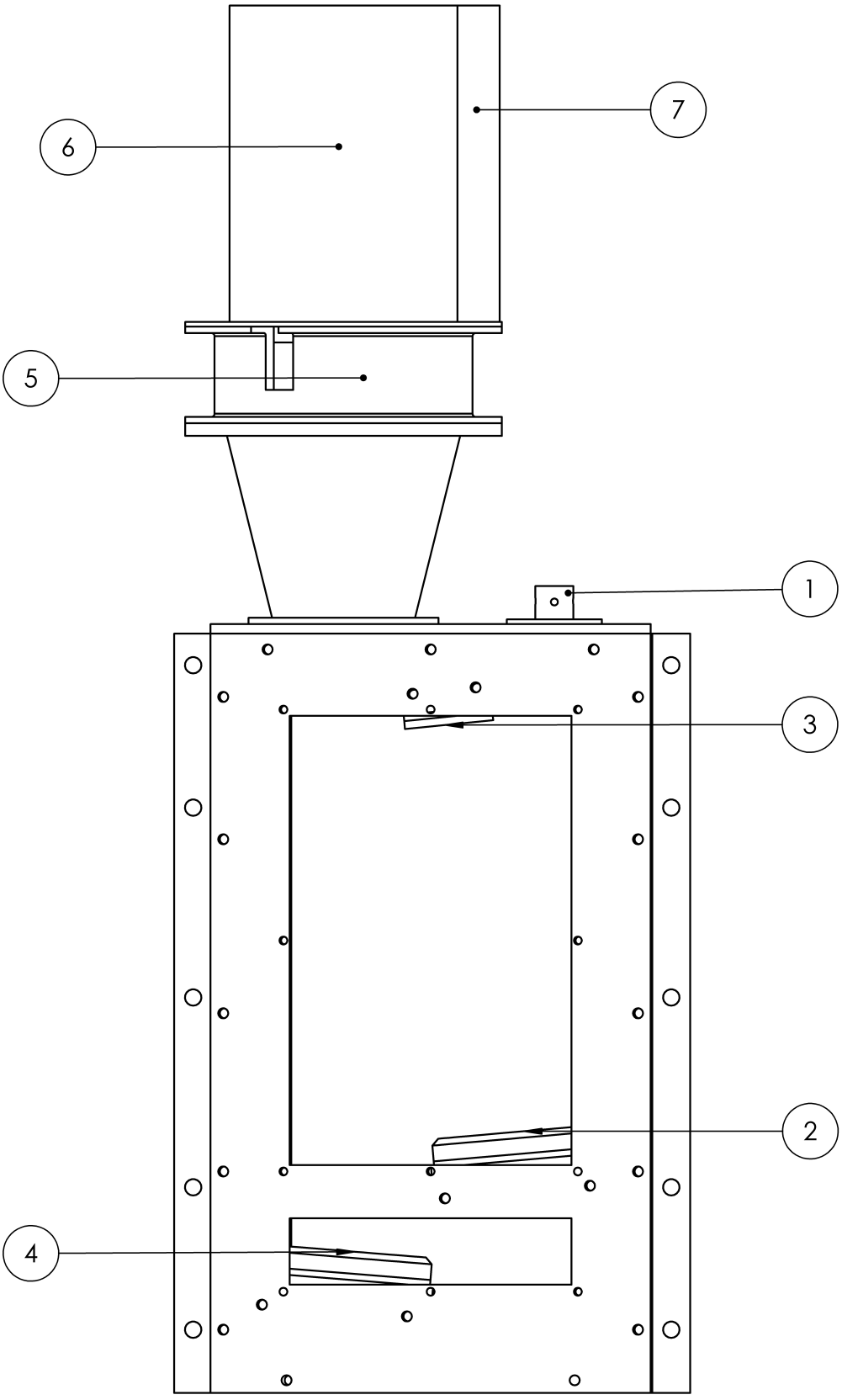

Figure 6.3: Structural design of the spectrograph. The component of spectrograph are as follows: *i.* Optics fiber adapter, *ii.* Collimating mirror, *iii.* Grating, iv. Focusing mirror, *v.* MCP, *vi.* Relay lens and CMOS detector, *vii.* Power supply (HVPS & LVPS).

photograph of the assembled spectrograph is as shown in Fig. 6.4.

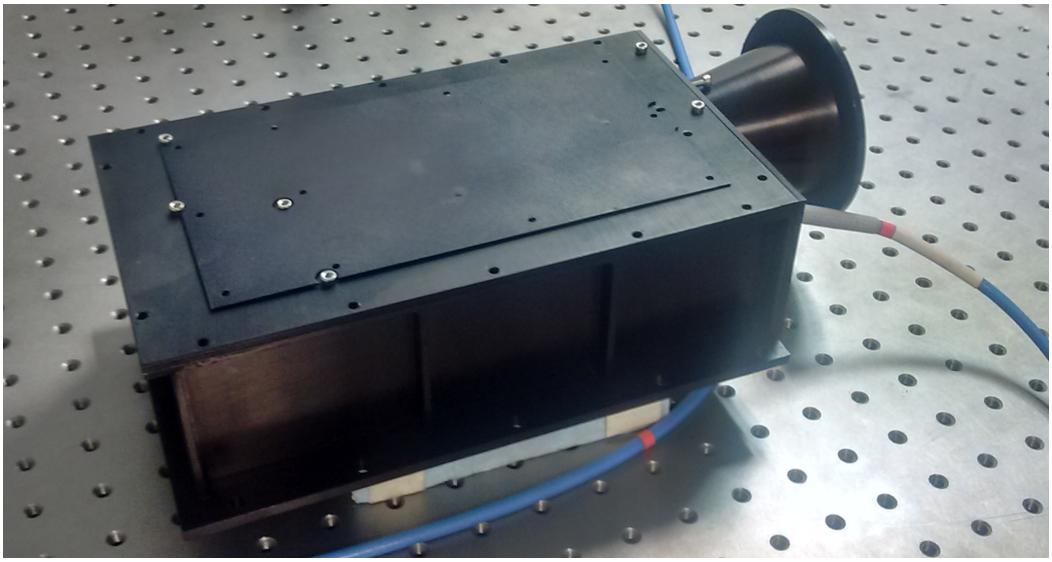

Figure 6.4: Assembled spectrograph in the laboratory (Detector part is not included in this image).

6.3.1 Opto-mechanical Overview

Light to the spectrograph is coupled using a 400μm fiber. The fiber aperture acts as the entrance slit of the spectrograph. The spectrograph has identical 2-inch concave mirrors as the collimating and focusing mirrors. The light from the fiber is used to illuminate the grating (600 lines/mm) in divergence mode. The reflected light from the grating is focused on to the detector using the focusing mirror. The size and focal length of mirrors are selected to reduce aberrations as discussed in the previous section. Mounts for all the optical components are made in Aluminum and anodized to reduce scattering. The entire mechanical breakout diagram is as shown in Fig. 6.5.

6.3.2 Detector Overview

The detector of choice for the spectrograph is an intensified CMOS consisting of a Micro Channel Plate (MCP) with the associated electronics including

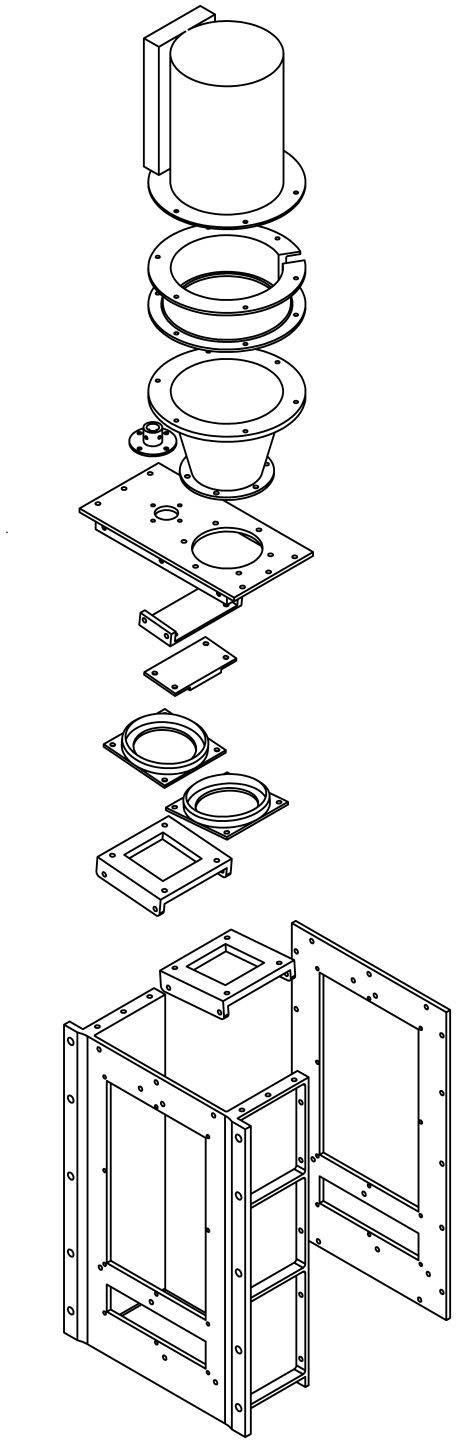

Figure 6.5: Mechanical breakout diagram of the spectrograph.

high voltage power supply (HVPS), a relay lens system, CMOS sensor and a digital readout card using an FPGA. The different sections of the detector are descried in brief below with detailed discussions in Ambily et al. (2017)

6.3.2.1 Image intensifier

We are using MCP340 assembly from Photek[2], which is a 40 mm diameter 3-stage MCP. It includes a quartz input window, S-20 photocathode, Z-stacked MCP and a P46 phosphor screen. The MCP requires an HVPS to operate in a single-photon mode, for which we have used FP632, a micro HVPS from Photek. The MCP voltage levels are $-200, 0, 2300$ and 6600 for the cathode, MCP-In, MCP-Out and phosphor screen respectively. It is possible to adjust the gain of the MCP by changing the voltage at the MCP output which automatically adjusts the screen voltage, thus maintaining a constant MCP-out-Anode voltage difference. The resulting bunch of photons from the phosphor screen at 530 nm falls on the CMOS sensor surface through a relay lens.

6.3.2.2 Relay optics

The detector currently uses the TVF-3.6X2812IR-BCDN-MD, a board-level varifocal lens from Senko with high precision zoom and focus adjustment which was provided with the CMOS board. The lens system has an F-ratio of F1:2 with an adjustable focus from 3 mm to 10 mm.

6.3.2.3 CMOS sensor

We have chosen the OV9715, a 1 Mega Pixel Video Image Sensor from OmniVision Technologies[3], for the CMOS camera. The advantages of CMOS sensors in easier readout and circuit integration, as well as their low power requirements, make them an obvious choice over the CCDs in our application.

[2] `http://www.photek.com/`
[3] `http://www.ovt.com/`

It is a 1/4 inch sensor that provides full-frame, sub-sampled or windowed 8-bit/10-bit images in RAW RGB format via the digital video port and with complete user control over image quality, formatting and output data transfer. The OV9715 incorporates advanced image processing functions, including exposure control, gain control, white balance, lens correction, and defective pixel correction, programmable through the serial camera control bus (SCCB) interface.

We are using a off-the-shelf headboard (Soliton Technologies, Bangalore) which incorporates essential components for biasing and clocking the CMOS sensor. This enables us to use the basic power, clock and synchronization signals to read the digital image values. There is a synchronous serial port for camera control which can be optionally connected to the FPGA board.

6.3.2.4 Data acquisition board

For the design of the main processor, we have chosen an FPGA prototyping board, XuLA2-LX25 from XESS Corp.[4], and added further components and modules as per our requirements. The heart of the processor is a Spartan 6 series XC6LX25 FPGA from Xilinx, Inc[5]. The FPGA is designed and programmed in such a way that it can serve the multiple functions such as control and readout of the CMOS sensor, processing and computation of centroids, and storage and transmission of the output. The inherent advantages of FPGAs, such as highly customizable architecture, the ability to do parallel processing, faster lead times, and lower costs have helped us in making changes in the algorithms without major modification of the overall system architecture.

The programming of the FPGA modules is done primarily in Verilog Hardware Description Language using the Xilinx ISE software provided by the company. In addition, we have used the VHDL modules, provided by

[4] http://www.xess.com/shop/product/xula2-lx25/
[5] http://www.xilinx.com/

the XESS Corp., for interfacing the standard IPs on the FPGA board like SDRAM (synchronous dynamic random-access memory) and SD Card.

6.3.3 Electrical Overview

The auxiliary electronics for the spectrograph include Low voltage power supply (LVPS) for CMOS and FPGA control and a High voltage power supply (HVPS) for the MCP. The simplified block diagram for the spectrograph support electronics is as shown in Fig. 6.6.

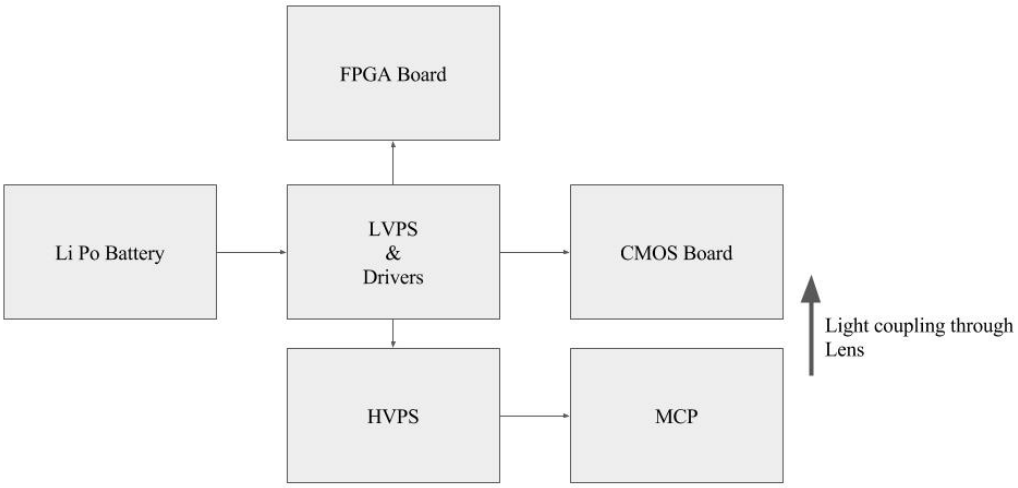

Figure 6.6: Simplified electrical block diagram of the spectrograph.

LVPS consists of regulators to provide +5V DC for the CMOS sensor and for the FPGA board. The input to the regulators comes from +7.4 V lithium polymer batteries. The capacity of the batteries depends on the duration of the experiment. FP632 micro-HVPS from Photek is used to power the MCP. and the regulated +5V is provided to FP632 micro-HVPS from the lithium polymer battery.

6.4 Ground Calibration

The calibration of the instrument was performed in class 1000 clean room at M.G.K Menon space laboratory of Indian Institute of Astrophysics.

6.4.1 Dark Count

The dark count test was performed by covering the input to the detector window and reading the image of the MCP surface on the CMOS in photon counting mode. At room temperature, a dark count of approximately 1000 cps across the entire detector was observed which is expected of an S20 photocathode. The dark count frame is shown in Fig. 6.7.

6.4.2 Wavelength Calibration

Wavelength calibration of the spectrograph was carried out at room temperature in the laboratory. A Mercury-Argon (Hg-Ar) lamp with known emission lines was used for the same. This calibration was further verified with a monochromator setup to verify the position of different wavelengths on the detector. Andor Shamrock 303i monochromator was used for the same. It is f#4 system with a wavelength resolution of 1Å. The monochromator has adjustable input and exit slit widths, which enables PSF measurements of the spectrograph. The relative effective area can also be measured with the help of this monochromator. The detailed description of ground calibration and other features of the spectrograph are beyond the scope of this thesis and will be discussed in forthcoming papers from our group.

6.5 Conclusion

The near ultraviolet spectrograph for balloon observations is described above. The instrument will have its fist flight in 2017. This spectrograph has better

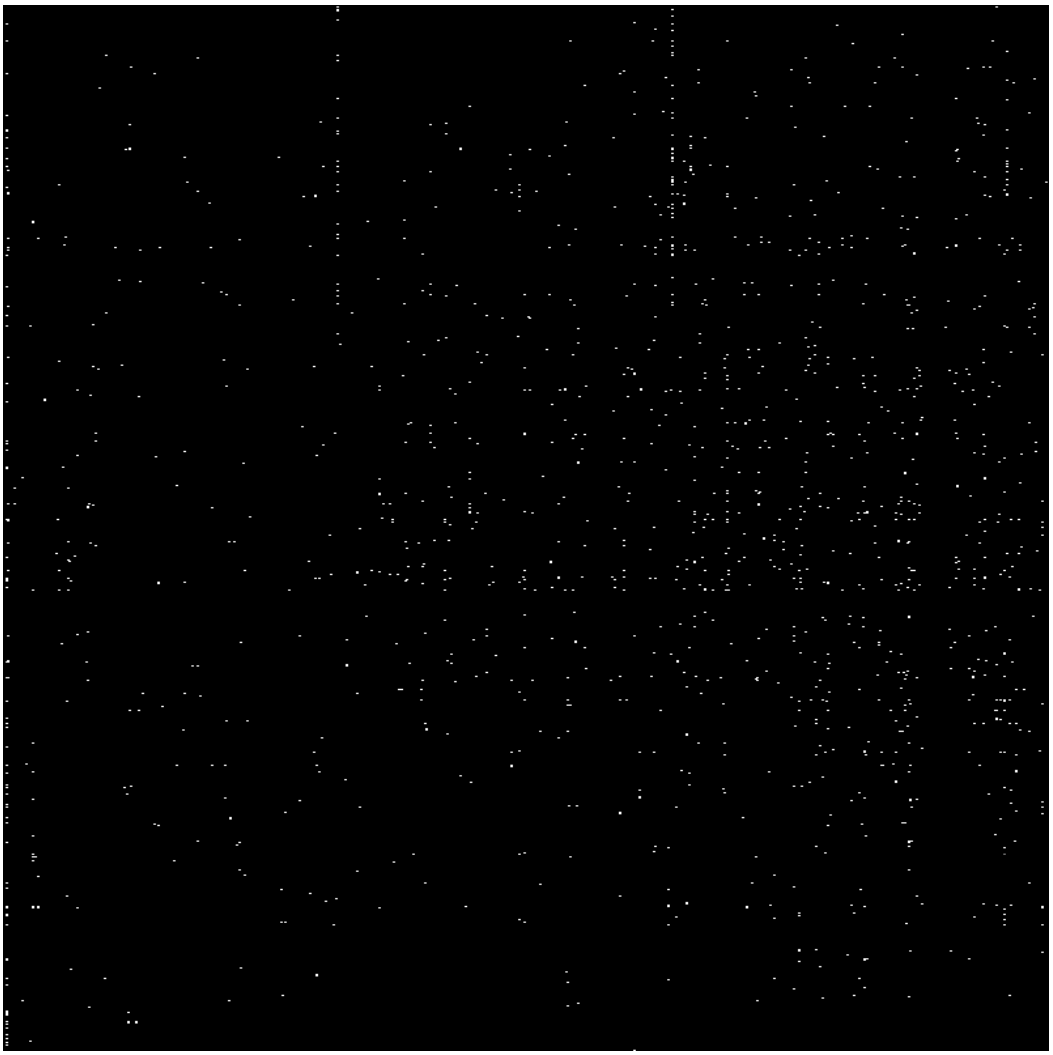

Figure 6.7: Dark frame of the spectrograph for an exposure of 2 seconds.

noise perfomance than the off th shelf spectrograph used our team for our team for observations in the past. Further improvements can be made to the instrument design after the initial flight tests of the current design. Although the divergent illumination method provides improvement without the addition of any new optical element and was hence used in this spectrograph, but its effect over a wide wavelength range has to studied further. Another method of aberration correction is using cylindrical lens and we will try to adopt it in future versions of the instrument.

Chapter 7
Far UV Airglow Observations with FUSE

7.1 Introduction

Airglow can be described as a faint emission of fluorescence from the atmosphere. It is caused by selective absorption and re-emission of solar radiation by molecules and atoms in the earth's atmosphere. Understanding this emission feature will provide valuable information about the state of the earth's upper atmosphere. Airglow predominately arises in the mesosphere and thermosphere region of our atmosphere (50 to 300 km from earth's surface). Above 300 km, the airglow arises in the geocorona and is due to the resonant scattering of sunlight from atoms. The important differentiating factor with respect to the commonly observed aurora is that airglow does not have the arc-like structures and is usually emitted from all directions of the sky (Reference: https://www.britannica.com/science/airglow). They are also emitted at all latitudes and at all times, even though the strength may vary with location and time (Meier, 1991). The airglow spectrum during daytime is termed dayglow and provides information about the composition and

processes in the ionosphere and thermosphere. During night, nightglow radiations occur by release of stored energy through photochemical reactions or recombination of ionized atoms and molecules. The strength of nightglow is very week in visible wavelengths but has stronger emissions in infrared (about 1000 times stronger). The ultraviolet nightglow emissions cannot be observed from ground and are studied with the help of rocket experiments and satellite data.

Airglow produced during the day and twilight can be attributed to scattering of the light from the sun by molecules in upper atmosphere. Atoms and molecules in upper atmosphere are also affected by radiations from outer space (for example: cosmic rays can interact with atoms and molecules in ionosphere). These reactions can lead to airglow during both day and night in the upper atmosphere.

Airglow features in the Earth's atmosphere are strongly related to time of the day and height from sea level at which these are observed. Solar activity also plays a major role in the strength of airglow (Meier, 1991). The composite airglow spectrum for day and night are as shown in Fig: 7.1 and Fig: 7.2. Meier (1991) provides a great overview on the subject of airglow emissions in the ultraviolet.

Airglow lines are one of the most important parameters to be taken into consideration while measuring the diffuse UV radiation or UV observations of point sources and extended sources from satellites above the atmosphere. Some of the brightest airglow lines are the Lyman series lines (Lyα, Lyβ, Lyγ) seen upto the Lyman limit at 912Å . Ionized Oxygen and Nitrogen oxides lines also appear as an important feature in airglow spectrum in UV range.

For astronomical observatories in the ultraviolet wavelengths from low earth orbits, it is necessary to understand the wide range of airglow emissions whose effect is a major concern during the observations. Murthy (2014) has characterized the ultraviolet foreground using observations from GALEX. The foreground mainly comprises of zodiacal light and airglow emissions. The

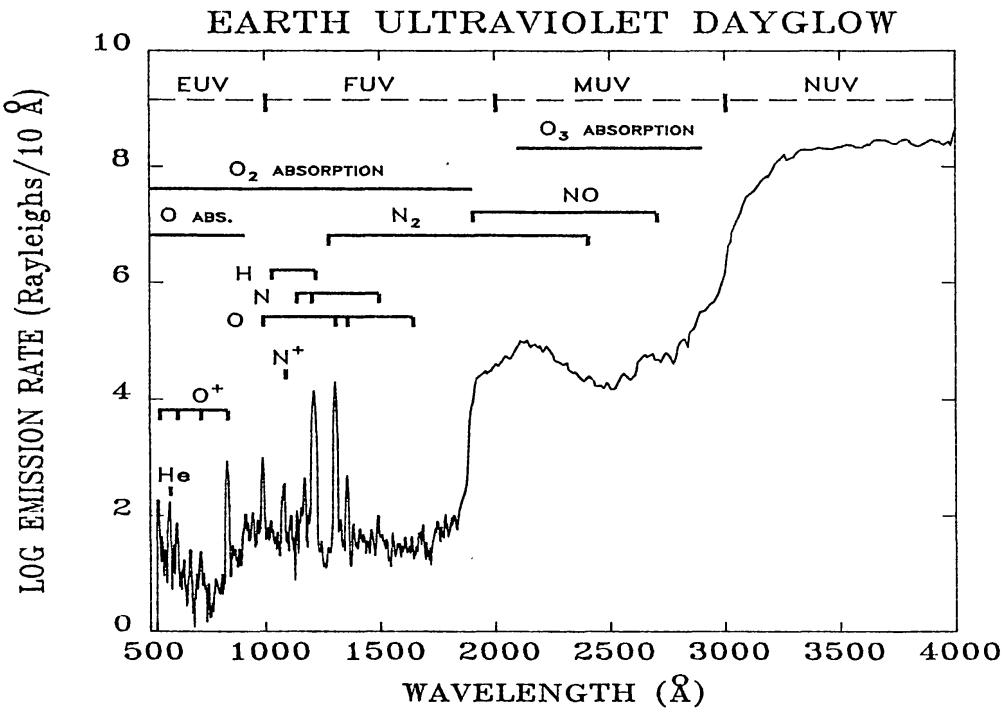

Figure 7.1: Complete dayglow spectrum adjusted to nadir viewing at 200km, *Courtsey: Meier (1991)*

zodiacal light has been well studied and is available in Leinert et al. (1998). Murthy (2014) concluded from GALEX observations that the airglow has two components: a local time dependent component which is symmetrical w.r.t. the local midnight and another component which has dependence on the sun angle of the target. But it is necessary to look into spectroscopic observations to further fix the limits on the strengths of these airglow emissions in the context of astronomical observations.

7.2 Far Ultraviolet Spectroscopic Explorer

The Far Ultraviolet Spectroscopic Explorer (FUSE) was a space telescope launched by NASA and operated by Johns Hopkins University Applied Physics Laboratory. Launched into a nearly circular, low-Earth orbit which is inclined to the equator at an angle of 25° with the help of a Delta II rocket in 1999,

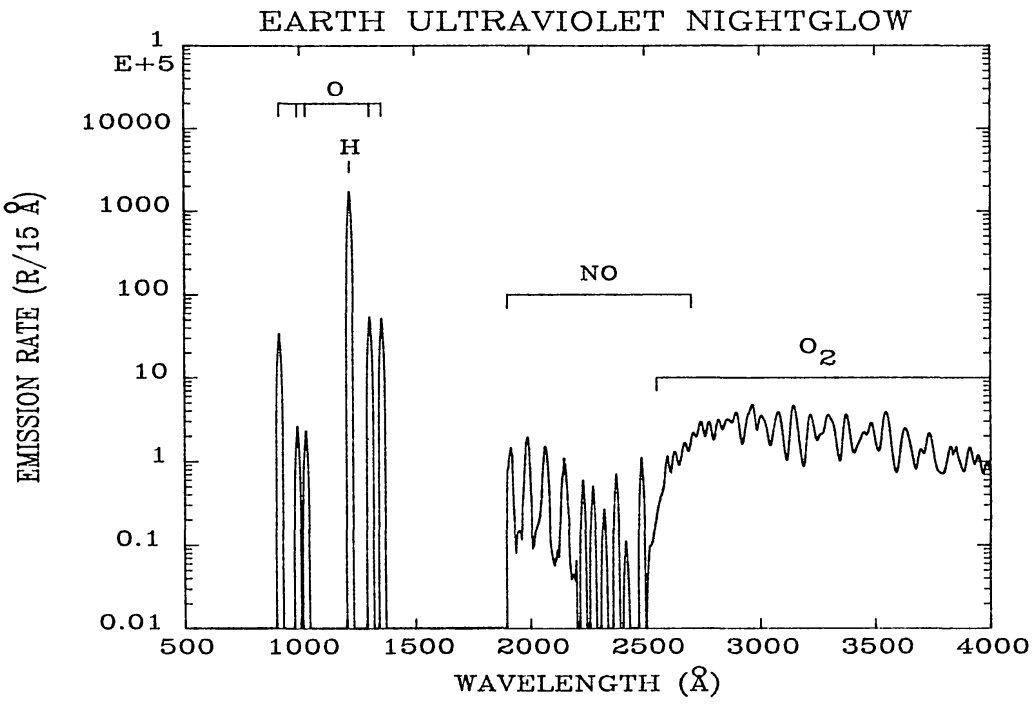

Figure 7.2: Composit nightglow spectrum adjusted to nadir viewing at 600km in equatorial region, *Courtesy: Meier (1991)*

.

FUSE was planned to be in operation for three years but worked for almost eight years. It was terminated in October, 2007 because of the failure of a reaction wheel required for pointing. Moos et al. (2000) and Sahnow et al. (2000) describe the mission and the instrument in detail. The FUSE data is available at the Mikulski Archive for Space Telescopes (MAST). FUSE operated in the spectral range of 905 to 1187Å and with resolving powers upto 20,000. Primary mission of FUSE was to characterize deuterium in understanding different stellar processes from big bang (Moos et al., 2000) .

7.2.1 FUSE Instrument

The FUSE Instrument (Fig:7.3) consists of four separate co-aligned telescopes. Each of the four channel consisted of

- Off-axis primary mirror

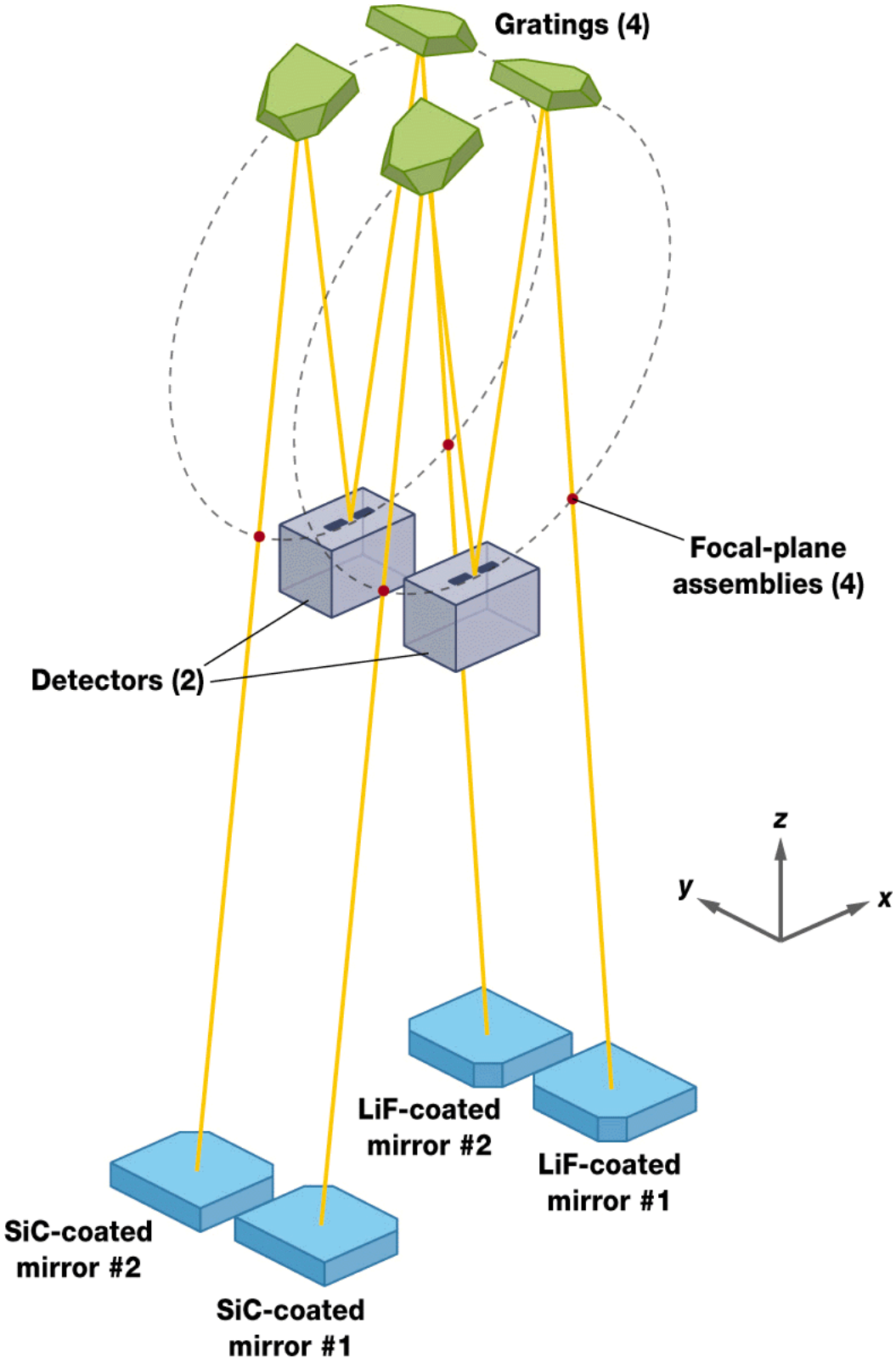

Figure 7.3: Optical design of the FUSE instrument showing the mirrors, focal plane assembly(FPA), gratings and detectors. The track of the light is from mirror to the rowland grating through the FPA and then reflects to the detector. (Image credit: https://archive.stsci.edu/fuse/papers/spie3/spie3.html)

- The focal plane assembly (FPA)
- Holographically ruled diffraction grating
- A portion of the detector.

The off-axis parabolic primary mirror collects the incoming light and feeds it to the corresponding spectrograph. The spectrographs are constructed in Rowland circle design and use holographically ruled gratings. The four channels of the instrument are co-aligned. Out of the four channels, all the elements (mirrors, gratings, etc) of two channels are coated with silicon carbide (SiC), while the other two are coated with lithium fluoride (LiF). The base layer for all the optical reflecting surfaces is aluminum. The four channels cover the entire 290Å wavelength range of the instrument (905-1187Å). The detector of choice to image the spectra from four channels were microchannel plate (MCP) detectors in photon counting mode. Detectors were also divided into two functionally independent segments A and B and these segments were separated by a small gap. A slight offset was also provided to ensure that the same wavelength region does not fall on both detectors. This configuration provided the required effective area. One detector had a set of spectrum from both of the channels.

The instrument consists of three spectrographs of different resolution and aperture separated spatially. The entrance apertures of three spectrographs are at the prime focus of the off-axis primary mirror. The spectrographs apertures are the low-resolution aperture (LWRS) of 30" × 30", a medium-resolution aperture (MDRS) 4" × 20" and the high-resolution aperture (HIRS) 1".25 ×20". MDRS and HIRS were not used to its full potential during the mission due to alignment and thermal issues, because of this most of the observations available with FUSE are through LWRS. A detailed discussion of FUSE instrument is present in the FUSE instrument handbook (https://archive.stsci.edu/fuse/ih.html).

7.3 Data

Airglow observations discussed here are from several time-tagged observations between 14 August 1999 and 27 March 2000. The observations are of different exposures and look directions. Most of the observations are of azimuths of zero or 180, so that the FUSE telescope FOV is always away from the sun. The elevation had variation from -60° to $+60^{\circ}$ degrees. Direct nadir observations were prohibited because of the limitations in telescope FoV and spacecraft orbital velocity vector (Feldman et al., 2001). The observations used for the analysis were downloaded from MAST archive of STScI (Space Telescope Science Institute). The FUSE detectors were photon counting in nature, but due to memory considerations the data from the detectors were stored in two separate formats. A 32-bit word contained the X coordinate (14 bits) and the Y coordinate (10 bits) of the detector, 5 bits for the pulse height distribution, one bit each for the segment and the detector, and a flag bit identifying a positive photon event. This photon information was converted into a photon list (TTAG mode) for lower count rates or 2-D histogram (HIST mode) for observations of higher count rates. Sahnow et al. (2000) observed calibration problem over longer wavelengths due to the occultation of starlight by a wire close to tangential focus, leading to low count values. The data used in the analysis were obtained from detector 1 as the high voltage power supply of detector 2 was turned off during these observations.

LWRS aperture observations were used for airglow analysis. The LWRS aperture was separated from the other two apertures (HIRS and MDRS) by 105" and 210", respectively. The data reduction was carried out using the data pipeline software, CalFUSE v3.2 (Dixon et al., 2007). Feldman et al. (2001) created an atlas of airglow emissions from illuminated earth FUSE observations and it has been used extensively as the reference for the work described in this chapter.

The brightness of airglow lines is represented as unit of Rayleigh. One

Rayleigh corresponds to a column emission rate of 10 photons per square meter per column per second, i.e.,

$$1\ Rayleigh = \frac{10^6}{4\pi}\ photons\ s^{-1}\ cm^{-2}\ sr^{-1} \tag{7.1}$$

7.4 Data Analysis

The data is extracted from the *fraw.fit file. The raw file name contains information regarding the detector, channel, and the mode of data readout. These data files contain unprocessed raw science data. The data stored in the raw TTAG files are photon list information containing the time information and position of photon arrival on the detector in X & Y. Information of the exposure time is stored in the header keyword EXPSTART. The time resolution is usually 1 second. From the raw fits files the particular region of interest, for example (x values: 6602–6838, y values: 460–614) corresponds to LWRS of LiF1 channel at wavelength of 1025.72Å, is extracted to get the count rate for a particular observation. This is carried out using *plotrate.pro* IDL function available in CalFUSE pipeline. The background calculation of the standard CalFUSE pipeline was found to overestimate the instrument background (Murthy & Sahnow, 2004), and so the background was empirically calculated from the region on the detector close to the desired aperture.

*fidf.fit is an intermediate file which is one of the outputs of the CalFUSE pipeline. The information regarding the satellite including the latitude, longitude, earth limb angle, time since sunrise, etc. are obtained from this file. The look direction information of Azimuth and elevation is calculated from the right ascension and declination information of target, latitude and longitude information of spacecraft, and time information of the observation.

From the raw file and the intermediate file, the count rate for a particular airglow line for a fixed azimuth and elevation is obtained as a function of time. The time resolution of these derived data is one second.

A sample spectrum obtained from airglow observations of the LWRS channel is as shown in Fig. 7.4. The strongest line close to the center is a combination of Lyman β and OI4. This observation was a bright earth observation obtained on 27 March 2000. The spectra is summed up from 9 exposures totaling up to 12512 seconds.

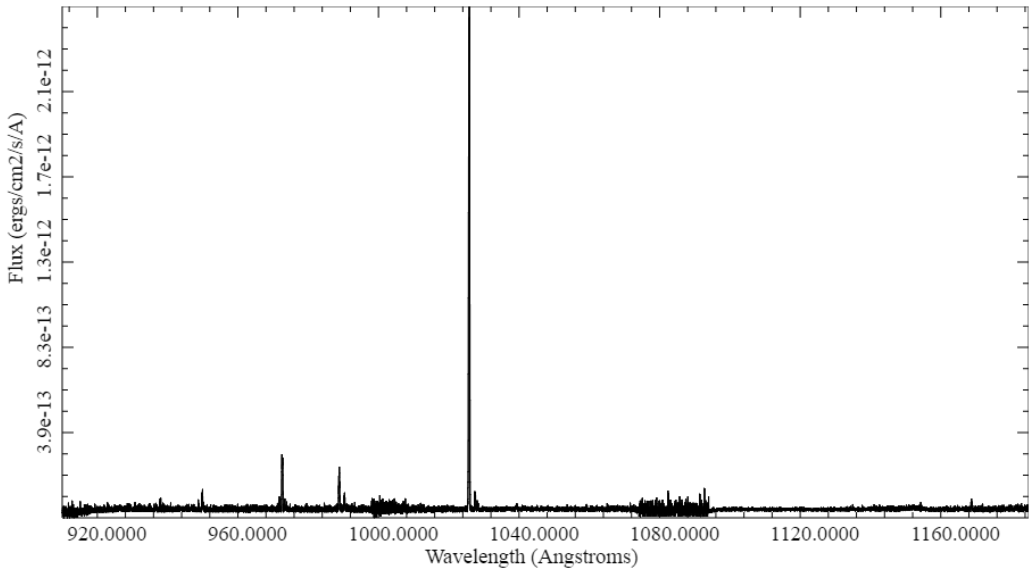

Figure 7.4: Sample spectrum from FUSE airglow observation.

7.5 Observation and Results

The results of observations are mainly divided into two main sections. The side looking observations are presented first. Fig. 7.5 shows the distribution of airglow line at 1026Å with local time (night). This wavelength corresponds to the merged spectrum of Lyman β and OI4 through the LWRS aperture. The airglow observations are binned at every 30 minutes. The data is for observations of approximately 90° from zenith. The black squares indicate the brightness averaged over 20 observations and the dotted line represents a

4th degree polynomial fit, with equations as follows.

$$Brightness = 0.04052 \cdot t^4 + 0.197 \cdot t^3 + 2.866 \cdot t^2 + 0.03164 \cdot t + 9.869. \quad (7.2)$$

Where the brightness of the airglow line is in Rayleigh and t is the local time. The polynomial fit has an R-square of 98.15% goodness of fit. The steepness of slope is more towards the morning of local time, indicating an increased airglow activity towards the day time. This also indicates a slow reduction in airglow activity as the sun sets and the stored energy is used for airglow emissions (Meier, 1991).

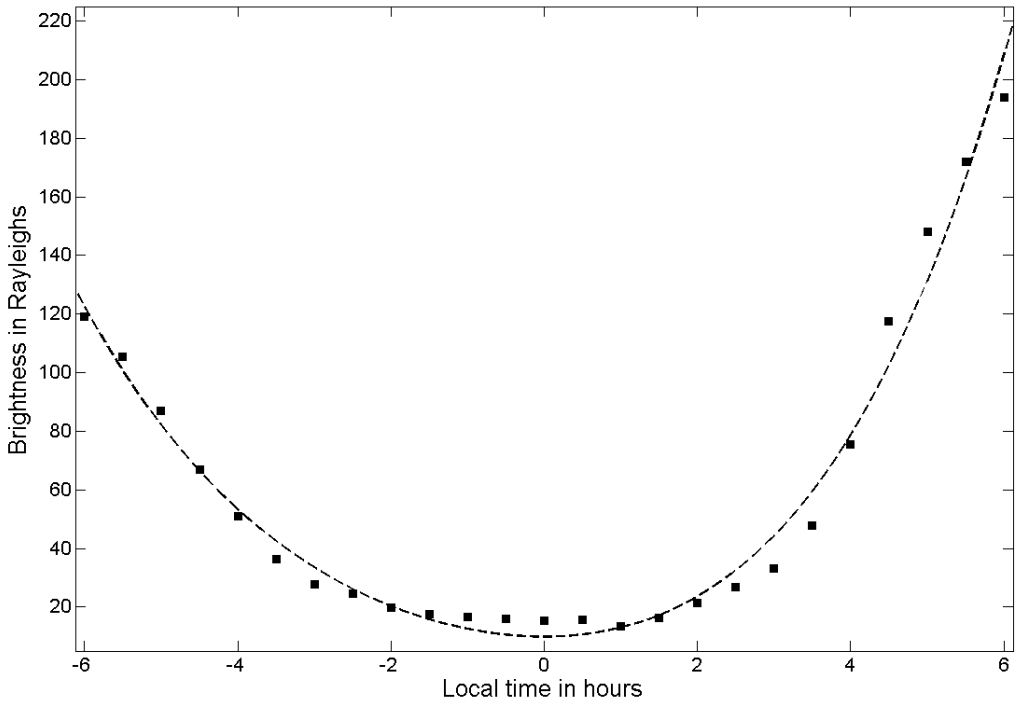

Figure 7.5: Distribution of airglow line at 1026Å with local time centered at local midnight. The data is for observations of approx 90° from zenith. The black squares indicate the brightness (averaged over 20 observations) and the dotted line represent a 4th degree polynomial fit.

The variation of airglow line at 1026Å with elevation is as shown in Fig. 7.6. The observations are binned for elevation angles of 1 degree and contains the average of almost 24 hours of local time for most of the observation. The observations are from a total of 51 exposures spread across one

month in late 1999. The strength of airglow increases from the direction of nadir to the earth limb (corresponding to an elevation angle of around 25 degrees). The strength drastically falls as the observation moves upward from the earth limb. The profile of the strength slowly dies down and reaches a flat profile for elevations above zero degrees (upward looking). This value averages around 40 Rayleigh (day and night combined). The outliers in the plot at around -10 degrees elevation are mainly because of the non availability of data throughout the 24-hour local time. These observations only have data during orbital day and hence the average brightness is more than the expected value. It will be interesting to look at the sun angle from the direction of observation, as this will provide a better understanding of these phenomena.

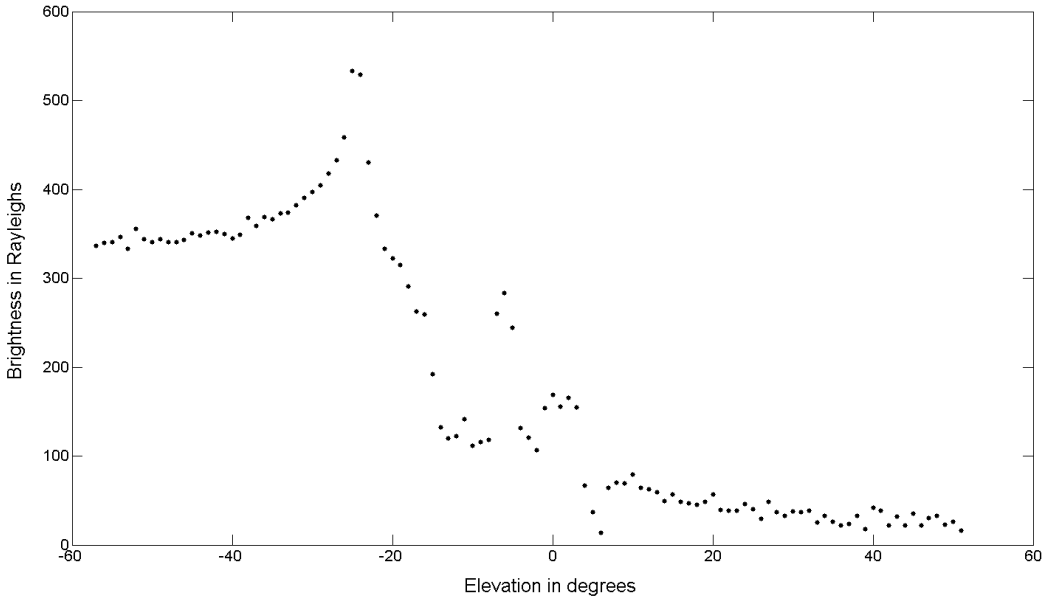

Figure 7.6: Variation of brightness for the airglow line at 1026Å with elevation.

7.6 Conclusion and Future Work

With the vast amount of data available, a table containing the variation of airglow line at 1026Å with azimuth and elevation for 24 hours of local time is

created. This can be used to identify the strength of this particular airglow line at any given azimuth, elevation and time. The results obtained with this exercise will be extended to other observations, so as to cover those azimuths and elevations that are not available in the data set considered.

The work presented in this chapter covers one airglow line. It is necessary to look at other airglow lines as well. We would also like to carry out the same exercise over a band of wavelength to examine whether these observations are consistent. This will enable us to provide with a time-dependent model of the airglow for the UV sky simulator discussed in chapter 2.

Chapter 8

Summary and Future Work

Sreejith, A. G, et al., Proc. SPIE 9908, Ground-based and Airborne Instrumentation for Astronomy VI, 99084E, 2016.

8.1 Introduction

High-altitude balloon experiments provide a faster and more cost effective method for scientific experiments to produce excellent scientific results. NASA achieved more than 45 days of flight at heights above 33 km in 2016, which they plan on improving this year. The constant innovations in space technology and miniaturization of components are pushing the limits of science that can be achieved with high-altitude ballooning. Balloon experiments also provide a viable means of testing the equipments for eventual space flights. Some of the instruments that we have developed for the balloon program are now in the process of flight qualification for space flights. With further improvements in technology, the near space region where high-altitude balloons float will become a major contributer to new scientific discoveries.

8.2 Summary

This thesis begins with the discussion of a first of its kind ultraviolet simulator, which can simulate the sky in the wavelength range of 1300Å to 3200Å. The working of the simulator is described with two examples. The main focus of this thesis is on high-altitude balloon experiments and the instrumentation for the same. The basic requirements and instruments developed for the balloon experiment are described in chapter 3. We are constrained by weight due to our launch location being close to nearby airports and the type of balloons used (We have permission from Airport authority of India for light/medium class balloons, limiting the weight to less than 6 kg). The basic instrumentation includes the telemetry system, flight termination unit, data loggers, etc. The payload for scattered solar light measurements includes an off-the-shelf spectrograph with associated electronics. This is a compact and lightweight instrument for trace gas mapping from ground and airborne platform that can detect multiple gas species at the same time. The initial observations of scattered solar light and the method of extracting trace gas are described. This system can also be used for pollution monitoring. The observations which was achieved was the first and only one of its kind from the subcontinent. These instruments can be easily scaled and modified for both ground based and air borne measurements in the future. It is necessary to have attitude information for observation from a balloon payload, in order to obtain the orientation information a compact light weight attitude sensor was developed using off-the-shelf components. This attitude sensor can obtain the orientation information with an accuracy of $\pm 0.24^{\circ}$. For astronomical and atmospheric observations, this attitude sensor was developed into a pointing system to automatically point to a target in the sky. This pointing system can have applications in aerial photography and as survey tools. For the improvement of the existing spectrographic system, a near ultraviolet spectrograph was designed and developed. This is a modified Czerny-Turner in

divergent illumination and uses a intensified CMOS as the detector. In order to understand the nature of variation of airglow line with time, an analysis of far ultraviolet airglow observation from the FUSE data was carried out.

8.3 Future Work

The instruments and techniques described in the thesis lead to a fully fledged UV observatory on a balloon platform which can do astronomical and atmospheric observations. The details of the UV observatory that we will fly in the coming months are discussed in the following sections.

8.4 Balloon Ultraviolet Observatory

In our earlier high-altitude flights, the payloads experienced frequent oscillations preventing us from continuous observation for a long duration. The development of a pointing and stabilization platform with two-fold coarse/fine pointing will enable stable observations of regions of interest. The details of a fully fledged system which can carry out observations from the stratosphere are described here. The individual components of this balloon UV observatory are complete and now our team is in the process of putting together the complete payload.

8.4.1 Science Objectives

8.4.1.1 Astronomical observations

One of our major goals is to observe astronomical targets of opportunity from balloons. These objects appear with little warning and, as a result, are often only observed in the visible from ground-based observatories. With our quick response time, we can have a balloon launch within two weeks, being well placed to obtain UV observations of these transients. A prime candidate

for such observations would be comets which suddenly appear, as did comet ISON (C/2012 S1) or Siding Spring (C/2013 A1). These were pristine comets whose evolution as traced by the emission in the molecular bands of different ices should have revealed much about their composition. We have developed pointing/stabilization systems suitable for balloon flights which will allow us to observe comets and other transients (e.g. supernovae) in bands not observable by any other ground-based system. Other high-risk targets could be Mercury/Venus, whose observations are difficult because of the proximity to the Sun.

Surprisingly for such a prominent object in the sky, there are only a handful of UV observations of the Moon, primarily because the Moon is so bright that most of the spacecrafts have an avoidance zone around it. We propose to observe the Moon both spectroscopically and with an imager to track changes in the albedo at different phases, where the phase angle of the Solar illumination changes. There is an increased interest in the Moon and it is important to understand the nature of the lunar surface (Henry et al., 1995).

8.4.1.2 Atmospheric observations

Balloons can provide remote sensing and in-situ measurements of trace gases in the upper troposphere and stratosphere (see Chapter 5). The UV window of 200–400 nm includes the lines from several important species in atmospheric chemistry, such as SO_2, O_3, BrO, HCHO. Spectroscopic observations at these wavelengths allow simultaneous measurement of multiple gas species and thus avoid the need for separate electrochemical systems for each gas. Balloon experiments are complementary to space-based instruments in that they are able to measure gas profiles with different observational geometries, while space-based instruments continuously monitor changes in the atmosphere over long periods of time. The widely accepted DOAS technique can be easily applied to spectroscopic observations of light in the atmosphere (scattered or directly from the source) in UV and visible wavelength regions to obtain the

trace gas strengths(Platt & Stutz, 2008).

8.4.2 Proposed Payload

The overall structural payload design is shown in Fig. 8.1. The payload will include several scientific instruments for simultaneous observations in both daytime and nighttime. The major instrument for the payload is a spherical catadioptric telescope of 80 mm aperture together with the UV spectrograph. The control of the pointing of the system is achieved through inertial measurement sensors (coarse pointing) and star sensor (fine pointing).

The operation of the payload can be in two different modes. For bright sources, the telescope with a UV-sensitive CCD at the secondary focus will carry out imaging, while the spectrograph, with the optical fiber connected to

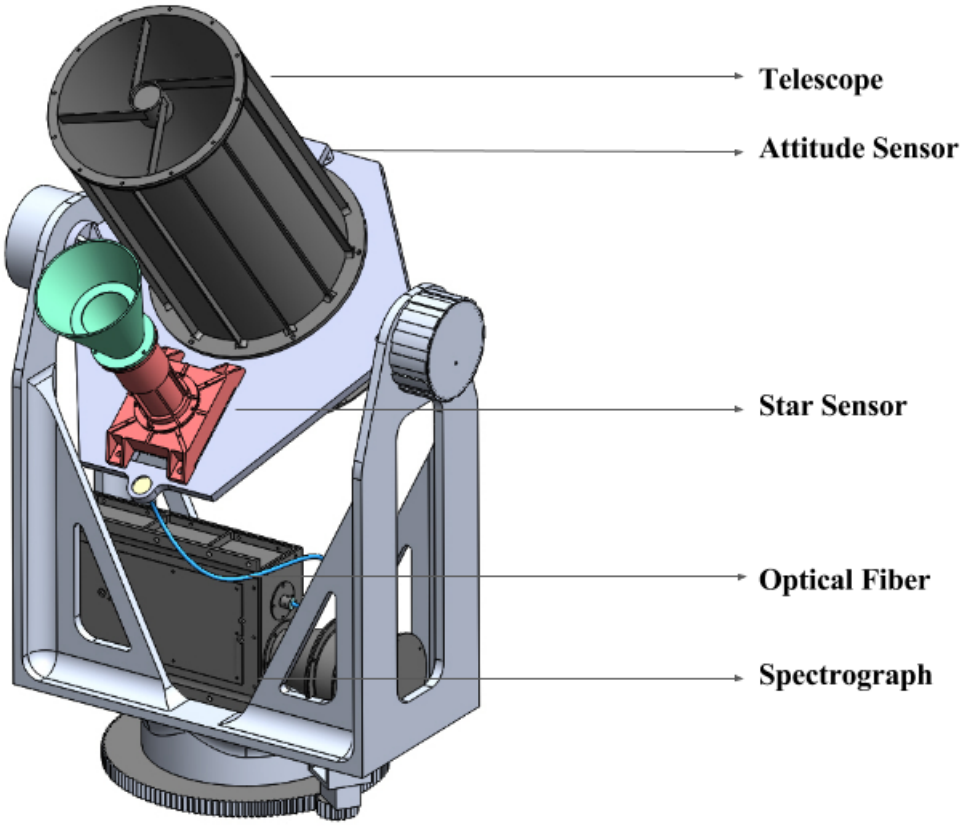

Figure 8.1: Meachanical assembly of complete payload.

the light-collecting lens (20 mm aperture) aligned with the telescope aperture, will conduct parallel spectroscopic observations of the same bright source. For faint sources observations, the optical fiber from the spectrograph will be placed at the secondary focus of the telescope enabling the spectroscopic observations. Both modes can be used for atmospheric observations. During day observations, the system will operate with only the coarse pointing as the star sensor will have difficulty in identifying stars.

Individual components of the payload are described in detail below. The float altitudes have extreme environment conditions of low pressure, and the temperature can go down to -50^oC or so. The low humidity and pressure at these altitudes demand extra care of high-voltage power supplies and detectors to prevent arcing. However, in contrast to space missions, the payload will experience lower vibrations and shocks during launch.

8.4.2.1 Telescope

The system consists of an 80 mm spherical catadioptric telescope mounted on the pointing platform. It has a rectangular field of view of $0.46^\circ \times 0.34^\circ$. The optical design is a two spherical mirror configuration and a double-pass corrector lens system. The secondary focus can house either a UV CCD with a suitable filter or a slit, depending on the mode of observation. The CCD is a 1360×1024 pixels detector which operates at 12 frames per second (fps). The instrument is designed to withstand loads up to 25 g. One of the main objectives is to scan the sky looking for transients. The instrument will acquire the images at a fast frame rate and will analyze each frame looking for brightness variations over the frames. The transient events will be stored on-board or transmitted back to the ground station through a radio link.

8.4.2.2 Spectrograph

The spectrograph used here is the fiber-fed modified Czerny-Turner (C-T) design (Fig. 8.2) which is discussed in detail in chapter 6. The light is fed to the

Table 8.1: Spectrograph technical specifications

Dimensions	$350 \times 130 \times 45$ mm
Weight	1.5 kg
Power	500 mA at +5 VDC
Design	Modified crossed Czerny-Turner
Input Fiber	Connector SMA 905 to single-strand optical fiber (0.22 NA)
Gratings	Holographic UV, 600 lines/mm
Entrance Slit	400 μm
Sun Avoidance Angle	Based on the experiment
Detector	Micro-Channel Plate MCP40
Wavelength	250–400 nm

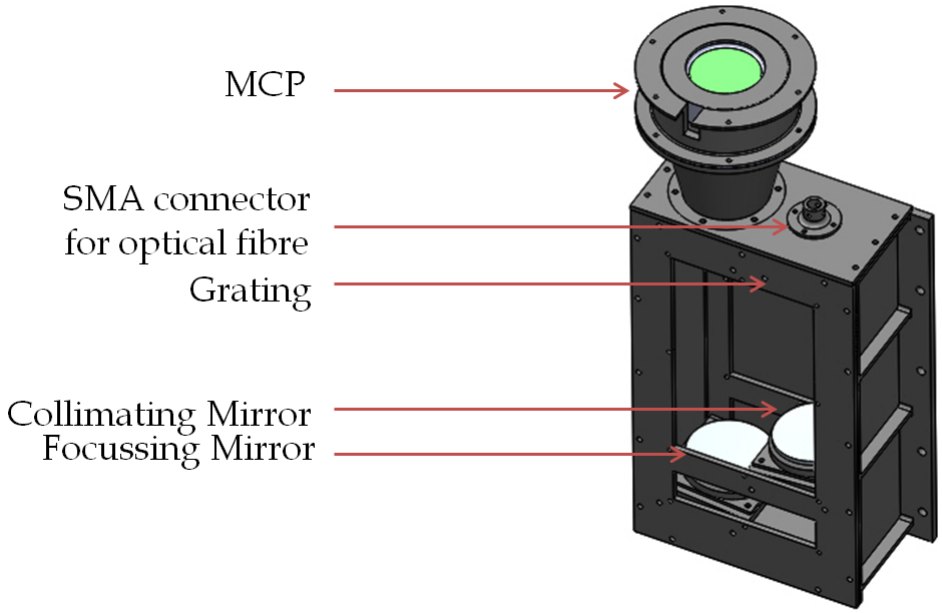

Figure 8.2: The near ultraviolet spectrograph.

spectrograph through a 400 μm diameter optical fiber, whose aperture acts as the entrance slit. The spectrograph is designed to work in the wavelength range of 250–400 nm. It uses commercial-off-the-shelf (COTS) optics with an MCP-based image intensified CMOS camera as the detector of choice. The detector can operate in either photon counting mode or full frame transfer mode. The detector readout is controlled by an FPGA board which enables us to do real-time processing and centroiding of the photon events and store the output data on-board. The block diagram of detector system used in

the spectrograph is shown in Fig. 8.3. The technical details of the spectrograph are given in Table 8.1 for easy reference. The CMOS sensor and the associated optics are attached to the back-end plate of the MCP. The other end of the optical fiber is connected to the telescope, or the light collecting lens, depending on the mode of observation described in the introduction to Section 3.

8.4.2.3 Pointing System

With a telescope placed on the high-altitude balloon payload, one of the major factors in the design of the pointing system is the transfer of oscillations from the flight train, with this constraint more important if the required stability for observation is within one degree of accuracy. In our first experiments of observation of atmospheric lines (Chapter 3, Chapter 5), the pointing accuracy was not of a great concern, but we plan to observe astronomical sources for which we require pointing and stabilization of the order of arc-seconds.

The pointing and stability of the system are carried out as two-fold (coarse and fine pointing) operation, using inertial measurement sensors and a star sensor, respectively. The flow chart describing the pointing system is shown in Fig. 8.4. The attitude sensor obtains the pointing information and corrects the position to an accuracy of $\pm 0.24^{\circ}$ using servomotors. The star sensor

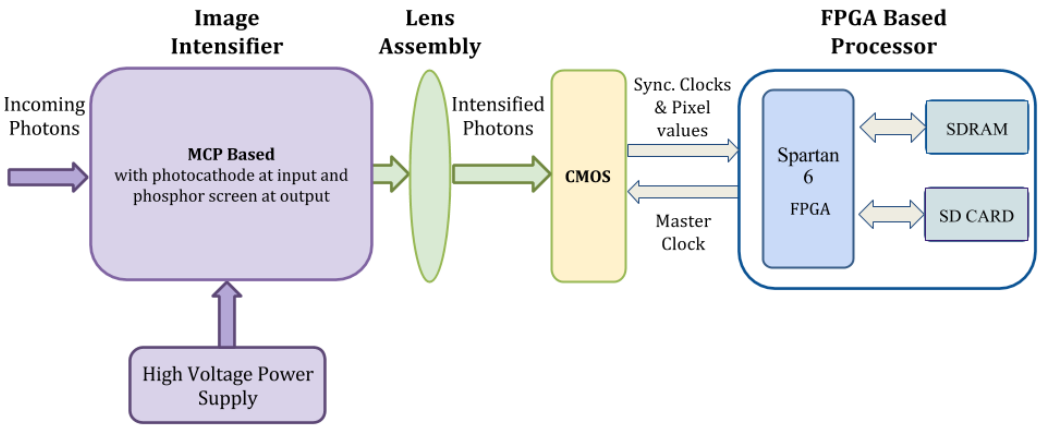

Figure 8.3: Block diagram of detector.

works in the inner loop, providing much finer accuracy of around 13″.

Coarse Pointing: Coarse pointing is carried out using an attitude sensor (see Chapter 4 for details) which acts as the brain for a closed-loop pointing system using servomotors. This sensor comprises an inertial measurement unit (consisting of 3-axis accelerometer, 3-axis gyroscope, and 3-axis magnetometer) with a GPS unit to give pointing to an accuracy of ±0.24° in either Earth-centered inertial coordinates (azimuth and elevation), or in Right Ascension (RA) and Declination (Dec). The technical details of the attitude sensor are given in Table 8.2 for easy reference. This set-up has been tested and found to perform satisfactorily for the requirements (Nirmal et al., 2016).

Table 8.2: Attitude sensor technical specifications

Size	$86 \times 54 \times 45$ mm
Weight	< 100 g without battery
Power	5 W
Components	Accelerometer, Gyroscope, Magnetometer and GPS
Accuracy	0.48° (average RMS)
Output Modes	RA-Dec or Az-Ele

Fine Pointing: Fine pointing is achieved through the use of a star sensor, which is a highly sensitive wide-field imaging camera (Sarpotdar et al., 2017). The camera has a four-element Tessar lens system as its optical element.

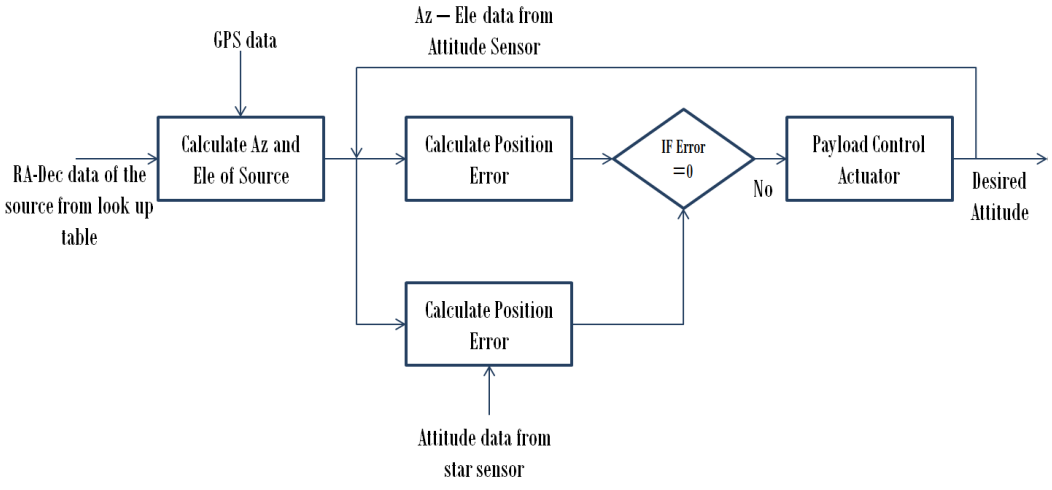

Figure 8.4: Block diagram of fine and coarse pointing control.

Optical design was carried out keeping in mind reduced chromatic aberration, coma, and distortion. The star sensor has a 10° field of view and uses a limiting magnitude of 6.5. It can provide pointing to an accuracy of 12.24″ for a signal to noise ratio of 30. The star sensor can work at a maximum slew rate of about 2°/sec. The technical details of the star sensor are given in Table 8.3. The coarse pointing maintains the payload in this slew rate and the fine pointing is achieved by the inputs from the star sensor.

Table 8.3: Star sensor technical specifications

Accuracy	12.24″
Update Rate	10 Hz
Weight	800 gms
Dimension	$10 \times 10 \times 50$ cm
Power	2W
Communication interface	RS-422
Memory	8MB Flash and 64 MB RAM
Wavelength range	450–750 nm
Sun Avoidance angle	45°

8.4.3 Flight Opportunity

The flight plan for this payload is on a zero-pressure balloon capable of floating at $\sim$ 40 km altitude for up to 5 hours with the National Balloon Facility station of TIFR at Hyderabad later this year. The duration of the float will enable us to observe in the night (with the launch 3–4 hours before sunrise) for astronomical objects, and at daylight for atmospheric studies. The reference spectrum for trace gas analysis will be obtained at float, and the measurements will continue during descent.

In this flight, our team also plan to supplement the observational instruments with the detachable pre-sterilized sampling chamber *SAMPLE* (Stratospheric Altitude Microbiology Probe for Life Existence) designed to collect and contain the dust stratospheric samples and get them back without contamination. We plan to collect dust particles, on which further study will

be conducted to establish the possibility of microbial life in the upper atmosphere.

8.5 Small Satellites

Testing and verification of the payloads on balloon flights are carried out with the intention of placing them on small satellites such as CubeSats. Going into space has the obvious advantages of longer mission life and the ability to go further into the far-UV. There is an increasing number of opportunities for small missions although without the quick response times possible with balloons, and the development of instrumentation skills will benefit future access to space. CubeSats provide a good opportunity to make significant observations at the relatively under-explored regions of the UV spectrum. Our team is currently in the process of developing such payloads that work in the NUV region.

One of the current payloads in the design and development stage is the near ultraviolet spectrograph called the CubeSat Ultraviolet Bright Spectrograph (CUBS). The restrictive CubeSat environment and the short lead times force certain choices on the design. This payload is a part of the program to

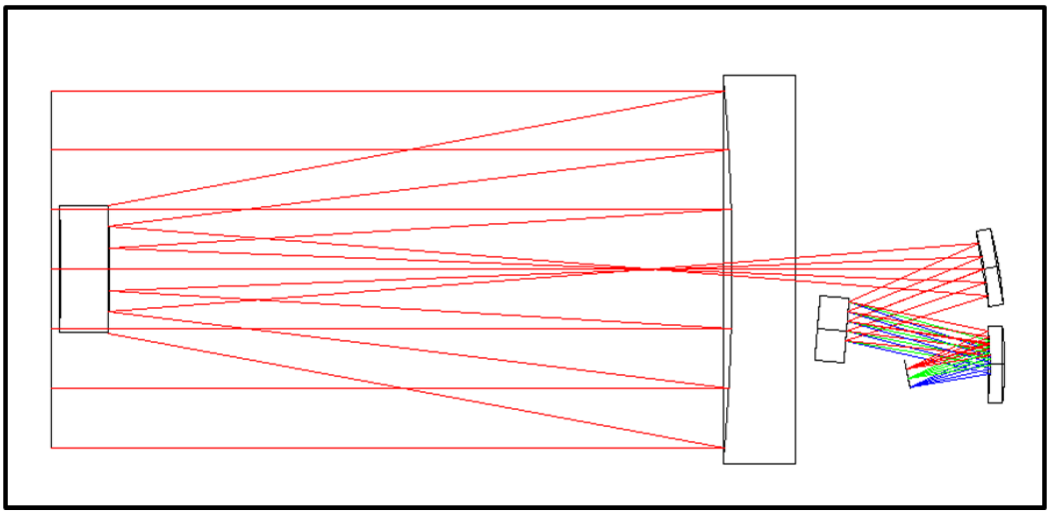

Figure 8.5: Optical design of CUBS.

build payloads that address limited scientific goals but make full use of the opportunities that are arising for CubeSat class missions.

The primary scientific objective of CUBS is to look at the origin of the 2175Å extinction bump. This feature was first observed in the 1960s but its origin is still not well understood. Several models have been presented to account for this bump which includes graphitic grains with a mixture of PAH molecules. To detect the strength of extinction bump CUBS will acquire spectrum of bright stars in the wavelength range 2000-3000 Å with a resolution of 10 Å. Another scientific objective of CUBS is solar system objects.Solar system objects are not usually observed by other space telescopes because of brightness limitations, A CubeSat size spectrograph could look at solar system objects and even comets close to its perihelion.

8.5.1 CUBS

CubeSat Ultraviolet Bright Spectrograph (CUBS) (Fig. 8.5) is a near ultraviolet (200 - 400 nm) spectrograph designed to fit in a 2U CubeSat and planned for flight in 2017/2018 with a scientific goal of obtaining NUV spectra of bright sources (greater than 8th magnitude) with a spectral resolution of 10 Å. The aggressive timeline drives the design to include only off-the-shelf items to minimize procurement delays and cost. The baseline optical design consists of a collecting mirror with a 70 mm diameter. The telescope design is two mirror spherical optics system which reflects light onto a modified Czerny-Turner spectrograph with reflection grating of spacing 1200 lines per mm. The grating focuses the light onto a UV sensitive CCD with a pixel size of 4.65μm $\times$ 4.65μm through a concave mirror. The instrument is an F 2.7 system with a collecting area of about 34 cm^2. The grating used is a ruled UV grating with 1200 lines/mm with an efficiency of more than 65% in 200-300 nm wavelength range. The detector has a QE of greater than 40% in our wavelength of interest of 200-300 nm.

The flight opportunity of the instrument is with a satellite bus being developed by Team Indus, a private company participating in the Google Lunar X prize. The pointing requirement of better than 1 arc minute will be provided by Team Indus.

Bibliography

Aliwell, S. R., Van Roozendael, M., Johnston, P. V., et al., "Analysis for BrO in zenith-sky spectra: An intercomparison exercise for analysis improvement", Journal of Geophysical Research (Atmospheres), 107, 4199 (2002).

Ambily, S., Sarpotdar, M., Mathew, J., et al., "Development of Data Acquisition Methods for an FPGA-Based Photon Counting Detector", Journal of Astronomical Instrumentation , 6, 1750002

Arnold, S. P., Tibor, K., Cheng, A. F., et al., "High-Altitude Balloon Observatories for Planetary Science" AGU Fall Meeting Abstracts, 1821 (2013).

Austin, D., Witting, T., and Walmsley, I., "Broadband astigmatism-free Czerny-Turner imaging spectrometer using spherical mirrors," Appl. Opt. 48, 3846-3853 (2009).

Ayub, S., Bahraminasab, A., Honary, B., "A Sensor Fusion Method for Smart phone Orientation Estimation", in *13th Annual Post Graduate Symposium on the Convergence of Telecommunications, Networking and Broadcasting.* Liverpool, 13th Annual Post Graduate Symposium on the Convergence of Telecommunication, Networking and Broadcasting , Liverpool, United Kingdom, (25-26 June, 2012).

Bar-Itzhack, I. Y.,and Oshman, Y., "Attitude Determination from Vector

Observations: Quaternion Estimation", IEEE Transactions on Aerospace Electronic Systems, 21, 128 (1985).

Bates, B. McDowell, M., and Newton, A. C., "Correction of astigmatism in a Czerny–Turner spectrograph using a plane grating in divergent illumination," J. Phys. E 3(3), 206–210 (1970).

Baum, W. A., Johnson, F. S., Oberly, J. J., et al., "Solar Ultraviolet Spectrum to 88 Kilometers", Physical Review, 70, 781 (1946).

Bevington, P. R., *Data reduction and error analysis for the physical sciences*, McGraw-Hill (1969).

Borenstein, J., Ojeda, L., and Kwanmuang, S., "Heuristic Reduction of Gyro Drift for Personnel Tracking Systems", Journal of Navigation, 62, 41 (2008).

Bogumil, K., J. Orphal, T. Homann, et al., "Measurements of Molecular Absorption Spectra with the SCIAMACHY Pre-Flight Model: Instrument Characterization and Reference Data for Atmospheric Remote-Sensing in the 230-2380 nm Region", J. Photochem. Photobiol.A., 157, 167-184 (2003).

Bovensmann, H., Burrows, J. P., Buchwitz, M., et al., "SCIAMACHY: Mission objectives and measurement modes", Journal of Atmospheric Sciences, 56, 127 (1999).

Byram, E. T., Chubb, T. A., Friedman, H., & Kupperian, J. E., Jr. "Rocket observations of extraterrestrial far-ultraviolet radiation", *Astronom. J.* , 62, 9 (1957).

Chandler, G. G., "Optimization of a 4-m Asymmetric Czerny-Turner Spectrograph," J. Opt. Soc. Am., 58, 895-896 (1968).

Cornu, A., "Observation de la limit ultraviolett du spectre solaire a diverse altitudes", C. R. Acad. Sci., 89 (1879).

Crutzen, P. J., "The influence of nitrogen oxides on the atmospheric ozone content" Quarterly Journal of the Royal Meteorological Society, 96, 320 (1970).

Crutzen, P. J., & Arnold, F., "Nitric acid cloud formation in the cold antarctic stratosphere - A major cause for the springtime 'ozone hole'" *Nature* , 324, 651 (1986).

Czerny, M., and Turner, A., "Ueber den Astigmatimus bei Spiegelspektrometern," Z. Phys. 61, 792–797 (1930).

Dalton, M., "Astigmatism Compensation in the Czerny-Turner Spectrometer," Appl. Opt. 5, 1121-1123 (1966).

Danckaert, T., Fayt, C., van Roozendal, M., de Smedt, I., Letocart, V., Merlaud, A., Pinardi, G., *QDOAS Software user manual*,(2016).

de Beek, R., Vountas, M., Rozanov, V. V., Richter, A., & Burrows, J. P., "The Ring effect in the cloudy atmosphere", Geophys. Res. Lett., 28, 721-724 (2001).

Dixon, W. V., Sahnow, D. J., Barrett, P. E., et al., "CalFUSE Version 3: A Data Reduction Pipeline for the Far Ultraviolet Spectroscopic Explorer", *Pub. Astron. Soc. Pac.*, 119, 527 (2007).

Farman, J. C., Gardiner, B. G., & Shanklin, J. D., "Large losses of total ozone in Antarctica reveal seasonal ClOx/NOx interaction" *Nature* , 315, 207 (1985)

Feldman, P. D., et al., "Ultraviolet spectroscopy of the terrestrial airglow with the Hopkins Ultraviolet Telescope", Eos, Trans. AGU, 72, 207 (1991).

Feldman, P. D., Sahnow, D. J., Kruk, J. W., Murphy, E. M., & Moos, H. W., "High-resolution FUV spectroscopy of the terrestrial day airglow with the Far Ultraviolet Spectroscopic Explorer" *J. Geophys. Res.*, 106, 8119 (2001).

Ferlemann, F., Bauer, N., Fitzenberger, R., et al., "Differential optical absorption spectroscopy instrument for stratospheric balloonborne trace-gas studies," App. Opt., 39, 2377-2386 (2000).

Fesen, R., & Brown, Y., "A method for establishing a long duration, stratospheric platform for astronomical research", *Experimental Astronomy*, **39**, 475, (2015).

Gebre-Egziabher, D., Hayward, R. C., and Powell, J. D., "Design Of Multi-sensor Attitude Determination Systems", IEEE Transactions on Aerospace Electronic Systems, 40, 627 (2004).

Groves, P. D., in *Principles of GNSS, Inertial, and Multisensor Integrated Navigation Systems*, 2nd ed., (Artech House Publishers, UK), (2013).

Hartley, W., "On the absorption of solar rays by atmospheric ozone", J. Chem. Soc., 39, 111 (1881).

Henry, R. C., "Far-Ultraviolet Studies. I. Predicted Far-Ultraviolet Interstellar Radiation Field", *Astrophys. J. Suppl.* , 33, 451 (1977).

Henry, R. C., Feldman, P. D., Kruk, J. W., Davidsen, A. F., & Durrance, S. T., "Ultraviolet Albedo of the Moon with the Hopkins Ultraviolet Telescope", *Astro phy jour ltrs*, **454**, L69, (1995).

Hibbitts, C. A., Young, E., Kremic, T. and Landis, R., "Science measurements and instruments for a planetary science stratospheric balloon platform", *Aerospace Conference, IEEE, Big Sky, MT*, pp. 1-9 (2013).

Hilkert, J., M.," Inertially stabilized platform technology Concepts and principles", IEEE Control Systems, vol. 28, no. 1, pp. 26-46 (2008).

Hönninger, G., von Friedeburg, C., and Platt, U., "Multi axis differential optical absorption spectroscopy (MAX-DOAS)", Atmos. Chem. Phys., 4, 231-254, (2004).

Ji, Y., Zhang, Y., Wang, C.-Y., "Li-Ion Cell Operation at Low Temperatures", J. Electrochem. Soc., 160, A636 (2013).

Kraus, S., 2004. *DOASIS: DOAS intelligent system.*, Institute of Environmental Physics, University of Heidelberg, in cooperation with Hoffmann Messtechnik GmbH, Heidelberg (2004).

Kritten, L., Butz, A., Dorf, M., et al., "Time dependent profile retrieval of UV/vis absorbing radicals from balloon-borne limb measurements – a case study on NO2 and O3", Atmospheric Measurement Techniques, 3, 933 (2010).

Kumar. A., Ghosh, S. K., Hutchings, J., Kamath, P. U., Kathiravan, S., Mahesh, P. K., Murthy, J., Nagbhushana S., Pati, A. K., Rao, M. N., Rao, N. K., Sriram, S., Tandon, S. N., "Ultra Violet Imaging Telescope (UVIT) on ASTROSAT", Proc. SPIE 8443, Space Telescopes and Instrumentation 2012, Ultraviolet to Gamma Ray, 84431N (2012).

Kurucz, R. L., Furenlid, I., Brault, J., & Testerman, L., "Solar flux atlas from 296 to 1300 nm", National Solar Observatory Atlas, Sunspot, New Mexico: National Solar Observatory, (1984).

Lemaire, P.,"High Resolution Balloon-Borne Spectrograph for the Near Solar Ultraviolet" New techniques in Space Astronomy, 41, 263 (1971).

Lemaire, P., & Samain, D., "High resolution observations of the solar UV spectrum from balloon", High spatial resolution solar observations, Proceedings of the 10th Sacramento Peak Summer Workshop, Sunspot, New Mexico, 551 (1989).

Leinert, C., Bowyer, S., Haikala, L. K., et al., "The 1997 reference of diffuse night sky brightness", *Astron. Astrophys. Suppl.* , 127, 1 (1998).

Llewellyn, E., Lloyd, N. D., Degenstein, D. A., et al., "The OSIRIS instrument on the Odin spacecraft", Canadian Journal of Physics, 82, 411 (2004).

Marquardt, D. W., "An Algorithm for Least-Squares Estimation of Nonlinear Parameters.", Journal of the Society for Industrial and Applied Mathematics, 11(2), 431-441 (1963).

Martin, D. C., Fanson, J., Schiminovich, D., et al., "The Galaxy Evolution Explorer: A Space Ultraviolet Survey Mission", *Astrophys. J. Lett.* , 619, L1 (2005).

McPeters, R. D., Janz, S. J., Hilsenrath, E., et al., "The retrieval of O3 profiles from limb scatter measurements: Results from the Shuttle Ozone Limb Sounding Experiment", Geo. Phy. Res. Ltrs, 27, 2597 (2000).

Meier, R. R., "Ultraviolet spectroscopy and remote sensing of the upper atmosphere" Space Science Reviews , 58, 1 (1991).

Molina, M. J., & Rowland, F. S., "Stratospheric sink for chlorofluoromethanes: chlorine atomc-atalysed destruction of ozone", *Nature* , 249, 810 (1974).

Moos, H. W., Cash, W. C., Cowie, L. L., et al., "Overview of the Far Ultraviolet Spectroscopic Explorer Mission", *Astrophys. J. Lett.* , 538, L1 (2000).

Morrissey, P., Conrow, T., Barlow, T. A., et al., "The Calibration and Data Products of GALEX", *Astrophys. J. Suppl.* , 173, 682 (2007).

Murcray, D. G.,Murcray, F. H., & Williams, W. J., "Variation of the Infrared Solar Spectrum Between 700 cm^{-1} and 2240 cm^{-1} with Altitude", Appl. Opt. 8, 2519-2536 (1969).

Murtagh, D., Frisk, U., Merino, F., et al., "Review: An overview of the Odin atmospheric mission", Canadian Journal of Physics, 80, 309 (2002).

Murthy, J., & Henry, R. C., "A Model of the Diffuse Ultraviolet Radiation Field", *Astrophys. J.* , 448, 848 (1995).

Murthy, J., & Sahnow, D. J., "Observations of the Diffuse Far-Ultraviolet Background with the Far Ultraviolet Spectroscopic Explorer", *Astrophys. J.* , 615, 315 (2004).

Murthy, J., "Observations of the near and far ultraviolet background" Astrophysics and Space Science , 320, 21 (2009).

Murthy, J., Henry, R. C., & Sujatha, N. V., "Mapping the Diffuse Ultraviolet Sky with the Galaxy Evolution Explorer", *Astrophys. J.* , 724, 1389 (2010).

Murthy, J., "The diffuse ultraviolet foreground", *Astrophys. Space Sci.* , 349, 165 (2014).

Navach, C., Lehmann, M., & Huguenin, D., "Feasibility of UV astronomy by balloon-borne observations. I. Stellar spectrophotometry.", *Astron. Astrophys.*, 22, 361 (1973).

Nirmal, K., Sreejith, A. G., Mathew, J., Sarpotdar, M., Suresh, A., Safonova, M., and Murthy, J., "Pointing System for the Balloon-Borne Telescope", Journal of Astronomical Telescopes, Instruments, and Systems, Vol. 02, issue. 04, 047001, (2016).

Ocean Optics, 2009: Maya Pro 2000 fiber optic spectrometer installation and operation manual. Available online at:*http://oceanoptics.com///wp-content/uploads/Maya.pdf.*

Okano, S., Okabayashi, M., and Gernandt, H., "Observations of ozone profiles in the upper stratosphere using a UV sensor on board a light-weight high-altitude balloon.", Memoirs of NIPR Spec. Issue, 51, 225 (1996).

Pang, H., Chen, D., Pan, M., et al., "A New Calibration Method of Three Axis Magnetometer With Nonlinearity Suppression.", IEEE Transactions on Magnetics, 49, 5011 (2013).

Perryman, M. A. C., Lindegren, L., Kovalevsky, J., et al., "The HIPPARCOS Catalogue", *Astron. Astrophys.*, 323, L49 (1997).

Pio, R.L., "Euler angle transformations ", IEEE Trans on Automatic Contro, AC11 (4), 707 (1966).

Platt, U., Perner, D., & PäTz, H. W., "Simultaneous measurement of atmospheric CH2O, O3, and NO2 by differential optical absorption", *J. Geophys. Res.*, 84, 6329 (1979).

Platt, U., Perner, D., Winer, A. M., Harris, G. W., & Pitts, J. N., Jr., "Detection of NO3 in the polluted troposphere by differential optical absorption", *Geophys. Res. Lett.*, 7, 89 (1980).

Platt, U., & Perner, D., "Direct measurements of atmospheric CH2O, HNO2, O3, NO2, and SO2 by differential optical absorption in the near UV", *J. Geophys. Res.*, 85, 7453 (1980).

Platt, U. and Stutz, J.: *Differential Optical Absorption Spectroscopy: Principles and Applications, Physics of Earth and Space Environments*, ISBN 978-3-540-21193-8, Springer-Verlag Berlin Heidelberg, (2008).

Rouse, P. E., Jr., Brixner, B., & Kline, J. V., "Optimization of a 4-m Asymmetric Czerny-Turner Spectrograph," J. Opt. Soc. Am. 59, 955-958 (1969).

Sabastian, T. A., Guarddin, G., Abi, R. N., Mufti, H. M., International Conference on Advanced Computer Science and Information Systems (ICACSIS), 83 (2012).

Safonova, M., Shalima, P., & Murthy, J., "TAUVEX flight calibrations: Plans and challenges", Bulletin of the Astronomical Society of India, 37, 23 (2009).

Sagiv, I., Gal-Yam, A., Ofek, E. O., et al., "Science with a Wide-field UV Transient Explorer", *Astronom. J.* , 147, 79 (2014).

Sahnow, D. J., Moos, H. W., Ake, T. B., et al., "On-Orbit Performance of the Far Ultraviolet Spectroscopic Explorer Satellite", *Astrophys. J. Lett.* , 538, L7 (2000).

Sarpotdar, M., Mathew, J., Sreejith, A. G., Nirmal. K., Ambily, S., Prakash, A., Safonova, M. and Murthy, J., "A software package for evaluating the performance of a star sensor operation", Experimental Astronomy,Vol 43, Issue 1, pp 99–117 (2017).

Seon, K. I., Edelstein, J., Korpela, E., et al., "Observation of the Far-ultraviolet Continuum Background with SPEAR/FIMS", *Astrophys. J. Suppl.* , 196, 15 (2011)

Shafer, A. B., Megill, L. R.,& Droppleman, L., "Optimization of the Czerny-Turner Spectrometer," J. Opt. Soc. Am. 54, 879-886 (1964).

Shafer, A., "Correcting for Astigmatism in the Czerny Turner Spectrometer and Spectrograph," Appl. Opt. 6, 159-160 (1967).

Shiau, J.K., Huang, C., Chang, M., "Noise Characteristics of MEMS Gyro's Null Drift and Temperature Compensation"' Journal of Applied Science and Engineering, 15, 239 (2012).

Si, F., Xie, P.,Liu, C., Liu, J., Zhang, Y., Dou, K. and Liu, W., "Retrieval of ultraviolet skylight radiances and O3 slant column densities from balloon-borne limb spectrometer," Chin. Opt. Lett. 6, 541-543 (2008).

Solomon, S., Garcia, R. R., Rowland, F. S., & Wuebbles, D. J., "On the depletion of Antarctic ozone" *Nature* , 321, 755 (1986).

Sreejith, A. G., Safonova, M., & Murthy, J., "Near ultraviolet spectrograph for balloon platform", Proceedings of SPIE, 9654, 96540D (2015).

Subramaniam, A., & Tandon, S., "UVIT image simulations of some Globular clusters with compact objects", 39th COSPAR Scientific Assembly, 39, 1901 (2012).

Sujatha, N. V., Chakraborty, P., Murthy, J., & Henry, R. C., "A model of the stellar radiation field in the UV", Bulletin of the Astronomical Society of India, 32, 151 (2004).

Sujatha, N. V., Murthy, J., Karnataki, A., Henry, R. C., & Bianchi, L., "GALEX Observations of Diffuse UV Radiation at High Spatial Resolution from the Sandage Nebulosity", *Astrophys. J.* , 692, 1333 (2009).

Toon, O. B., Pinto, J., Hamill, P., & Turco, R. P., "Condensation of HNO3 and HCl in the winter polar stratospheres", *Geophys. Res. Lett.*, 13, 1284 (1986).

Vandaele, A. C., Hermans, C., Simon, P. C., et al., "Measurements of the NO2 absorption cross-section from 42000 cm-1 to 10000 cm-1 (238–1000 nm) at 220 K and 294 K.", JQSRT , 59, 171–84 (1998).

Wahner, A., Ravishankara, A. R., Sander, S. P., & Friedl, R. R. "Absorption cross section of BrO between 312 and 385 nm at 298 and 223 K ", Chemical Physics Letters, 152, 507 (1988).

Wamsteker, W., Prochaska, J. X., Bianchi, L., et al., "The Need for Ultraviolet to Understand the Chemical Evolution of the Universe and Cosmology", *Astrophys. Space Sci.* , 303, 69 (2006).

Wang, J., Wang, S., and Lin, G., "Design of resolution testing facility for ultraviolet imager" Chin. Opt. Lett. 6, 510-512 (2008).

Weidner, F., Bösch, H., Bovensmann, H., Burrows, J. P., Butz, A., Camy-Peyret, C., Dorf, M., Gerilowski, K., Gurlit, W., Platt, U., von Friedeburg, C., Wagner, T., and Pfeilsticker, K., "Balloon-borne limb profiling of UV/vis skylight radiances, O3, NO2, and BrO: technical set-up and validation of the method", Atmos. Chem. Phys., 5, 1409-1422 (2005).

Weidner, F., "Development and Application of a Versatile Balloon-Borne

DOAS Spectrometer for Skylight Radiance and Atmospheric Trace Gas Profile Measurements", PhD Thesis, IUP Heidelberg, (2005).

Wolff, M. A., Herber, A., Jacobi, H.-W., et al., "The Development of a Miniature Optical Sensor for Balloon-Borne Measurements of Ozone Profiles", Journal of Atmospheric and Oceanic Technology, 25, 57 (2008).

Xue, Q., Wang, S., and Lu, F., "Aberration-corrected Czerny-Turner imaging spectrometer with a wide spectral region," Appl. Opt. 48, 11-16 (2009).